NSG 1142

DESIGN AND FABRICATION OF MICROSTRIP ANTENNA ARRAYS

June 1978

Final Report

Approved for public release, distribution unlimited.

Prepared for

NASA Langley Research Center
Hampton, Virginia 23665

THE UNIVERSITY OF KANSAS CENTER FOR RESEARCH, INC.
2291 Irving Hill Drive—Campus West
Lawrence, Kansas 66045

THE UNIVERSITY OF KANSAS CENTER FOR RESEARCH, INC.

2291 Irving Hill Drive—Campus West
Lawrence, Kansas 66045

Telephone:

NSG 1142

DESIGN AND FABRICATION OF MICROSTRIP ANTENNA ARRAYS

June 1978

Final Report

Approved for public release, distribution unlimited.

Prepared for

NASA Langley Research Center
Hampton, Virginia 23665

DESIGN AND FABRICATION OF MICROSTRIP DISK ANTENNA ARRAYS

ABSTRACT

A microstrip array project was conducted to demonstrate the feasibility of designing and fabricating simple, low cost, low sidelobe phased arrays with circular disk microstrip radiating elements. Design data were presented for microstrip elements and arrays including the effects of the protective covers, the mutual interaction between elements, and stripline feed network design. Low cost multilayer laminate fabrication techniques were also investigated.

Utilizing this design data two C-band low sidelobe arrays were fabricated and tested: an eight-element linear and a sixty-four-element planar array. These arrays incorporated stripline Butler matrix feed networks to produce a low sidelobe broadside beam.

PREFACE

This final technical report, which covers the period June 1, 1975, through June 30, 1978, was prepared by the Center for Research, Inc., the University of Kansas, under NASA Grant NSG1142. The work was administered under the direction of Dr. M. C. Bailey of the NASA Langley Research Center.

TABLE OF CONTENTS

LIST OF FIGURES

FIGURES PAGE

FIGURES PAGE

FIGURES PAGE

FIGURES PAGE

LIST OF SYMBOLS

c_o	speed of light in vacuum
D	directivity
D_{max}	maximum directivity
d	length of array
d_x, d_y	element spacing in the x and y direction
E	electric field intensity
$\hat{e}_i$, $\hat{e}_j$	normalized vector mode functions for the waveguide excitations of the ith and jth apertures
f	array factor
f_R	resonance frequency
G	gain
g	element radiation pattern
H	magnetic field intensity
h	resonator height
I	current
k_o	free space propagation constant

SYMBOLS (Continued)

N	number of array elements
$\hat{P}$	complex polarization unit vector
P_j	input power
P_{loss}	dissipated power
P_o	output power
P_{rad}	radiated power
P_{tot}	total power
R	distance between antennas
r	cavity, disk, or waveguide radius
r, Θ, ϕ	spherical coordinates
$[S]$	scattering matrix
$s(\Theta,\phi)$	element gain pattern
S_i	area of ith aperture
$S_{mn,pg}$	complex transmission between element (mn) and (pg)
t	substrate thickness
TE	transverse electric

SYMBOLS (Continued)

TEM	transverse electromagnetic
TM	transverse magnetic
V_i, V_j	normalized modal voltage for aperture i and j
V_{mn}	complex excitation to element (m, n)
V_n^+	incident voltage
V_n^-	reflected voltage
VSWR	voltage standing wave ratio
X'_{nm}	mth zero of the derivative of the Bessel function of order n
X, Y, Z	variables in reference Cartesian coordinate system
X_{11}	first root of $J'_1(X_{11}) = 0$
[Y]	admittance matrix
Y_{ij}	mutual admittance between apertures i and j
Y_o	characteristic admittance
$\hat{z}$	unit vector in the z direction
Z_{mn}	active impedance of element (mn)

SYMBOLS (Continued)

Z_o	characteristic impedance
α_{mn}	phase of excitation to element (m,n)
β	phase of array excitation
δ	phase error
Γ	reflection coefficient
ε	complex permittivity
ε_r	dielectric constant
ε_o	permittivity of free space
ζ_o	intrinsic admittance of free space
λ	wavelength
η	efficiency
Θ_B	half power beamwidth
Θ_s	main beam scan angle in Θ direction
ρ	magnitude of reflection coefficient
Φ	power density per unit solid angle
Φ_{av}	average power density per unit solid angle

SYMBOLS (Continued)

ϕ_s	main beam scan angle in ϕ direction
ψ_B	half power beamwidth
ψ_x	phase increments between consecutive array columns
ψ_y	phase increments between consecutive array columns
Ω	solid angle

CHAPTER 1 INTRODUCTION

A microstrip array project was conducted to demonstrate the feasibility of designing and fabricating simple, low cost, low sidelobe phased arrays with circular disk microstrip radiating elements. Development was concentrated in three areas:

1. Microstrip radiating elements,
2. Linear and planar microstrip arrays,
3. Stripline Butler matrix feed networks.

The Microstrip Antenna

The microstrip antenna is a relatively new antenna and was patented by Munson in 1975 [1]. Microstrip antennas have been in use since 1969 and their development has been documented in references [2, 3, 4, 5]. The microstrip radiator is well suited for phased array applications [6]. The microstrip antenna is physically thin, conformal, rugged, and inexpensive to manufacture. The radiation pattern is similar to that of an open ended waveguide. Although the antenna is a relatively narrow band device, the antenna has enough bandwidth for many applications.

The microstrip antenna is basically a metal patch which is supported parallel to a ground plane by a dielectric material, as shown in figure 1-1. The structure may be fabricated from standard printed circuit double clad laminates. The metal on one side of the laminate is the ground plane, and the copper on the other side is

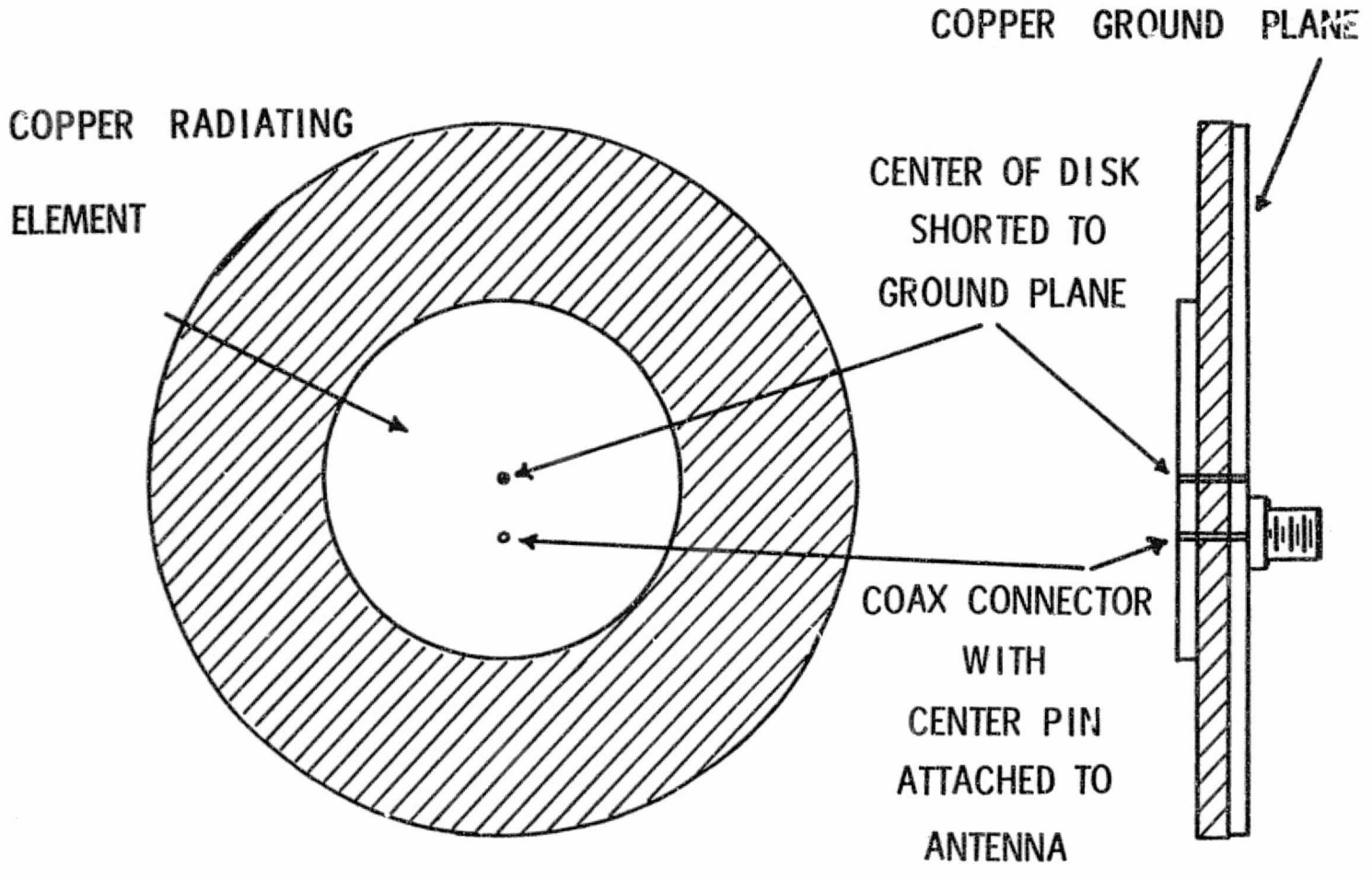

Figure 1-1. Microstrip disk antenna fed from the back.

etched away to form a metal patch. The metal patches considered here are circular disks with a diameter of one-half wavelength in the dielectric. Each disk is excited by a probe from the back and the center of the disk is shorted to the ground plane as described by Howell [4].

Microstrip Arrays

A microstrip array is a set of microstrip antennas radiating in phase coherence. The design of the radiating elements, the array geometry, and the feed network determine the characteristics of the radiation pattern.

The microstrip antenna is a revolutionary breakthrough in conformal low cost phased array technology. Small microstrip arrays have been described in the literature [2, 3, 5, 6, 7, 8]. Many of these arrays are conformal since the thin laminate allows the antenna to conform to the surface of a vehicle. For example, on an aircraft the low profile flush mounted antenna has a negligible effect on the air flow and the aircraft mechanical structure. The antenna installation cost is low since the array is easy to mount on the surface of existing structures. These antennas can be made very rugged since they are so thin.

This report describes the design and fabrication of both linear and planar arrays. Linear arrays consiting of circular disk microstrip elements were fabricated and tested at C-band, and the array elements were etched from teflon fiberglass dual clad laminates, figure 1-2. These linear arrays produced 20 by 83 degree half power beamwidth fan beam radiation patterns.

Figure 1-2. The 8 element linear microstrip array.

Planar arrays consisting of 64 circular disk microstrip elements were also designed, fabricated, and tested at C-band. Figure 1-3 shows the array on a teflon fiberglass laminate. This planar array produced a broadside 20 degree half power beamwidth pencil beam radiation pattern.

The Feed Network

The linear and planar arrays developed in this program were designed to produce low sidelobes. The low sidelobes were achieved with Butler matrix feed networks [9] which produced a cosine amplitude excitation distribution. The cosine excitation resulted in radiation pattern sidelobes which are typically 23 decibels below the peak of the main beam. The networks are implemented in stripline with quadrature branchline hybrids, fixed-line length phase shifters, and power dividers.

Low profile microstrip arrays combined with stripline Butler matrix feed networks resulted in low sidelobe systems which can be fabricated inexpensivley.

The microstrip array program is being conducted at the National Aeronautics and Space Administration (NASA) Langley Research Center, in Hampton, Virginia. The project is sponsored by NASA grant NSG-1142.

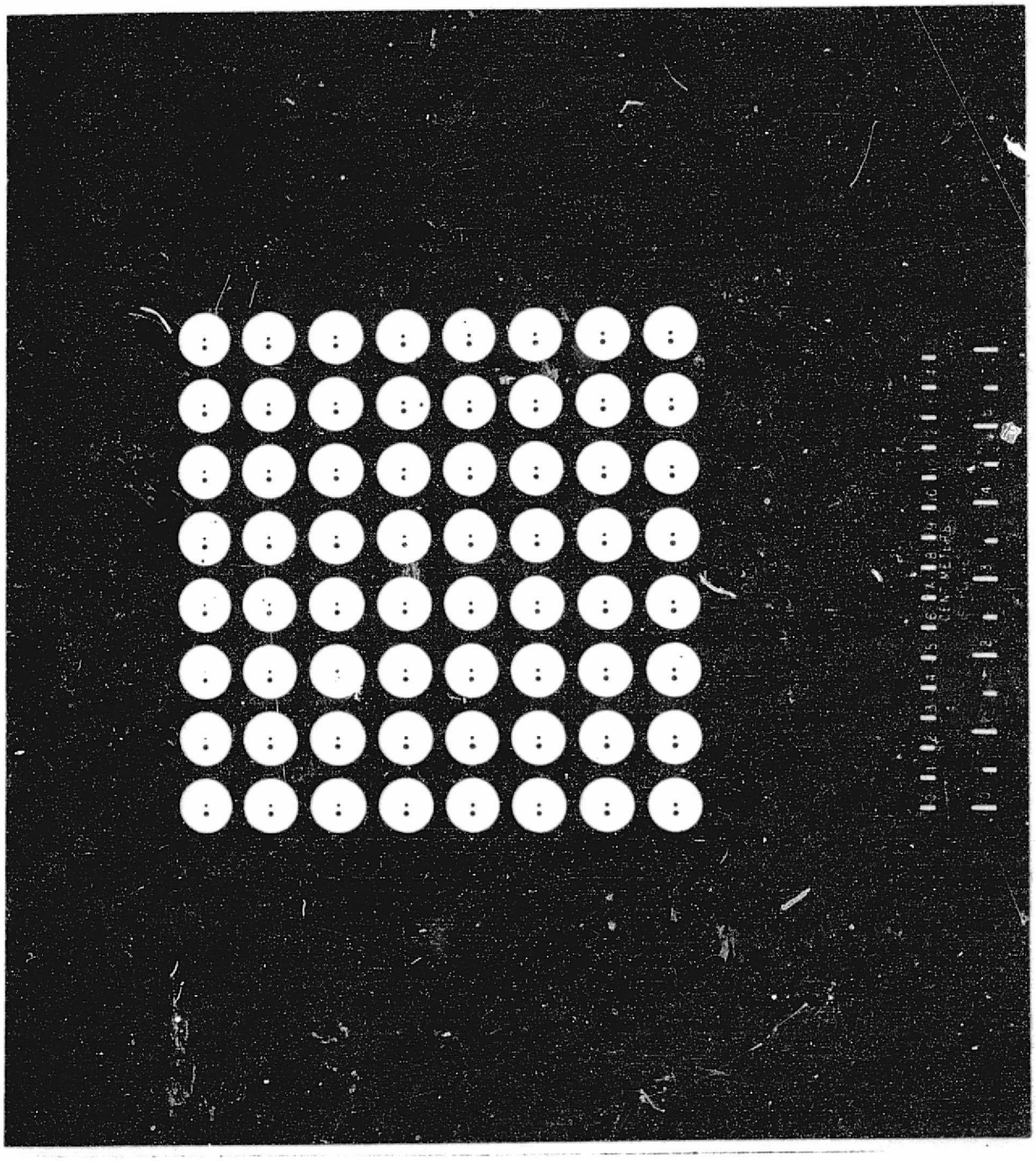

Figure 1-3.. The 64 element planar microstrip array.

CHAPTER 2 DESIGN

This chapter describes the design and development of simple, low cost, low sidelobe phased arrays with microstrip disk radiating elements. The microstrip radiating element is considered first. The microstrip antennas are then incorporated into the design of linear and planar antenna arrays. The chapter concludes with the design of low sidelobe stripline Butler matrix feed networks which feed the microstrip arrays. This project produced two low cost C-band antenna system designs: a linear array and a planar array. The linear array was designed to produce a 20^{0} X 85^{0} half power beamwidth and a linearly polarized fan beam radiation pattern. The planar array is designed for a 20^{0} X 20^{0} half power beamwidth pencil beam. The sidelobes are designed to be at least 20 dB below the peak of the beam.

These systems will produce a broadside beam. Design information is provided so that a scanning beam feed network may be included at a later time in place of the broadside beam network.

The initial concept of the array configuration is shown in figure 2-1. The radiating elements are copper disks on a copper clad dielectric sheet. Each element is fed from the back by a stripline feed network bonded to the array. All radiators are connected through the feed network to a single common connector on the back side.

Various techniques for the design of phased arrays have been devised. Wheeler [10] has outlined the small array, the infinite array simulator, and the grating lobe series approaches. Amitay, Galindo, and Wu [11] discussed infinite array computations.

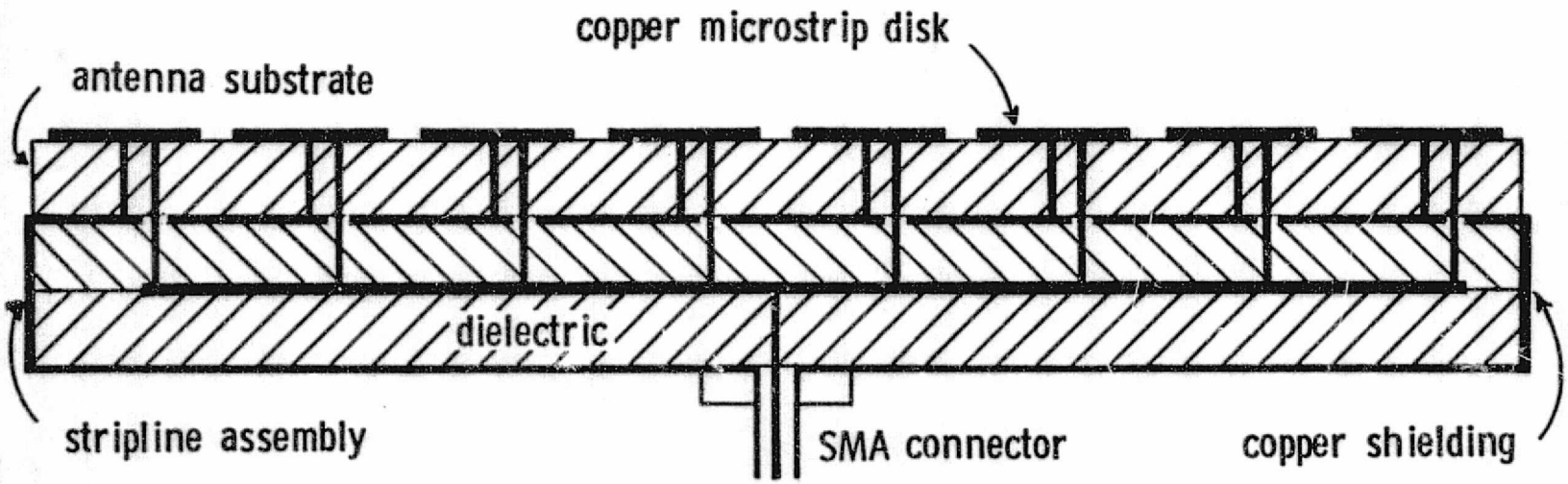

Figure 2-1. Cross section of the microstrip array fed with a stripline network.

Arrays were designed using the small array techniques discussed by Diamond [12]. The following design procedure was used:

1. Match the input impedance of a single microstrip element
2. Choose the element lattice and determine the number and spacing of elements
3. Design the dielectric cover if required
4. Redesign the array to include the effects of mutual coupling
5. Design the feed network amplitude distribution for sidelobe control, and design the progressive phase distribution for beam tilt.

Microstrip Element Design

The first step in the phased array design process is to design and match a single microstrip element. The structure of the linearly polarized element is shown in figure 1-1. The radiator is a metal patch supported by a dielectric clad ground plane. The metal patch may be round, square, or rectangular; however, many different shapes will produce similar results. Some shapes have dual frequency, dual polarization, or circular polarization characteristics. The circular disk shape is used here because of the geometrical symmetry.

Input impedance.- The microstrip disk antenna can be matched from the back directly to a 50-ohm transmission line. The input impedance is a function of the distance from the feed point to the disk center. The impedance at resonance increases from zero at the center to approximately 120 ohms at the disk edge. The 50-ohm feed point is one-third of the radius from the center of the disk.

The microstrip disk is a narrow band antenna since the disk is spaced above the ground plane a small fraction of a wavelength. Figure 2-2 shows how the impedance and return loss vary rapidly as the frequency changes. This disk diameter is 1.86 cm on a .16 cm substrate with a 2.5 dielectric constant. The return loss when fed from the back at resonance is usually less than -25 dB. The bandwidth for a voltage standing wave ratio (VSWR) of less than 3:1 is 5 percent. The bandwidth is 2 percent for a VSWR of less than 2:1.

The bandwidth can be increased by increasing the dielectric substrate thickness. The Munson formula for the bandwidth [13] is

$$\text{Bandwidth (MHz)} = 4f_R^2 \frac{t}{(1/32)}, \quad (\text{VSWR} < 2{:}1) \qquad (2.1)$$

where f_R is the frequency in GHz and t is the dielectric substrate thickness in inches. The $1/32$ factor is retained since copper clad laminates are obtained in multiples of 1/32 inch (.079 cm).

The measured percent bandwidth as a function of substrate thickness is shown in figure 2-3. The data are for antennas with a substrate dielectric constant of 2.5.

Resonant frequency.- The microstrip antenna can be analyzed as a microstrip disk resonator to predict the resonant frequency. The radiating disk of radius r and the ground plane below it are considered to be a dielectric loaded resonator with magnetic sidewalls of height h, see figure 2-4.

Watkins [14] formulated the resonance frequencies f_R of the resonator model. Howell [15] used this model to predict the resonance

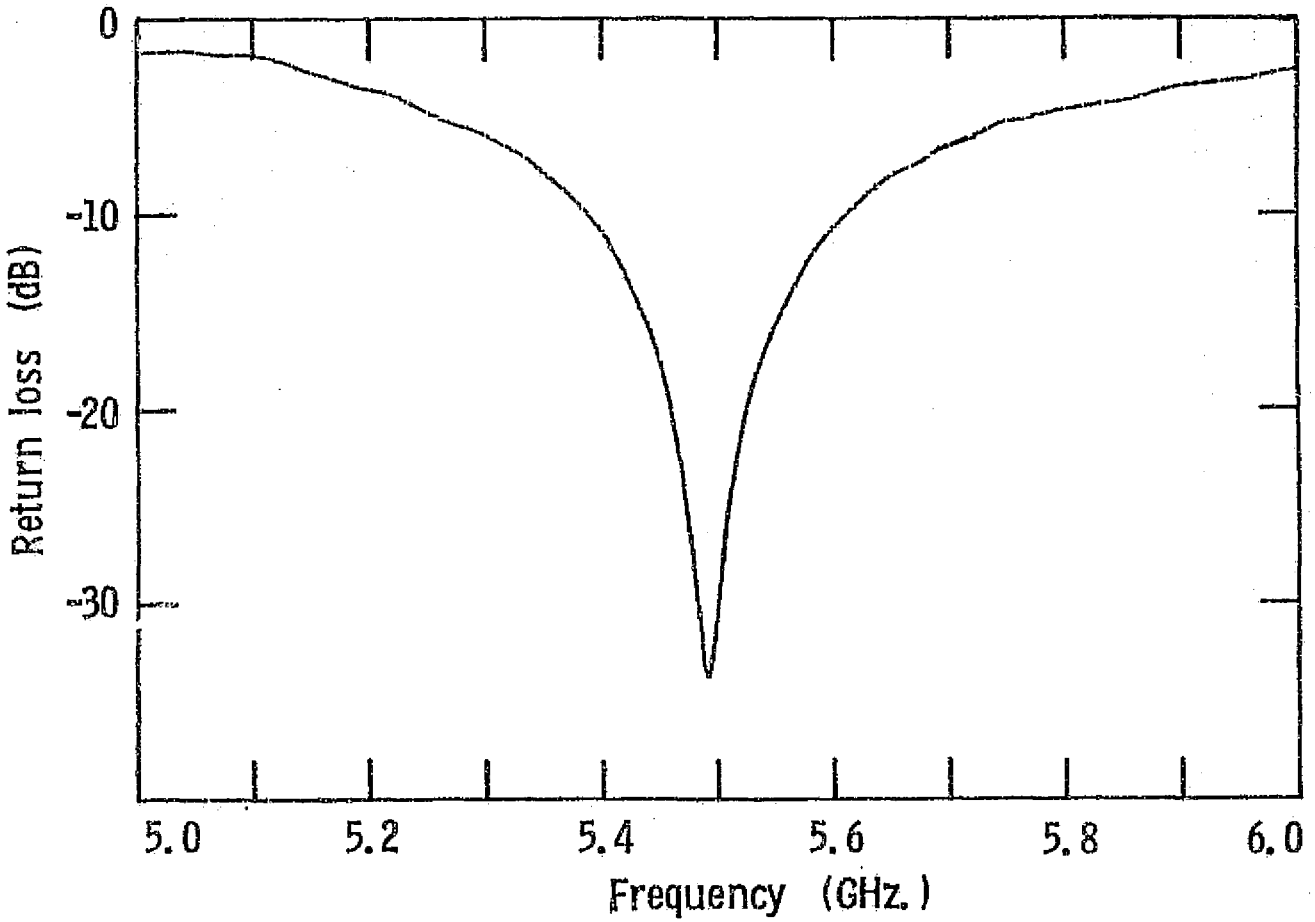

Figure 2-2. Measured return loss of a microstrip disk.

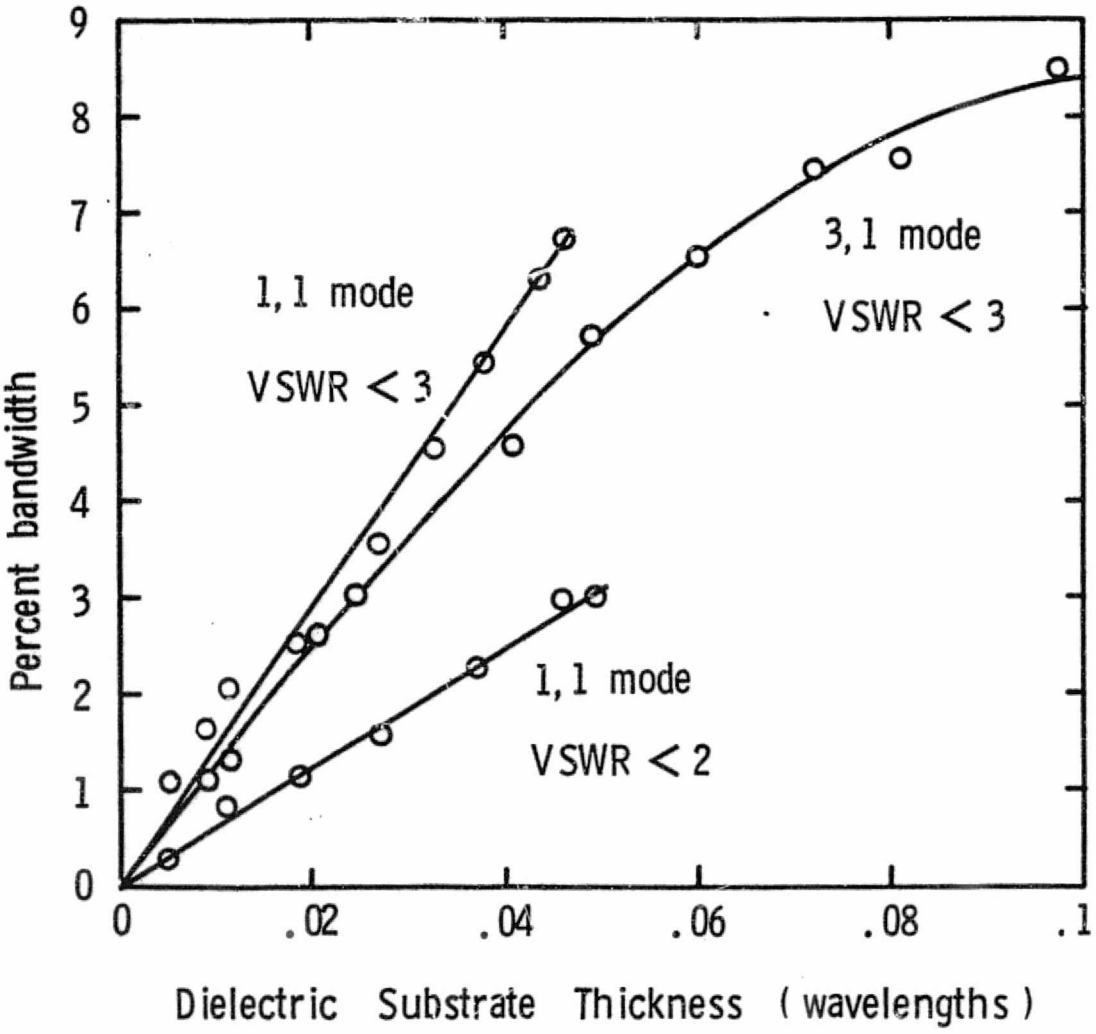

Figure 2-3. Percent bandwidth of a microstrip disk versus substrate thickness.

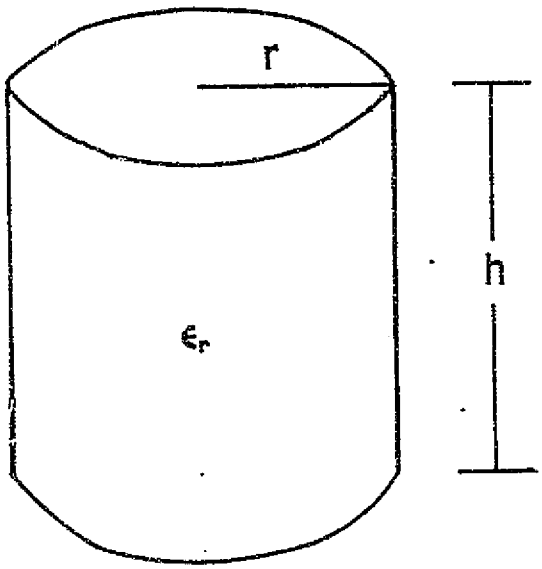

Figure 2-4. Dielectric loaded cavity with magnetic sidewalls.

frequency of microstrip antennas:

$$f_R = \frac{X'_{nm}\, c_0}{2\pi r\, (\varepsilon_r)^{\frac{1}{2}}} \qquad (2.2)$$

where ε_r is the substrate dielectric constant and X'_{nm} is the mth zero of the derivative of the Bessel function of order n, and $c_0 = 3 \cdot 10^{10}$ cm/sec. For m = 1

$$X'_{n1} = \begin{cases} 1.841 & n=1 \\ 3.054 & n=2 \\ 4.201 & n=3 \end{cases} \qquad (2.3)$$

The resonant frequency for the lowest order mode (TE_{11}) is

$$f_R = \frac{1.841\, c_0}{2\pi r\, (\varepsilon_r)^{\frac{1}{2}}} \qquad (2.4)$$

The calculated resonance frequencies for the prominent cavity resonator modes m n are shown in figure 2-5. The graph compares the calculated cavity mode resonance frequencies with the measured microstrip disk return loss as a function of frequency from 2 to 10 GHz. The data were measured for a microstrip disk antenna with a 4.7 cm diameter on a .16 cm teflon fiberglass substrate.

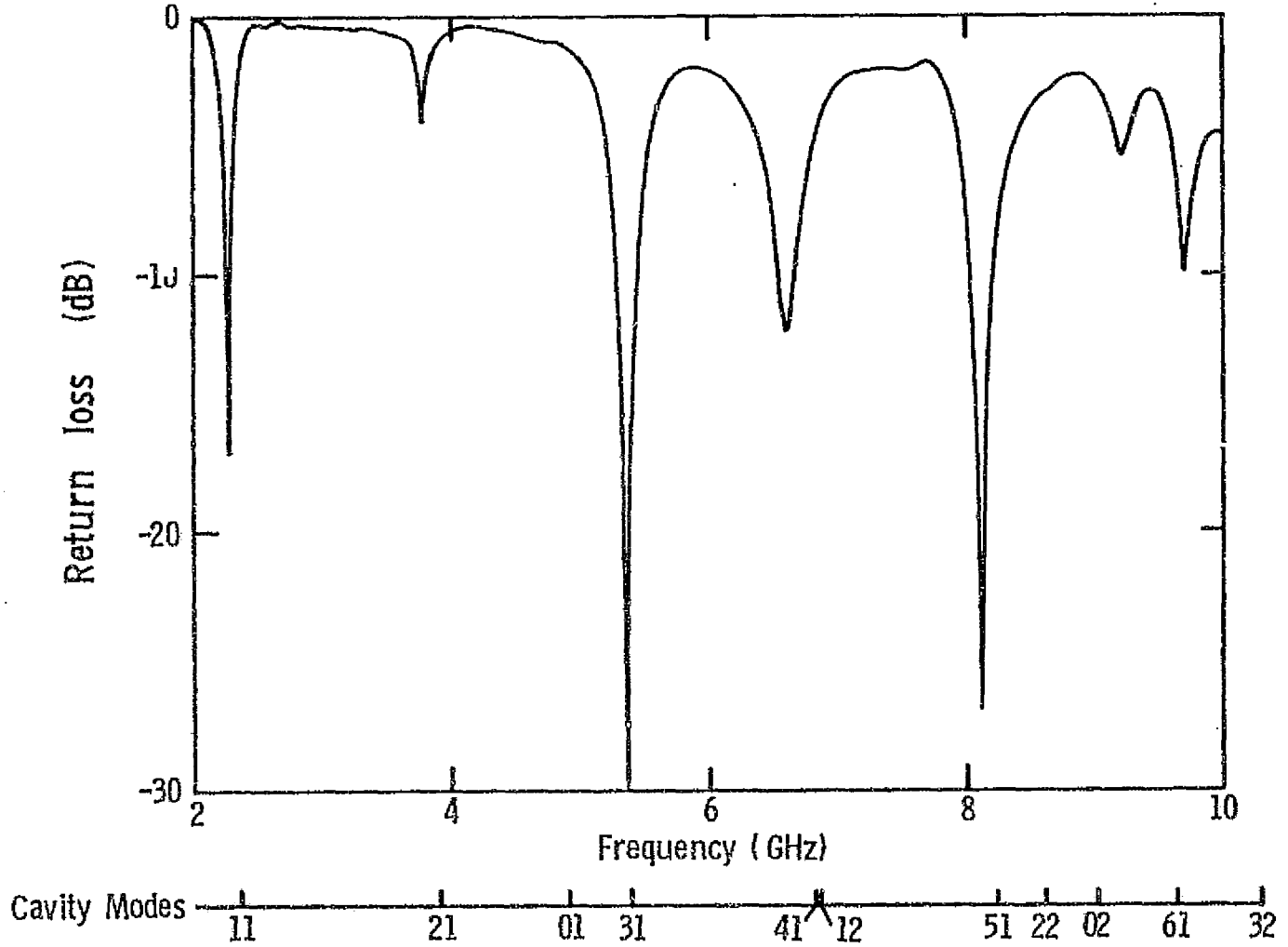

Figure 2-5. Return loss and cavity modes of a 4.7 cm. diameter microstrip disk on a .16 cm. substrate.

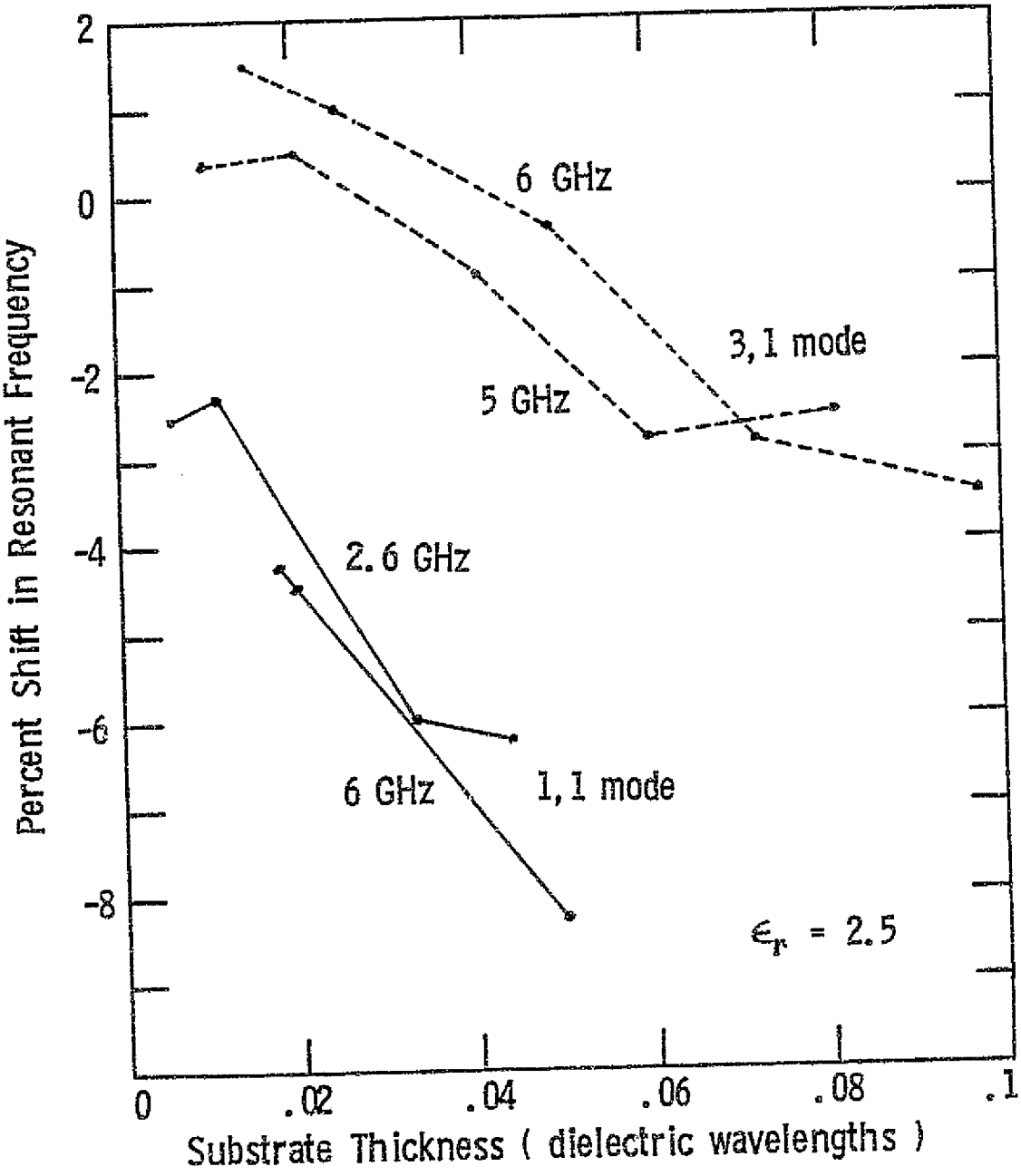

Figure 2-6. Percent shift in resonant frequency from the cavity calculation versus dielectric thickness.

Experimental resonant frequency measurements are compared with the calculated cavity frequencies in figure 2-6. These experiments show that the resonant frequency measurements for the (1, 1) mode are less than the calculated cavity frequencies.

The resonant frequency can be calculated more accurately by other methods. For example, Wolff and Knoppick [16] calculate the capacitance of circular microstrip disk capacitors. The influence of the fringing field on the resonant frequencies is calculated from the microstrip edge capacitances. These frequencies are calculated from a resonator model employing an effective radius and a dynamic dielectric constant. These models neglect the effect of the feed probe. Therefore, empirical data is necessary in the design process to obtain the desired resonant frequency of the microstrip antenna.

Radiation patterns.- The radiation pattern of a microstrip disk antenna is similar to the pattern of an open end circular wave guide. Figures 2-7 and 2-8 compare the measured and calculated E-plane and H-plane patterns of the microstrip and waveguide antennas. The microstrip antenna resonates at 5 GHz with a .34λ diameter on a .16 cm. teflon fiberglass substrate. The antenna is mounted on a ten wavelength square ground plane. The calculated circular wave guide pattern includes the oscillatory variations with angle due to the finite ground plane edges. This is accomplished by expressing the radiated field as

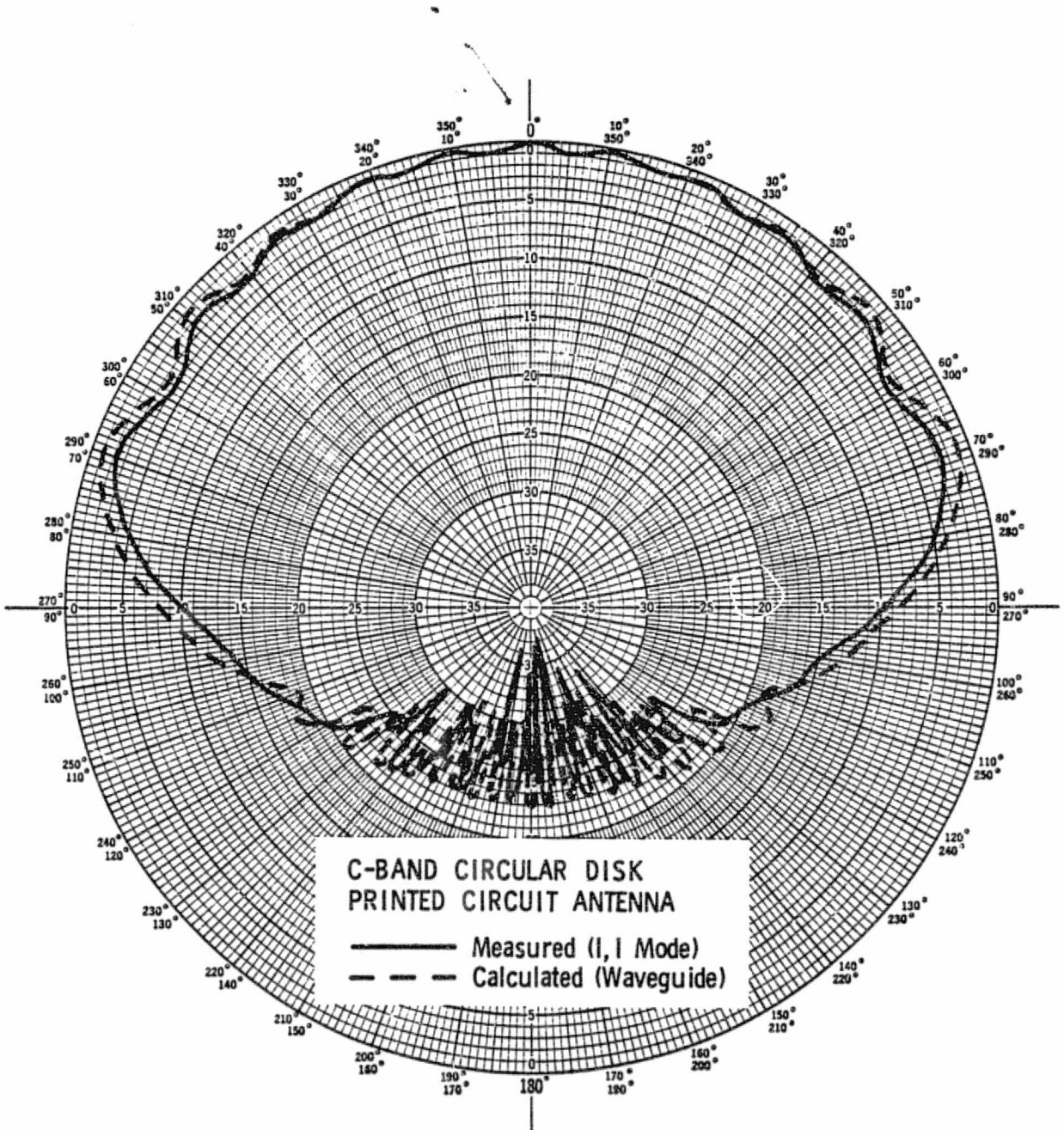

Figure 2-7. E-plane pattern at 5 GHz. on a 62 cm. ground plane.

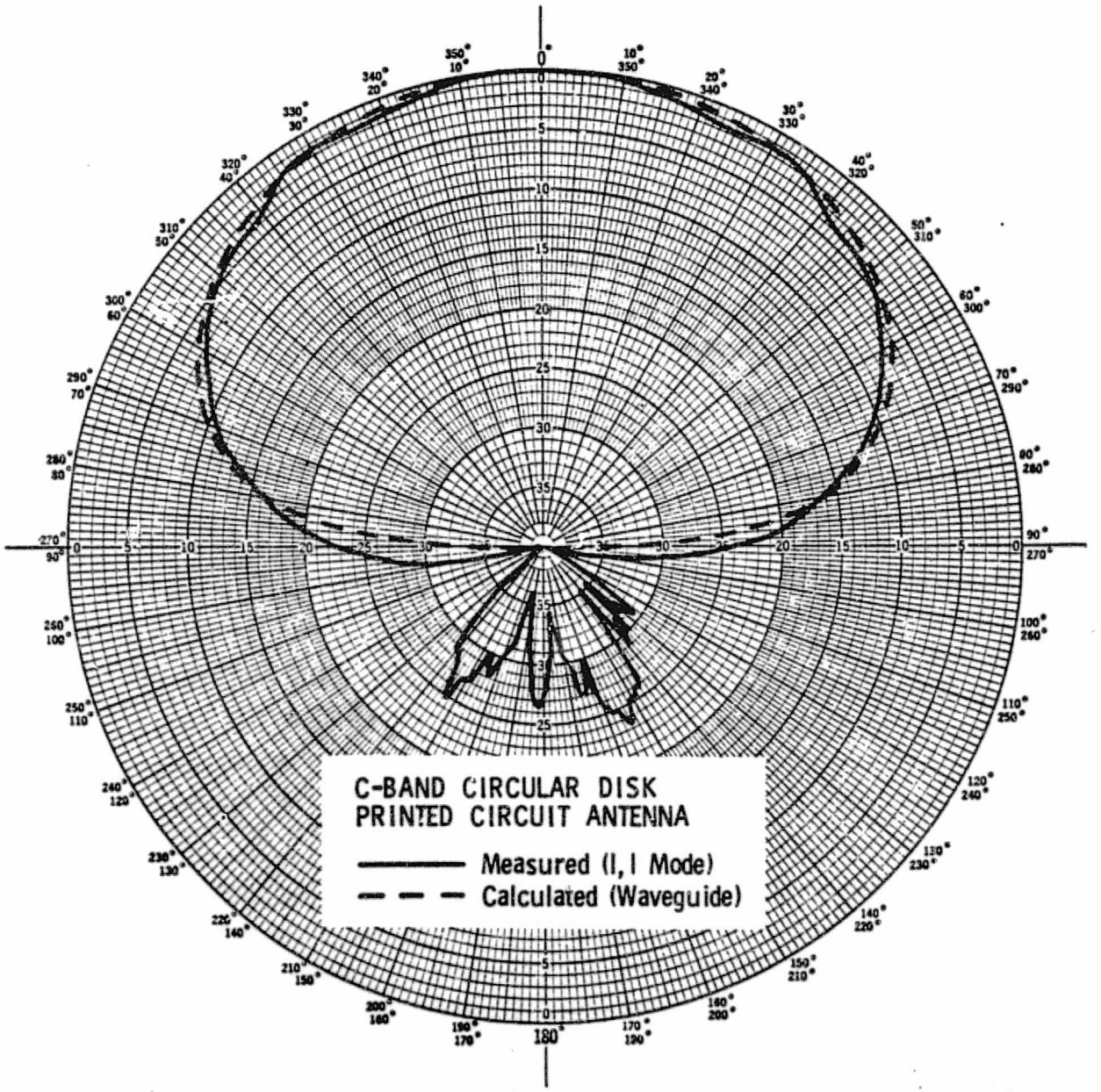

Figure 2-8. H-plane pattern at 5 GHz. on a 62 cm. ground plane.

a superposition of the field on an infinite ground plane [20] and the singularly diffracted fields from the ground plane edges [17].

The circular waveguide aperture model with an infinite ground plane is very often a satisfactory model for array calculations. The circular aperture and the metal microstrip radiating disk are the same diameter, .34 wavelengths.

This circular waveguide is excited in the dominant transverse mode TE_{11}. And the radiated patterns are computed from integral transforms expressed by Bailey [20]. These radiation fields are

$$E_\phi \approx -j(1+\Gamma)\, J_1(X_{11})\, \frac{e^{jk_0 r}}{r} \left\{ \frac{k_0 a \cos\theta \cos\phi\, J_1'(k_0 a \sin\theta)}{1 - \left[\frac{k_0 a}{X_{11}} \sin\theta\right]^2} \right\} \tag{2.5}$$

$$E_\theta \approx -j(1+\Gamma)\, J_1(X_{11})\, \frac{e^{jk_0 r}}{r} \left\{ \frac{\sin\phi\, J_1(k_0 a \sin\theta)}{\sin\theta} \right\} \tag{2.6}$$

where r, θ, ϕ are spherical coordinates and the aperture geometry is defined in figure 2-9. The propagation constant in free space is k_0, a is the waveguide radius, J_1 is the Bessel function of first kind of order 1, X_{11} is the first root of $J'_1(X) = 0$, and Γ is the reflection coefficient. The radiation pattern is the square root of the sum of the terms in braces. The calculated E-plane and H-plane patterns are plotted in figure 2-10.

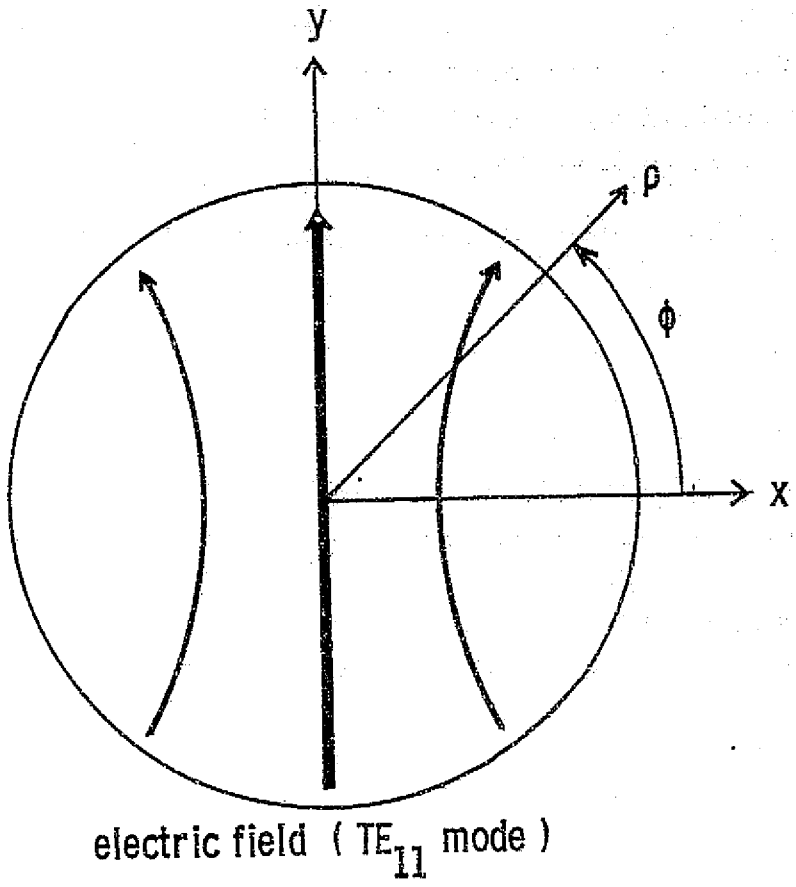

Figure 2-9. Geometry of the circular waveguide fed aperture.

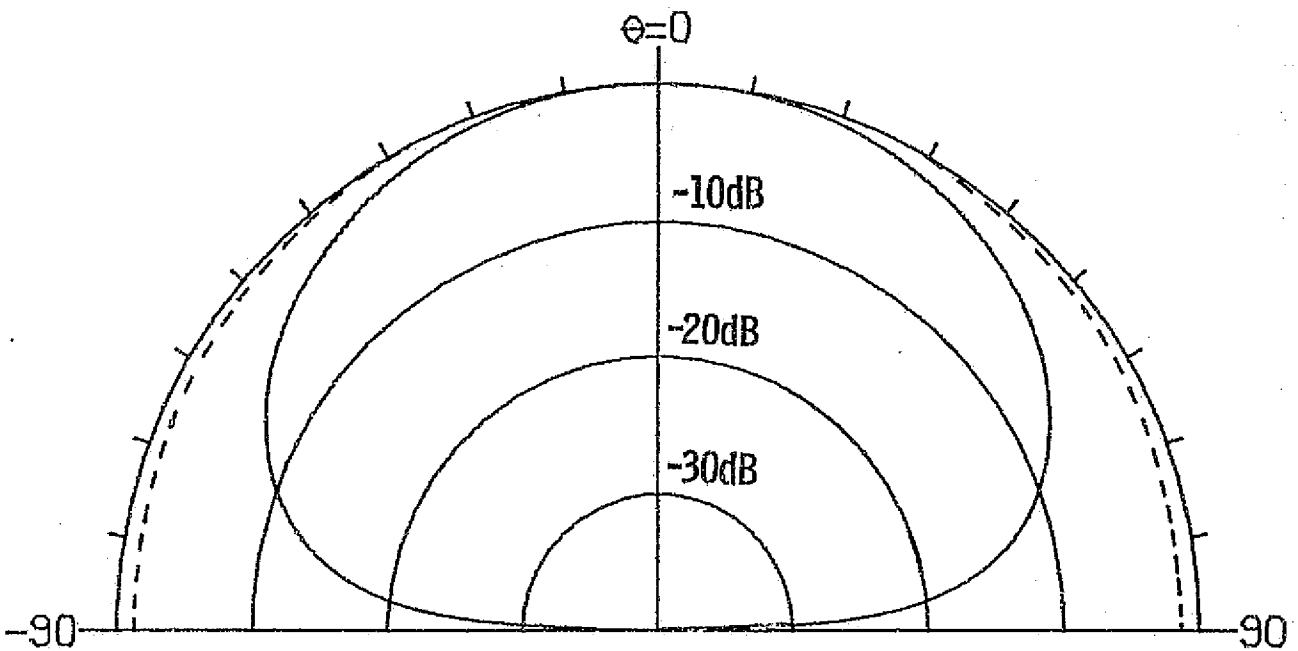

Figure 2-10. Pattern of a circular aperture on an infinite ground plane.

The wire grid model. - The radiation mechanism of the microstrip antenna is not completely understood yet. Agrawal and Bailey [21] explain the radiation mechanism in terms of currents on the copper radiator. They analyze the microstrip antenna as a fine wire grid immersed in a dielectric medium. Richmonds' Reaction formulation [22] is used to evaluate the piecewise sinusoidal currents on the wire grid segments. The calculated results are modified to account for the finite dielectric discontinuity. A round microstrip element and the wire grid model are shown in figure 2-11a.

A comparison of the calculated and measured radiation patterns and impedance plots are shown in figures 2-11b and 2-12. The above calculations are compared with a test antenna which has a very thick dielectric cover, greater than two wavelengths.

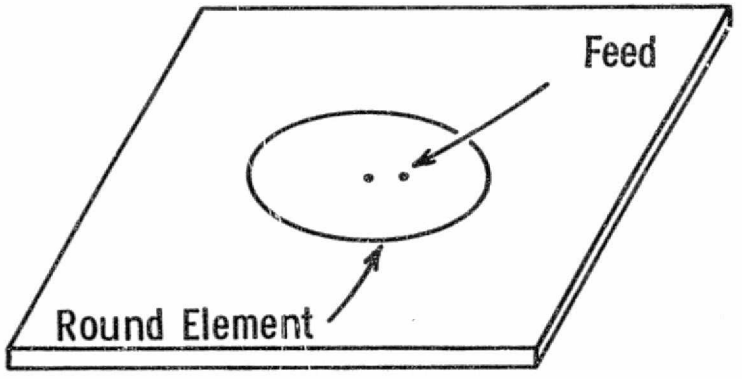

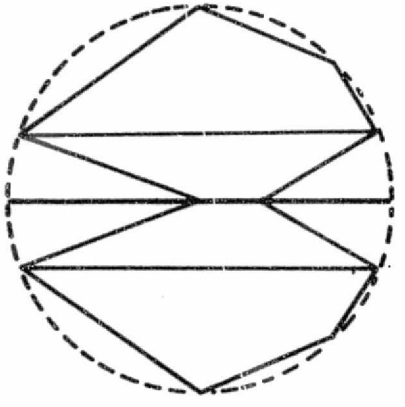

Figure 2-11a.
Round Microstrip Antenna and the Wire Grid Model of the Antenna

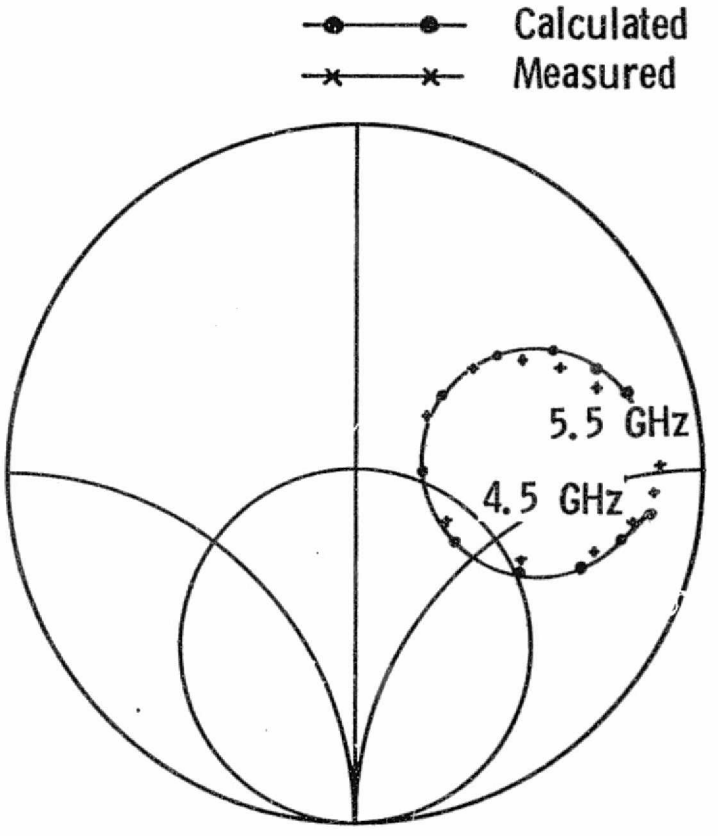

Figure 2-11b.
Input Impedance of Round Microstrip Antenna as a Function of Frequency

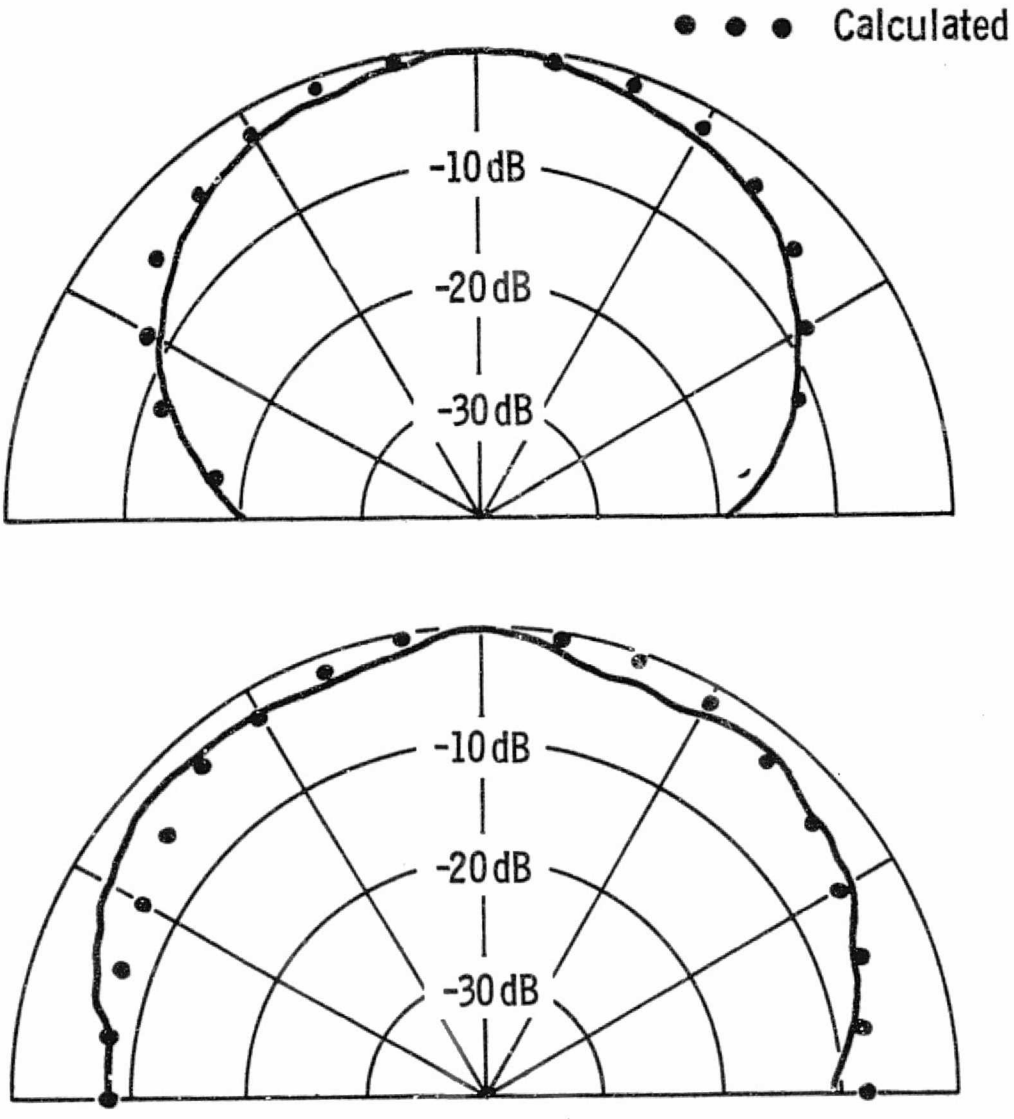

Figure 2-12.
H- and E-Plane Power Patterns for Round Microstrip Antenna fed from Behind

Array Design

Many antenna applications cannot be satisfied by a simple antenna element. These applications require a combination of several identical antennas to form a single antenna array.

This section examines the factors which have a major influence of the array performance. These factors are the spatial distribution of the individual radiators and their excitation voltage.

The general array characteristics are obtained from a few simple equations. Consider a planar array of radiating elements in the x-y plane, figure 2-13. The electrical field strength $\overline{E}$ in the far field of the array which radiates power P_{rad} is

$$\overline{E} = E\hat{p} \cdot g \tag{2.7}$$

Collin and Zucker [23] state

$$E = \sqrt{\frac{P_{rad}}{2\pi\ \zeta_o}}\ \frac{e^{-jk_o r}}{r}\ g(\theta,\phi)\ f(\theta,\phi) \tag{2.8}$$

where $\hat{p}$ is the complex polarization unit vector,

ζ_o is the intrinsic admittance of free space,

$g(\theta,\phi)$ is the radiation pattern of an isolated radiating element, and

r, θ, ϕ are spherical coordinates.

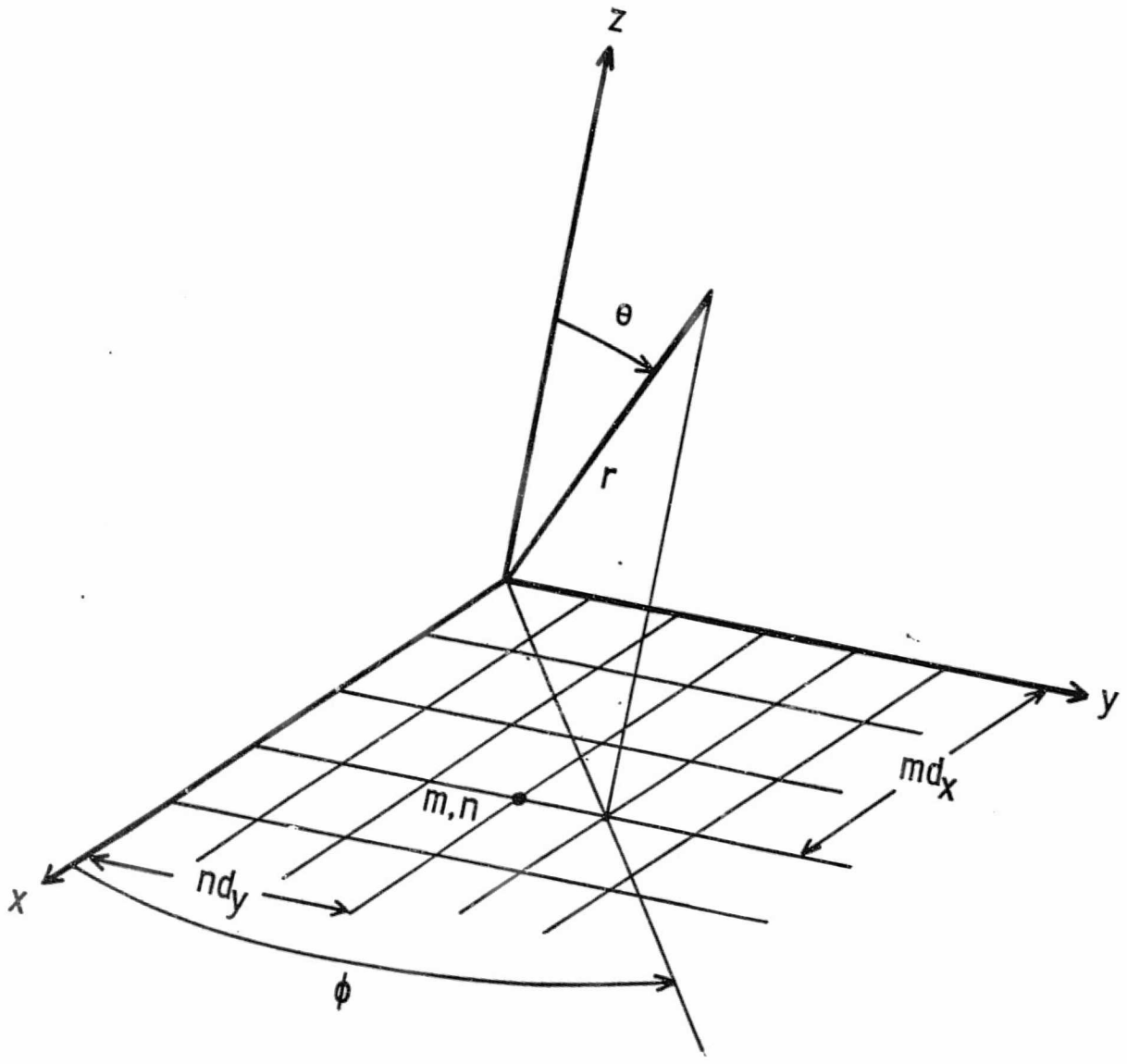

Figure 2-13. Array coordinate system.

The array factor is

$$f(\theta,\phi) = \sum_{m=1}^{M}\sum_{n=1}^{N} V_{mn}\, e^{j(2\pi/\lambda)(md_x \sin\theta\cos\phi + nd_y \sin\theta\sin\phi)} \tag{2.9}$$

where V_{mn} is the complex excitation to element (m,n) and

λ is the wavelength.

Antenna performance is often described in terms of antenna power patterns. The antenna patterns provide information on the antenna beamwidth, sidelobes, antenna noise temperature, and beam efficiency. The total power pattern is $|g(\theta,\phi)\, f(\theta,\phi)|^2$.

Gain.- The gain of an antenna is an important measure of performance. There are two types of gain: directive gain, directivity, considers the antenna to be lossless, and, gain which includes all losses.

The directivity $D(\theta,\phi)$ measures the spatial distribution of radiated energy. The directivity is defined as the ratio of the radiation intensity $\Phi(\theta,\phi)$ to the average radiation intensity,

$$D(\theta,\phi) = \frac{\Phi(\theta,\phi)}{\Phi_{av}} \tag{2.10}$$

where $\Phi(\theta,\phi)$ is the power density per unit solid angle in the direction (θ,ϕ).

Since there are 4π steradians of solid angle over the sphere and

$$\Phi(\theta,\phi) = \frac{1}{4\pi} P_{rad} \left| g(\theta,\phi)\ f(\theta,\phi) \right|^2, \tag{2.11}$$

the directivity can be expressed as

$$D(\theta,\phi) = \frac{\Phi(\theta,\phi)}{P_{rad}/4\pi} = \frac{\Phi(\theta,\phi)}{\frac{1}{4\pi}\int_{4\pi} \left| g(\theta,\phi)\ f(\theta,\phi) \right|^2 d\Omega} \tag{2.12}$$

where Ω is a solid angle. This indicates that the directivity can be determined by integrating the radiation pattern, see reference [24]. Figure 4-20 graphs the directivity for 1, 8, and 64 microstrip elements. This data was obtained by integrating the measured radiation patterns $\left| g(\theta,\phi)\ f(\theta,\phi) \right|^2$.

An important design approximation to the maximum directivity is expressed by Wolff [35]

$$D_{max} = \frac{41253}{\theta_B\ \Psi_B} \tag{2.13}$$

where θ_B and Ψ_B are the orthogonal half-power beamwidths.

The gain includes all losses associated with the antenna system. The total power supplied to the antenna P_{tot} is the sum of the radiated power P_{rad} and the dissipated power P_{loss}:

$$P_{tot} = P_{rad} + P_{loss} \tag{2.14}$$

The efficiency η of the antenna is defined by

$$\eta = \frac{P_{rad}}{P_{tot}} . \tag{2.15}$$

The gain becomes

$$G(\theta,\phi) = \frac{\Phi(\theta,\phi)}{(1/4\pi)P_{tot}} = \eta|f(\theta,\phi)\ g(\theta,\phi)|^2 \tag{2.16}$$

or

$$G(\theta,\phi) = \eta\ D(\theta,\phi) \tag{2.17}$$

The half power beamwidth of the radiation pattern is determined by the number of elements, the element spacing, the excitation voltages, and the element pattern.

The number of elements.- The number of elements N for a given half power beamwidth θ_B is approximated by

$$N \approx \frac{68.8\lambda}{\theta_B(\lambda/2)} + 1 . \tag{2.18}$$

This expression was derived for a cosine line source to obtain low sidelobes, reference [35].

The 64 element antenna array was designed for a 20 degree half power beamwidth. The above formula requires 8 elements in each orthogonal plane to produce a pencil beam. The 64 elements are arranged in a square lattice of 8 elements on each side, figure 1-3.

Element spacing.- The beamwidth also depends on the linear dimension of the array or the spacing between elements. The half power beamwidth θ_B for a given element spacing d_x is approximated by

$$\theta_B \approx \frac{68.8}{(N-1)d_x} \text{ , (degrees)} \tag{2.19}$$

where N is the number of elements, and

d_x is the spacing in wavelengths.

The half power beamwidth derived for a cosine line source is plotted in figure 2-14 as a function of the element spacing for 8, 16, and 32 elements. The line source model is not accurate for small arrays. The beamwidth of microstrip arrays with cosine tapers can be estimated with the circular waveguide model. The radiation pattern for the waveguide model $|g(\theta,\phi)\ f(\theta,\phi)|^2$ was calculated for a 0.34λ diameter waveguide on an infinite ground plane for 8, 16, and 32 elements, figure 2-14. The data begins at .34λ spacing since the elements cannot be spaced closer than the disk diameter.

The spacing between elements determines the location of grating lobes and the maximum beam scan angle. Since only one main beam is

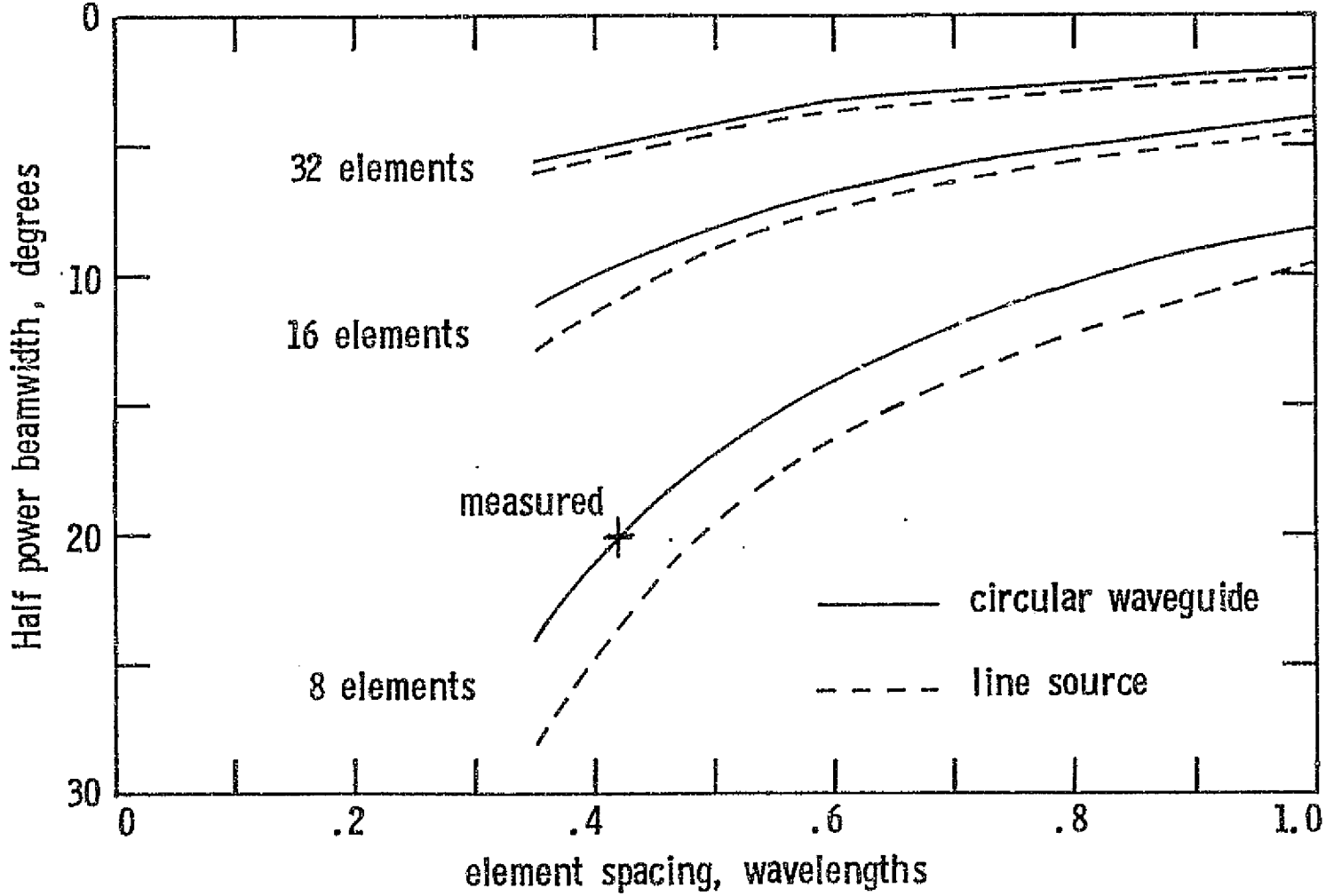

Figure 2-14. Half power beamwidth of microstrip arrays with cosine tapers.

required, the element spacing d_x is restricted to less than one free space wavelength λ. The element spacing d_x is also limited by the largest scan angle of the main beam from the array normal (θ_s),

$$d_x < \frac{\lambda}{1 + \sin |\theta_s|} \tag{2.20}$$

where d_x is the element spacing in wavelengths.

Element excitation. The complex excitation voltage controls the radiation pattern beamwidth, sidelobe level, and beam pointing direction. Each radiating element of the antenna (m,n) is excited by a voltage V_{mn} from the feed network.

The amplitude distribution for this design reduces the sidelobes and broadens the half power beamwidth. The amplitude distribution has a cosine taper such that the elements in the center have the highest voltage and the end elements have the lowest voltage as shown below.

Cosine Distribution

Element Number	Amplitude	Phase
1	-20.17 dB	0^o
2	-11.09 dB	0^o
3	-7.58 dB	0^o
4	-6.15 dB	0^o
5	-6.15 dB	0^o
6	-7.58 dB	0^o
7	-11.09 dB	0^o
8	-20.17 dB	0^o

Figure 2-15 shows the radiation patterns which result from excitations with and without an amplitude taper. The uniform taper produces -13 dB sidelobes. However, the cosine taper has -23.5 dB sidelobes with an increased beamwidth.

The main beam of the antenna points in a direction that is normal to the phase front. θ_s is the angle of scan measured from broadside and ϕ_s is the plane of scan measured from the X axis, figure 2-13. The phase front can be adjusted to scan the beam by controlling the phase of excitation α_{mn} to each radiating element. The voltage $\overline{V}_{mn}$ applied to each element is

$$\overline{V}_{mn} = |V_{mn}|e^{-j\alpha_{mn}} \tag{2.21}$$

where the phase of excitation to element (m,n) is

$$\alpha_{mn} = (2\pi/\lambda)(md_x \sin\theta_s \cos\phi_s + nd_y \sin\theta_s \sin\phi_s) . \tag{2.22}$$

The subscripts s refer to the array steering commands. The phase increments between consecutive columns and rows are respectively

$$\Psi_x = (2\pi/\lambda)\, d_x \sin\theta_s \cos\phi_s \tag{2.23}$$

and

$$\Psi_y = (2\pi/\lambda)\, d_y \sin\theta_s \sin\phi_s \tag{2.24}$$

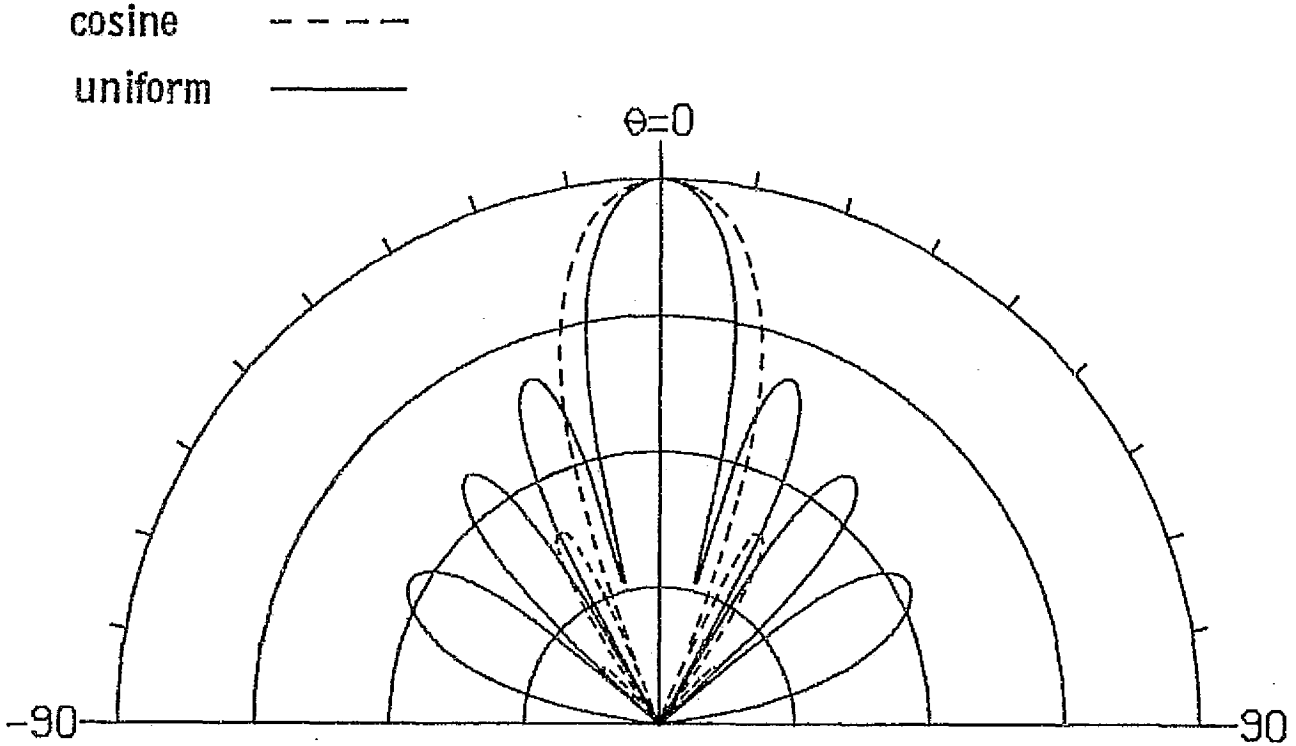

Figure 2-15. Calculated patterns of an 8 element array with uniform and cosine amplitude tapers.

If we consider steering in only the principal plane ($\phi_s = 0$) containing rows of the rectangular array then the phase increments become

$$\Psi_x = (2\pi/\lambda)\, d_x \sin \theta_s \tag{2.25}$$

$$\Psi_y = 0 \tag{2.26}$$

Dielectric Cover Design

The thickness, dielectric constant, and loss tangent of the dielectric cover should be known early in the design stage. These properties affect the bandwidth, resonant frequency, efficiency, and mutual coupling. For example, figure 2-16 shows that the bandwidth of the microstrip disk radiator increases as the dielectric cover thickness increases, and the resonant frequency decreases as the dielectric cover increases.

Many applications require that a bonded dielectric cover protect the radiating elements. This provides protection against heat, physical damage, and the environment.

Another common application is to increase the minimum breakdown power. This is accomplished by the cover capturing electrons (attachment) in its field and preventing them from generating ions. The cover also increases the minimum breakdown power by providing a smooth surface to keep the voltage gradients at a minimum. Munson [13] claims a teflon fiberglass laminate 0.0397 cm. thick improves the power breakdown 2.5 times. Munson also reported kilowatt range peak pulse powers for covered microstrip antennas from 1 to 10 GHz. Finally, Howell [25] tested a UHF microstrip disk with a teflon tape cover at a 78 watt average power level through the critical pressure region.

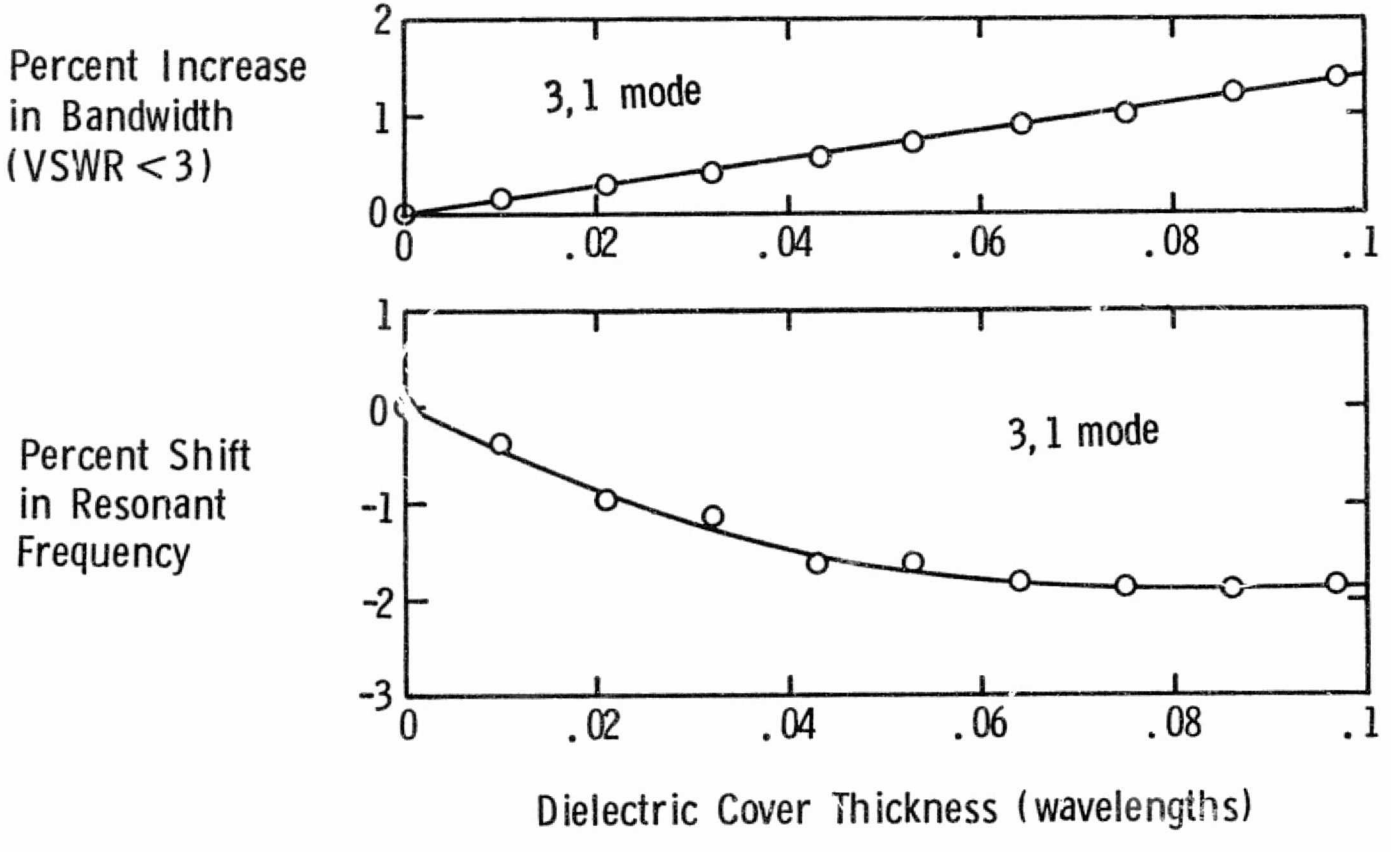

Figure 2-16. Bandwidth and resonant frequency shift versus dielectric cover thickness.

Mutual Coupling

The mutual coupling between radiating elements is the cause of an apparent change in the element impedance and element pattern. For example, in a scanning phased array the impedance of each radiating element varies as the main beam is scanned. This mismatch affects the level of the radiated power, the shape of the radiation pattern, and spurious lobes. In addition, an array that is well matched at broadside may have an angle of scan in which most of the power is reflected into the feed network.

In order to describe the effects of mutual coupling we represent the antenna array as an N port linear system which can be described by a scattering matrix. The scattering matrix represents the coupling coefficients and reflection coefficients in terms of incident voltages (V_n^+) and reflected voltages (V_n^-) at each port.

$$\begin{bmatrix} V_1^- \\ V_2^- \\ \vdots \\ V_n^- \end{bmatrix} = \begin{bmatrix} S_{11} & S_{12} & S_{13} & \cdots & S_{1n} \\ S_{21} & S_{22} & S_{23} & \cdots & S_{2n} \\ \vdots & \vdots & \vdots & & \vdots \\ S_{n1} & S_{n2} & S_{n3} & \cdots & S_{nn} \end{bmatrix} \begin{bmatrix} V_1^+ \\ V_2^+ \\ \vdots \\ V_n^+ \end{bmatrix} \tag{2.27}$$

or

$$[V^-] = [S][V^+] \tag{2.28}$$

where [S] is the scattering matrix as expressed by Collin [26].

The reflection coefficient (Γ_n) of element n is obtained by dividing the reflected voltage by the incident voltage

$$\Gamma_n = \frac{V_n^-}{V_n^+} = S_{n1}\frac{V_1^+}{V_n^+} + S_{n2}\frac{V_2^+}{V_n^+} + \cdots S_{nn}\frac{V_n^+}{V_n^+} \tag{2.29}$$

For a planar array, figure 2-13, the reflection coefficient of the element mn is

$$\Gamma_{mn} = \sum_{\text{all}_p}\sum_{q} S_{mn,\,pq}\,\frac{V_{pq}^+}{V_{mn}^+}\,. \tag{2.30}$$

But, if the main beam is scanned in the direction (θ_s, ϕ_s), then the reflection coefficient becomes

$$\Gamma_{mn}(\theta_s,\ \phi_s) = \sum_{\text{all}_p}\sum_{q} S_{mn,\,pq}\left|\frac{V_{pq}^+}{V_{mn}^+}\right| e^{+j\alpha_{mn}} \tag{2.31}$$

where

$$\alpha_{mn} = (2\pi/\lambda)[(m - p)d_x \sin\theta_s \cos\phi_s + (n - q)d_y \sin\theta_s \sin\phi_s]. \tag{2.32}$$

The impedance can now be determined from the above reflection coefficient. The reflection coefficient causes an impedance variation relative to a matched beam at broadside:

$$\frac{Z_{mn}(\theta,\phi)}{Z_{mn}(0,0)} = \frac{1 + \Gamma_{mn}(\theta,\phi)}{1 - \Gamma_{mn}(\theta,\phi)} \tag{2.33}$$

where $Z_{mn}(\theta,\phi)$ is the active impedance of element mn for a beam scanned in direction (θ,ϕ). The excitation of the radiating element mn is

$$V_{mn} = V_{mn}^{+} - V_{mn}^{-} \tag{2.34}$$

or

$$V_{mn} = V_{mn}^{+}(1 - \Gamma_{mn}). \tag{2.35}$$

The array radiation pattern can now be expressed in terms of the element gain pattern $s(\theta,\phi)$ and the array factor $f(\theta,\phi)$.

$$\begin{aligned} D(\theta,\phi) &= |s(\theta,\phi)\ f(\theta,\phi)|^2 \\ &= \left| s(\theta,\phi) \sum_m \sum_n V_{mn}^{+} \right. \\ &\qquad \left. e^{j(2\pi/\lambda)(md_x \sin\theta\cos\phi + nd_y \sin\theta\sin\phi)} \right|^2 . \end{aligned} \tag{2.36}$$

The element pattern is the actual radiation pattern taken in the array in the presence of all other elements. The pattern also takes into account all coupling effects and mismatches:

$$\left|s(\theta,\phi)\right|^2 = \left|g(\theta,\phi)(1 - \Gamma_{mn})\right|^2 \tag{2.37}$$

where $g(\theta,\phi)$ is the pattern of an isolated element and Γ_{mn} is the active reflection coefficient.

Figure 2-17 shows the measured element patterns $|s(\theta,\phi)|^2$ of a linear 8 element array with E-plane coupling. The patterns are measured by exciting one element and terminating the other seven microstrip elements with fifty ohm loads. The patterns show that there are no serious mismatch effects in the 8 element microstrip array. In general, the coupling effects are more pronounced in larger arrays as shown by Bailey [29]. The dominate ripple in these patterns is caused by the finite ground plane, see figure 2-7.

Mutual coupling coefficients.- The scattering matrix method of computing the variation in the reflection coefficient requires that each mutual coupling coefficient be determined. The mutual coupling coefficients, $S_{mn,pq}$, may be easily measured by exciting one element and terminating each of the other elements in matched loads[18]. The ratio of the induced voltage at element mn to the excitation voltage at element pq gives the amplitude and phase of the coupling coefficient $S_{mn,pq}$. Once these coefficients are determined, they may be substituted into equations (2.31) and (2.36) to determine the mismatch and radiation patterns for any amplitude and phase excitation from the array feed network.

The figure 2-18 shows the measured complex coupling coefficients for an 8 element microstrip array. The end element was excited with the other elements terminated. Next, a swept frequency network analyzer measured the scattering coefficient of each element.

.42 wavelength element spacing

5.5 Ghz

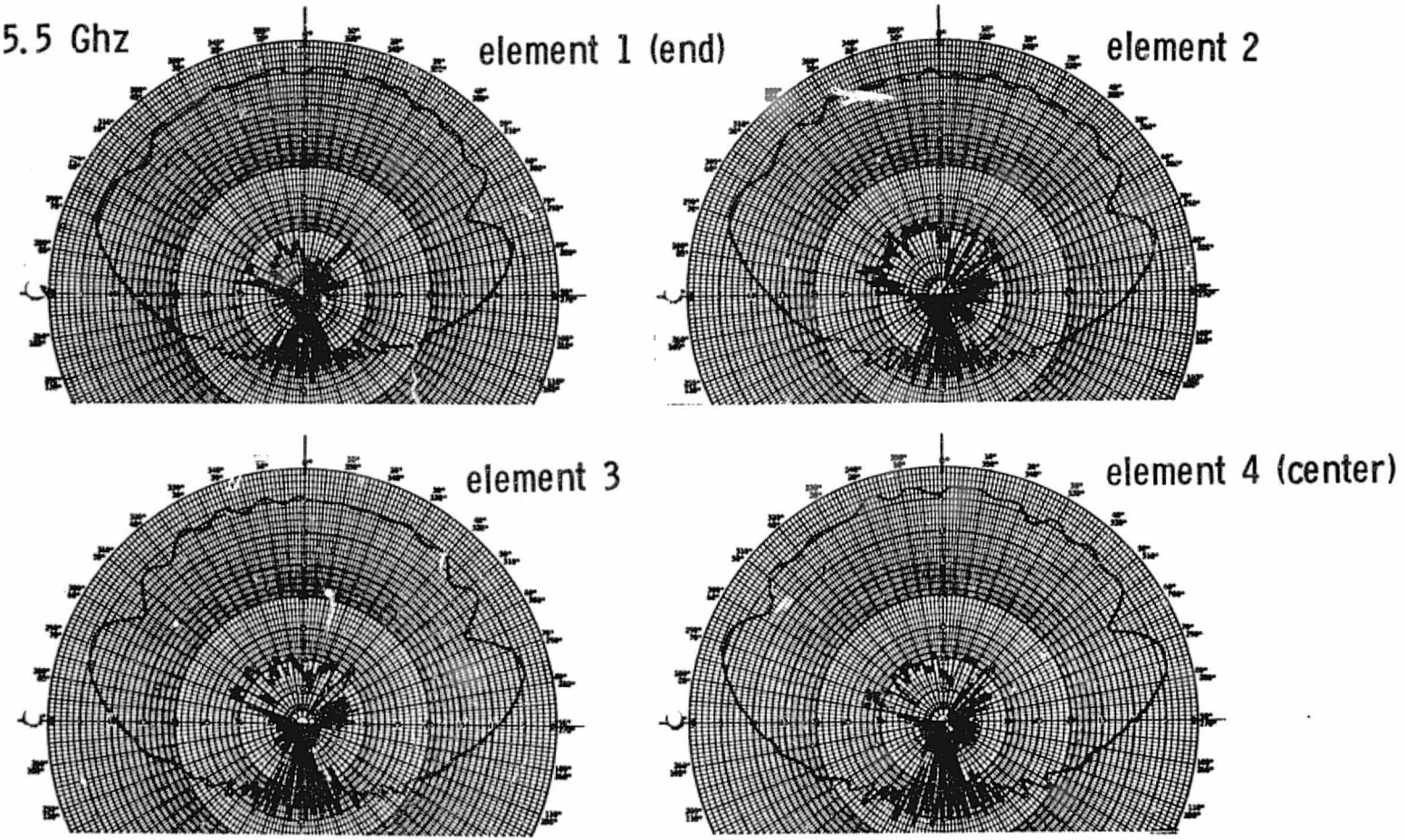

Figure 2-17. E-plane element patterns of an 8 element array with one element excited and the other elements matched.

.16 cm substrate, ϵ_r=2.5

.42 wavelength element spacing

5.5GHz

E-plane coupling

(amplitude, dB
phase, 360° periods)

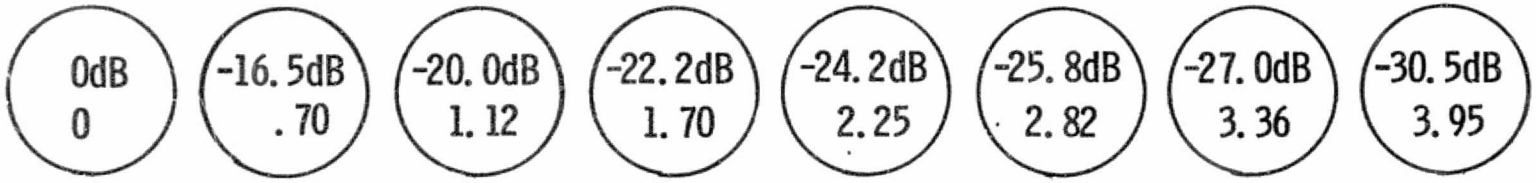

Figure 2-18. Measured mutual coupling coefficients in a microstrip array.

Two element coupling coefficients.- The two element mutual coupling coefficients were measured [27] for various spacings and orientations on a large ground plane. This two element coupling data can be used to estimate the coupling in a large array as discussed in the preceding section and also noted in equations (2.44) and (2.49). Six two element arrays were photo etched on teflon fiberglass laminates, figure 2-19. To obtain data for additional spacings and orientations, the elements were first constructed on two separate laminates and then mounted together on a large ground plane, figures 2-20 and 2-21. The separation between the elements was increased by mounting spacers of various widths between the coupled antennas.

The coupling was measured over a swept frequency range of 4.5 to 6.5 GHz with a microwave network analyzer. A typical graph of this data is shown in figure 2-22. The elements resonated at 5.5 GHz with less than -25 dB return loss. The coupling decreases rapidly as the antenna becomes mismatched off resonance. The maximum coupling occurs at resonance where the elements are well matched.

The coupling amplitude in dB as a function of the spacing between disk centers is shown in figure 2-23. These data are for antennas at resonance with maximum coupling. The H-plane coupling decreases rapidly as the spacing increases. However, the E-plane coupling is very strong. The E-plane coupling decreases slowly for large spacings. The elements appear to couple via a surface wave propagating in the lowest order TM_0 mode. Antenna elements will influence the surface

Figure 2-19. Two coupled microstrip elements on a teflon fiberglass laminate.

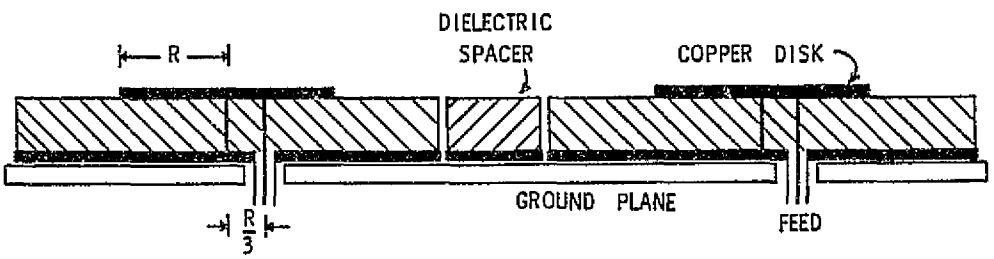

Figure 2-20. Cross section of the coupled disk antennas.

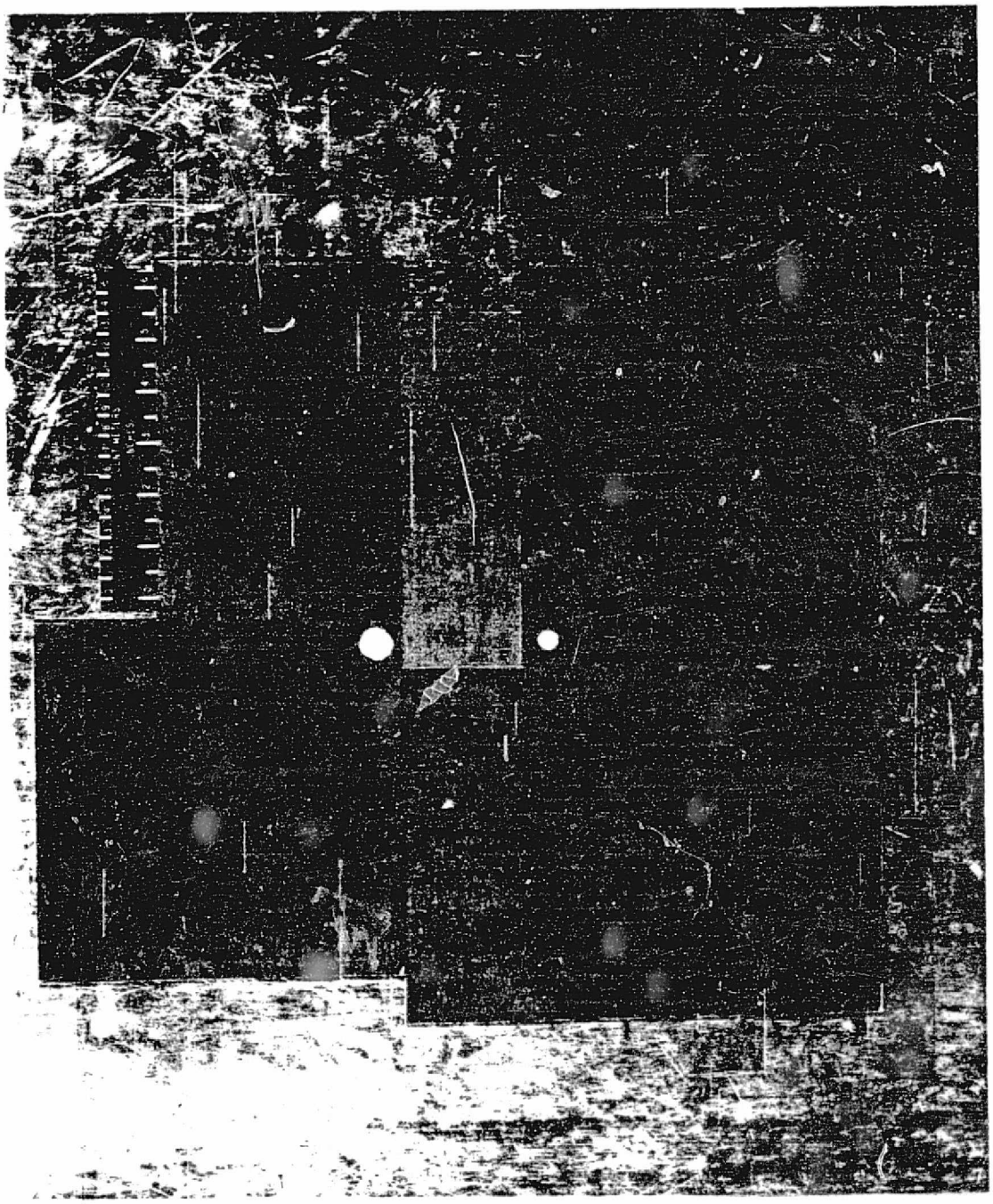

Figure 2-21. Two coupled antennas with dielectric spacers on an aluminum ground plane.

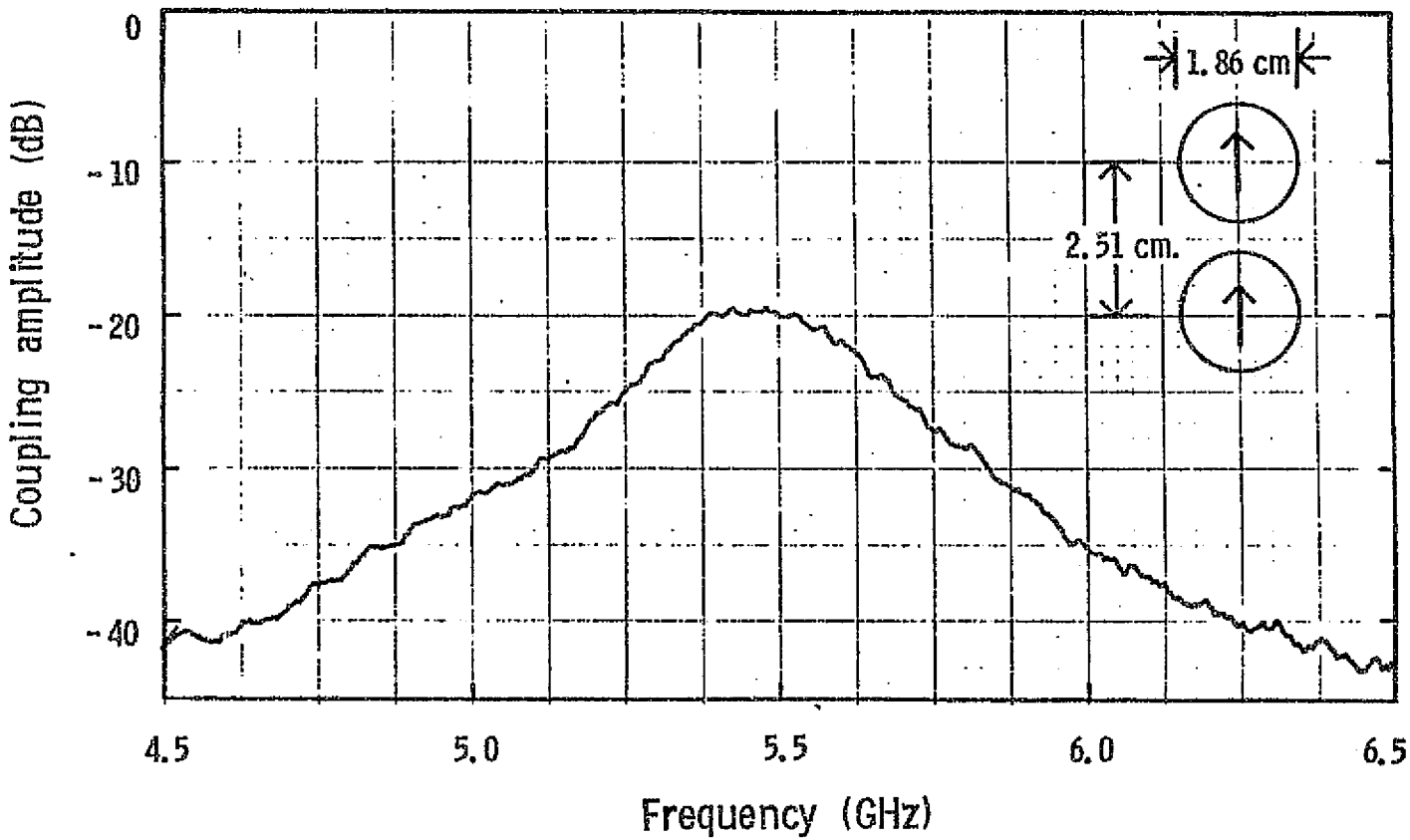

Figure 2-22. Swept frequency coupling amplitude data between two microstrip disks.

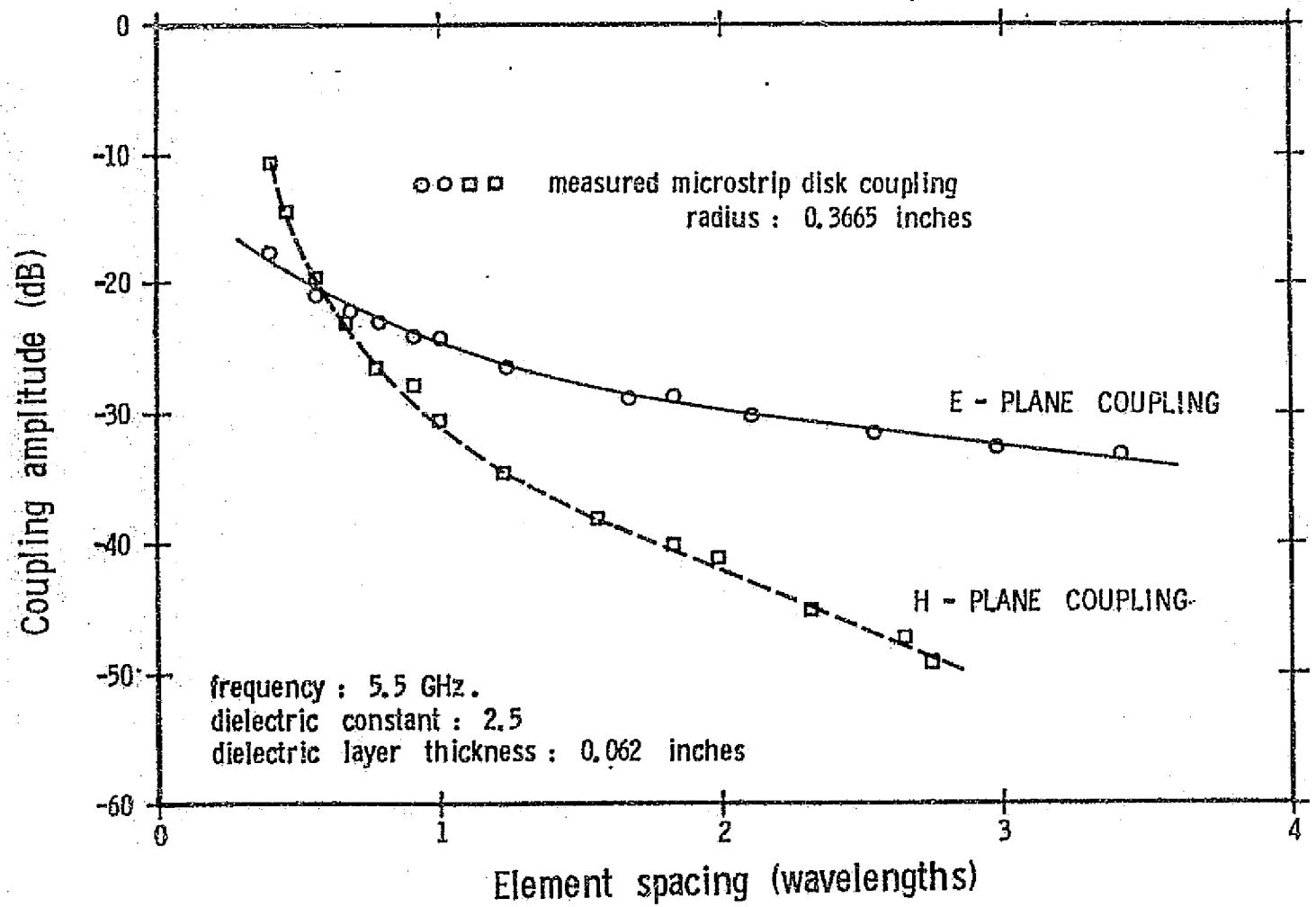

Figure 2-23. Microstrip disk coupling amplitude between two elements.

wave velocity and extract power from the surface wave through mutual coupling and scattering.

The difference in coupling amplitude between six test cases, each on a single dielectric laminate, and the other measurements with dielectric spacers is within the scatter of these data.

The array designer may require mutual coupling data for many more orientations and spacings so a method of estimating coupling is presented. The currents on microstrip disk antennas are postulated to be similar to the electric field distribution for the TE_{11} circular waveguide mode. Therefore, the dual problem of coupling between dielectric covered circular waveguide-fed apertures [28] was used to predict the coupling between the microstrip disks, figure 2-24.

The mutual admittance between two apertures can be determined from a consideration of

$$Y_{ij} = \frac{1}{V_i V_j} \iint_{S_i} [E^{(i)} \times H^{(j)}] \cdot \hat{Z} dS_i \tag{2.38}$$

where V_i and V_j are the normalized modal voltages

$$V_i = \iint_{S_i} E^{(i)} \cdot \hat{e}_i dS_i \tag{2.39}$$

$$V_j = \iint_{S_j} E^{(j)} \cdot \hat{e}_j dS_j \, . \tag{2.40}$$

Figure 2-24. CROSS SECTION OF COUPLED CIRCULAR WAVEGUIDE - FED APERTURES WITH A DIELECTRIC COVER

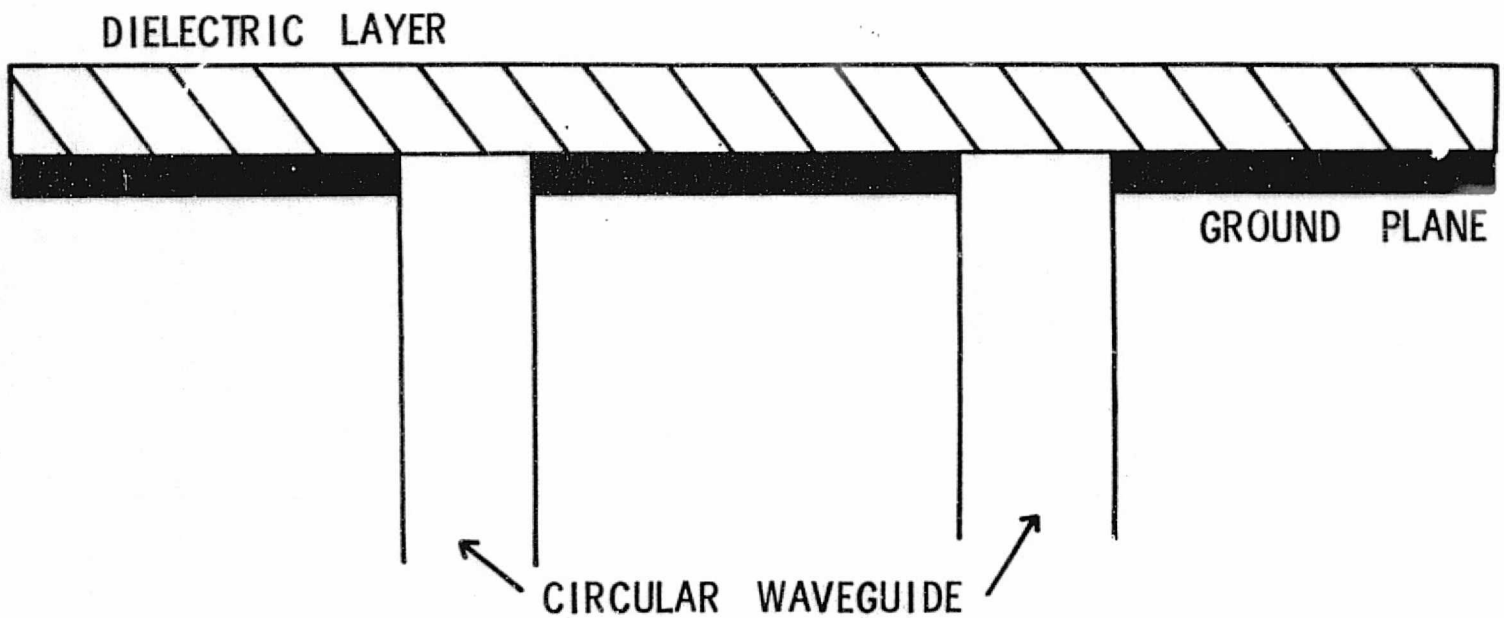

$\hat{e}_i$ and $\hat{e}_j$ are the normalized vector mode functions for the waveguide excitations of the ith and jth apertures. $H^{(j)}$ is the short-circuit magnetic field produced in aperture i by an assumed electric field $E^{(j)}$ in aperture j.

The aperture self-admittance and the mutual admittance form the admittance matrix [Y]. Then the scattering matrix [S] can be determined from the relation

$$[S] = \left[[Y_o] - [Y]\right] \left[[Y_o] + [Y]\right]^{-1} , \tag{2.41}$$

where $[Y_o]$ is a diagonal matrix whose elements are the characteristic admittances of the waveguide modes and $[\cdot]^{-1}$ denotes matrix inversion. The scattering matrix can then be used to study mutual coupling and impedance.

A computer program was developed to calculate the mutual coupling between circular waveguide-fed apertures covered by dielectric layers [29]. Figure 2-25 shows a comparison of the calculated waveguide coupling with the measured microstrip disk coupling data. The microstrip disk substrate is the same thickness as the aperture dielectric cover. The computer program calculates the coupling at 5.5 GHz. This is the resonant frequency of the microstrip antenna; the disk antenna is well matched and the coupling is maximum at this frequency. Therefore, the computer program must be modified to tune each waveguide such that the coupling is maximized. This is accomplished by setting the self-admittance of each waveguide equal to the characteristic admittance.

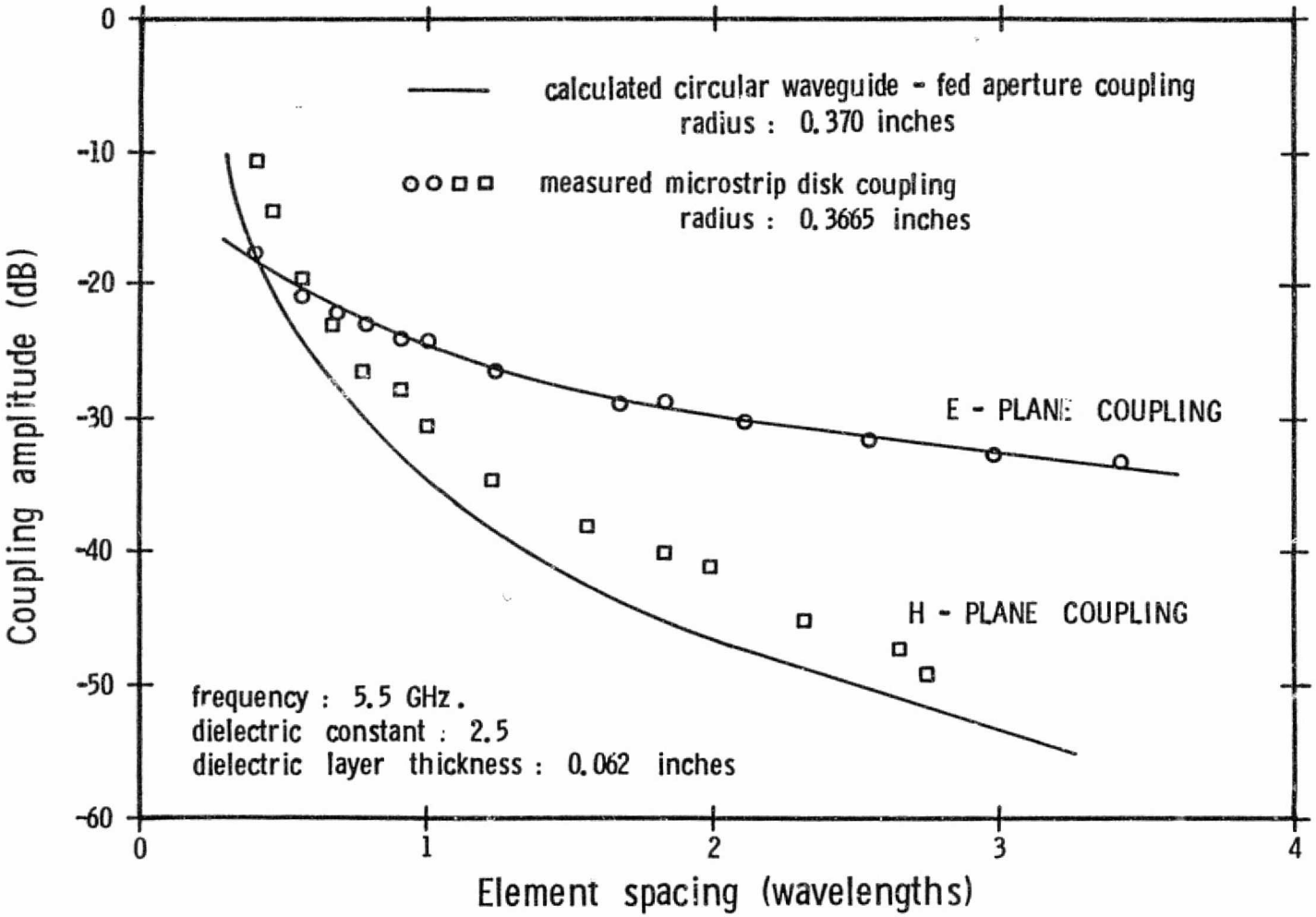

Figure 2-25. Comparison of the calculated and measured two element coupling.

The E-plane calculations estimate the measured data. The calculations predict the high level of coupling for large spacings. However, the H-plane calculations are approximately 4 dB lower than the measured levels of coupling. The waveguide calculations estimate the coupling within one dB as the orientation angle varies from 0 to 55 degrees in figure 2-26. The graph is normalized to the level of E-plane coupling, θ = 0 degrees. The data was measured at resonance with a spacing of 2.3 wavelengths.

The mutual coupling coefficients of the two element arrays and the 8 element array are compared in figures 2-27 and 2-28. The two element data was measured for spacings up to 3.5 wavelengths. The 8 element array element spacing is .42 wavelengths. These data are for the elements at a resonant frequency of 5.5 GHz where the coupling is the maximum.

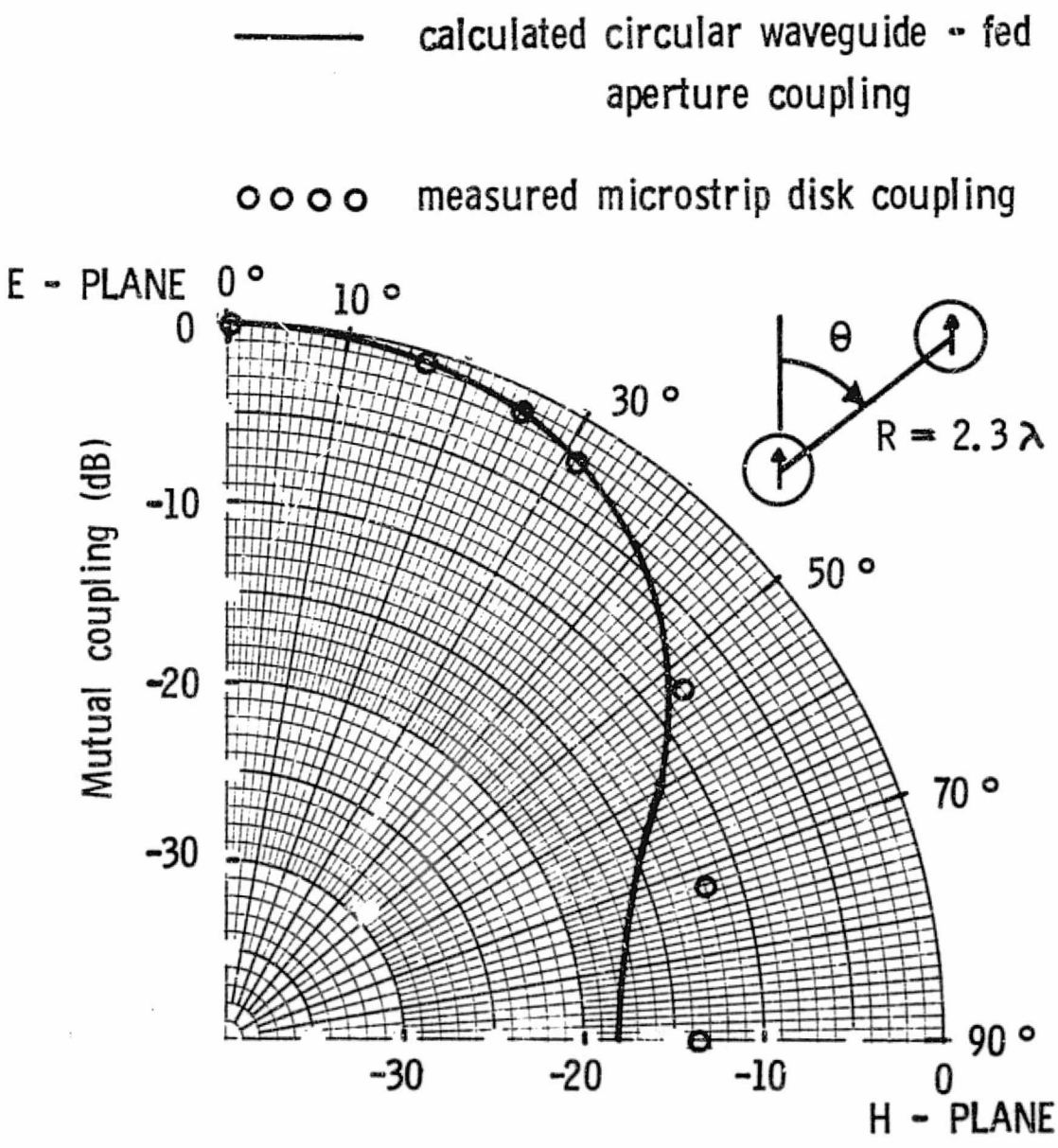

Figure 2-26. Normalized coupling pattern.

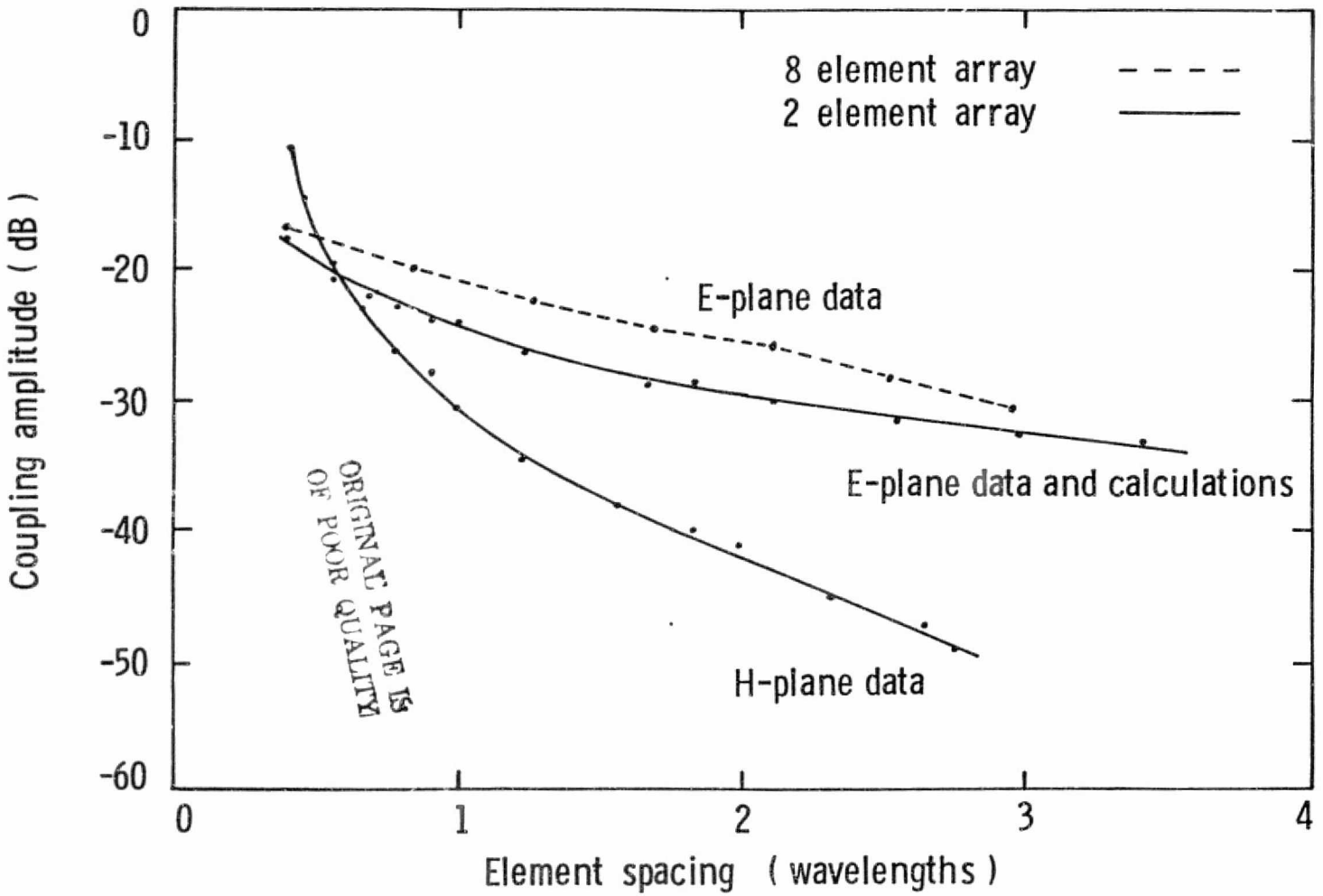

Figure 2-27. Amplitude of the mutual coupling coefficients as a function of spacing.

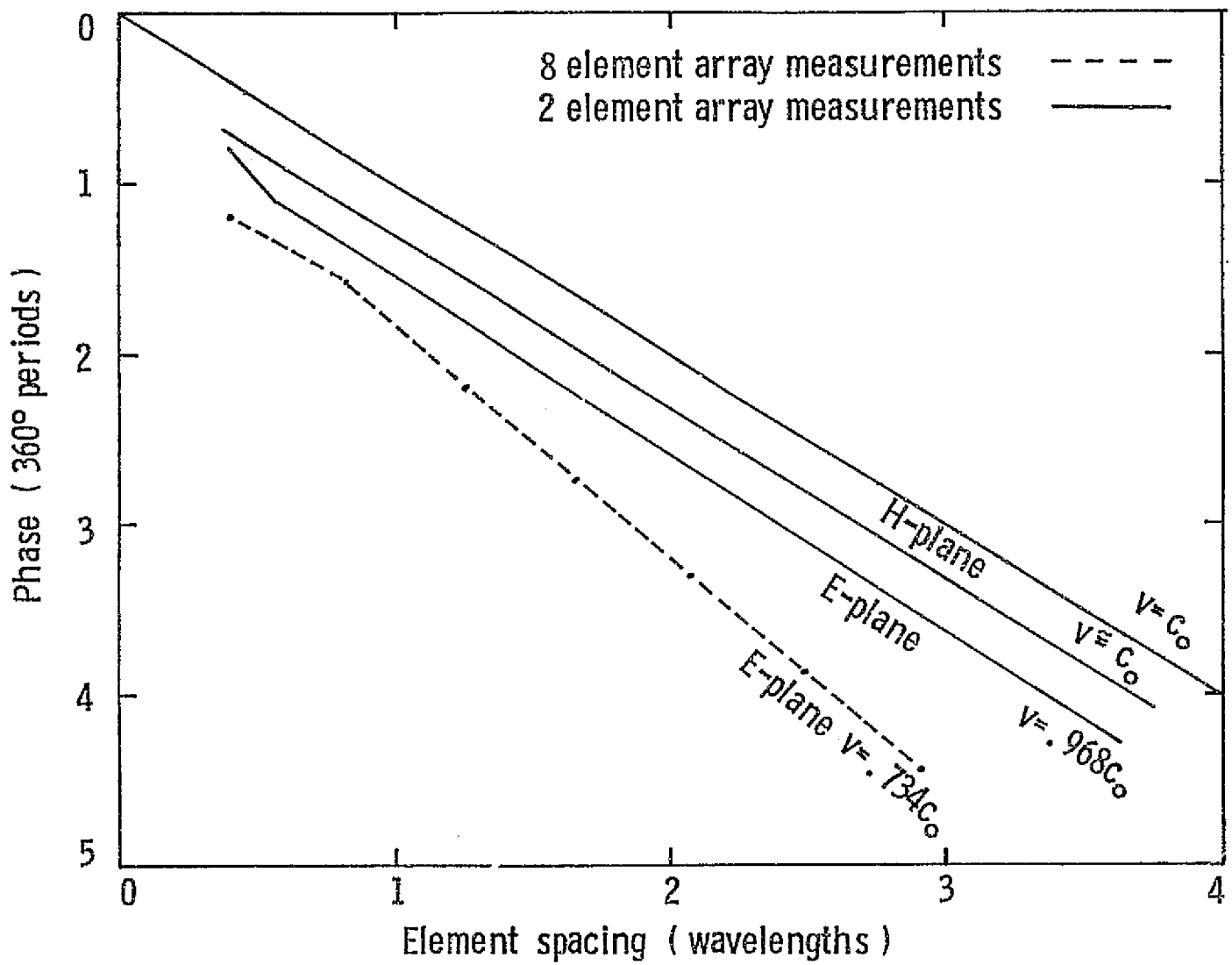

Figure 2-28. Phase of the mutual coupling coefficients as a function of spacing.

Feed Network Design

There are many feed network circuits which can produce a cosine amplitude excitation. For example, the sidelobe reducing cosine amplitude excitation may be obtained by using resistive or reactive attenuators. These feed networks attenuators are placed in the transmission line to each array radiating element.

The losses in this feed network can be estimated by integrating the power intensity under the amplitude distribution function as if the array were a line source. For a cosine excitation with 23dB sidelobes the losses are

$$P_o/P_i = (1/\pi) \int_0^{\pi} \sin^2 x \, d_x = 1/2 \text{ or } 3dB \qquad (2.42)$$

A sidelobe reducing network with a cosine amplitude excitation can be implemented without attenuators [30]. A circuit of this type is the "lossless" Butler factorial matrix. This network produces a cosine distribution utilizing 3dB hybrid branchline couplers and fixed shifters, figure 2-29.

The factorial matrix circuit is analyzed by Butler [9] in terms of the total antenna pattern which is expressed as the sum of two patterns. These two patterns are orthogonal in space such that

$$\int_a^b fg \, d_x = 0 \qquad (2.43)$$

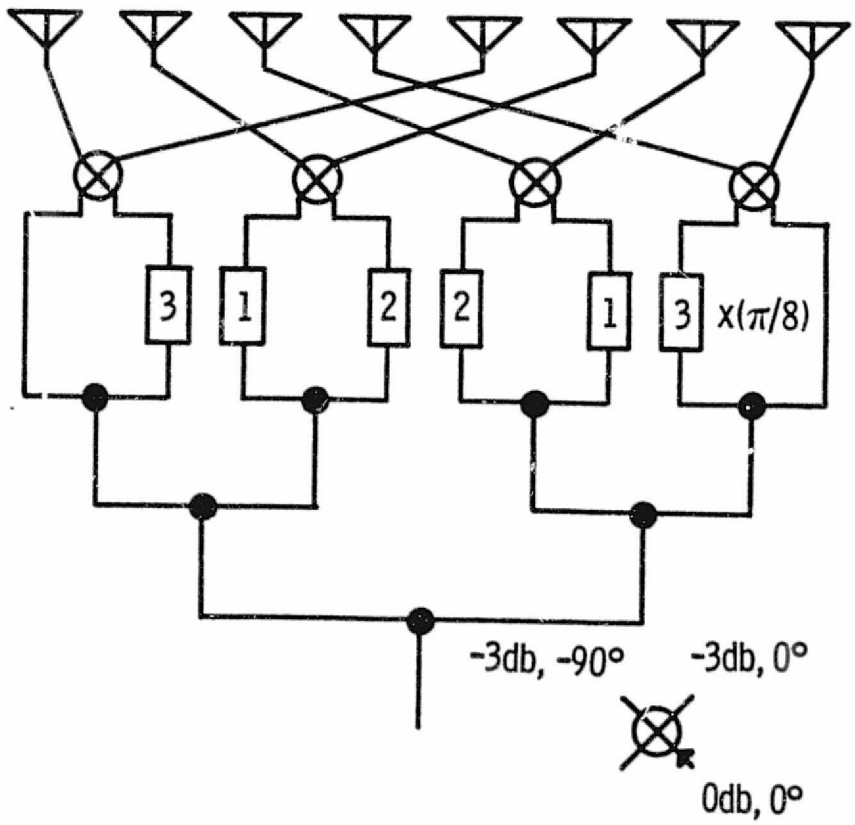

Figure 2-29. The Butler matrix feed network with a cosine amplitude taper.

where f(x) and g(x) are the orthogonal functions over an interval (a,b).

The addition of these two orthogonal beams produces a cosine distribution which can be demonstrated by treating the array as a line source as shown below.

$$I_R = \exp [j\beta] \tag{2.44}$$

$$I_L = \exp [-j\beta] \tag{2.45}$$

Thus, the Butler matrix produces the two above uniform excitations: the first one with a phase change of positive π and the second one with a phase change of negative π. The linear superposition of these two excitations results in a new cosine amplitude distribution,

$$I_R + I_L = 2\cos \beta \exp [0] \tag{2.46}$$

and, the resulting phase distribution exp[0] produces a broadside beam.

The total far field radiation patterns are represented by the linear superposition of the far field patterns of the two orthogonal beams. This principle of linear superposition applies to both the array excitation and to the far field patterns.

The 64-element array is fed with the 8-element matrix described above. Each matrix feeds a row of 8 microstrip disks and another network feeds each of the 8 rows, figure 2-30. This combination of networks results in a pencil beam radiation pattern where the single 8-element matrix produces a fan beam.

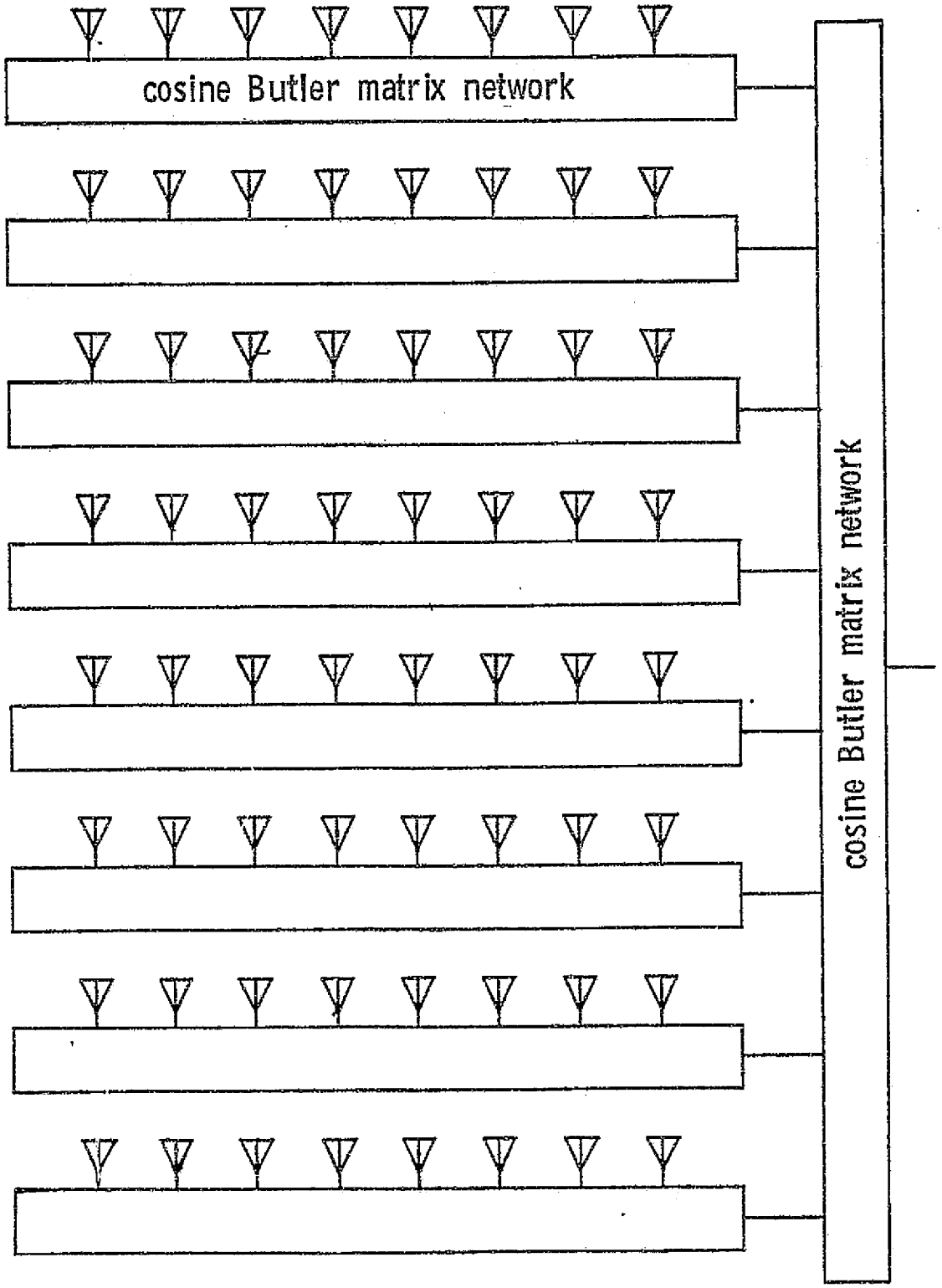

Figure 2-30. The 64 element planar array Butler matrix network.

Stripline.- The feed network can be implemented from many different types of transmission lines: stripline, coax, waveguide, and microstrip. The design for this project utilizes stripline transmission networks. Stripline has the advantage of being compact in size compared with coax and waveguide transmission lines. Stripline circuits were preferred for this application instead of microstrip to avoid radiation from unshielded lines.

Many applications require microstrip feed lines etched on the same laminate as the microstrip radiating elements. Radiation from these microstrip lines may affect the total radiation pattern. For example, Agrawal [31] calculates that a microstrip 3dB branchline coupler radiates 14 percent of the input power. The degradation of the total radiation pattern can often be improved by rerouting the microstrip lines.

The width of the stripline conductor (w) determines the characteristic impedance of the line. The impedance for a given laminate thickness (b) and dielectric constant (ε_r) is expressed by Howe [32],

$$Z_0\sqrt{\varepsilon} = \frac{94.15}{\left[\frac{w/b}{1-t/b} + \frac{c_f}{0.0885\varepsilon_r}\right]} \qquad (2.47)$$

where

$$c_f = \frac{0.0885\varepsilon}{\pi}\left[\frac{2}{1-t/b}\log_e\left[\frac{1}{1-t/b}+1\right]\right] -$$

$$\left[\frac{1}{1-t/b}\right] - 1 \log_e \left[\frac{1}{(1-t/b)^2}\right] - 1 \Bigg] \qquad (2.48)$$

where t is the thickness of the copper conductor. The above equation indicates that changes in the dielectric constant and dimensional tolerances will cause impedance variations. The impedance variations were examined for various stripline widths fabricated from .16 cm thick teflon fiberglass laminates.

Four branchline 3dB hybrid directional couplers are required in the network. The coupler divides the input power from any one port equally between two other ports and supplies zero power to the remaining ports. The operation is performed with phase quadrature between the output signals. Several hybrid couplers were constructed to determine the effects of dimensional tolerances and packaging techniques, figure 2-31. Figure 2-32 shows the amplitude and phase of the transmission through the hybrid coupler.

Figure 2-33 shows the center copper conductor of the stripline Butler matrix feed network. The center conductor consists of hybrid couplers, phase shifters, power divider, and impedance transformers from the circuit in figure 2-29. Figure 2-36 shows the calculated output of the phase shifters and hybrids network which is a function of phase shift for this physical circuit configuration.

Seven stripline three-port power dividers are used in this circuit. These power dividers are simple to fabricate. However, they can not be matched in all three ports simultaneously. Minor

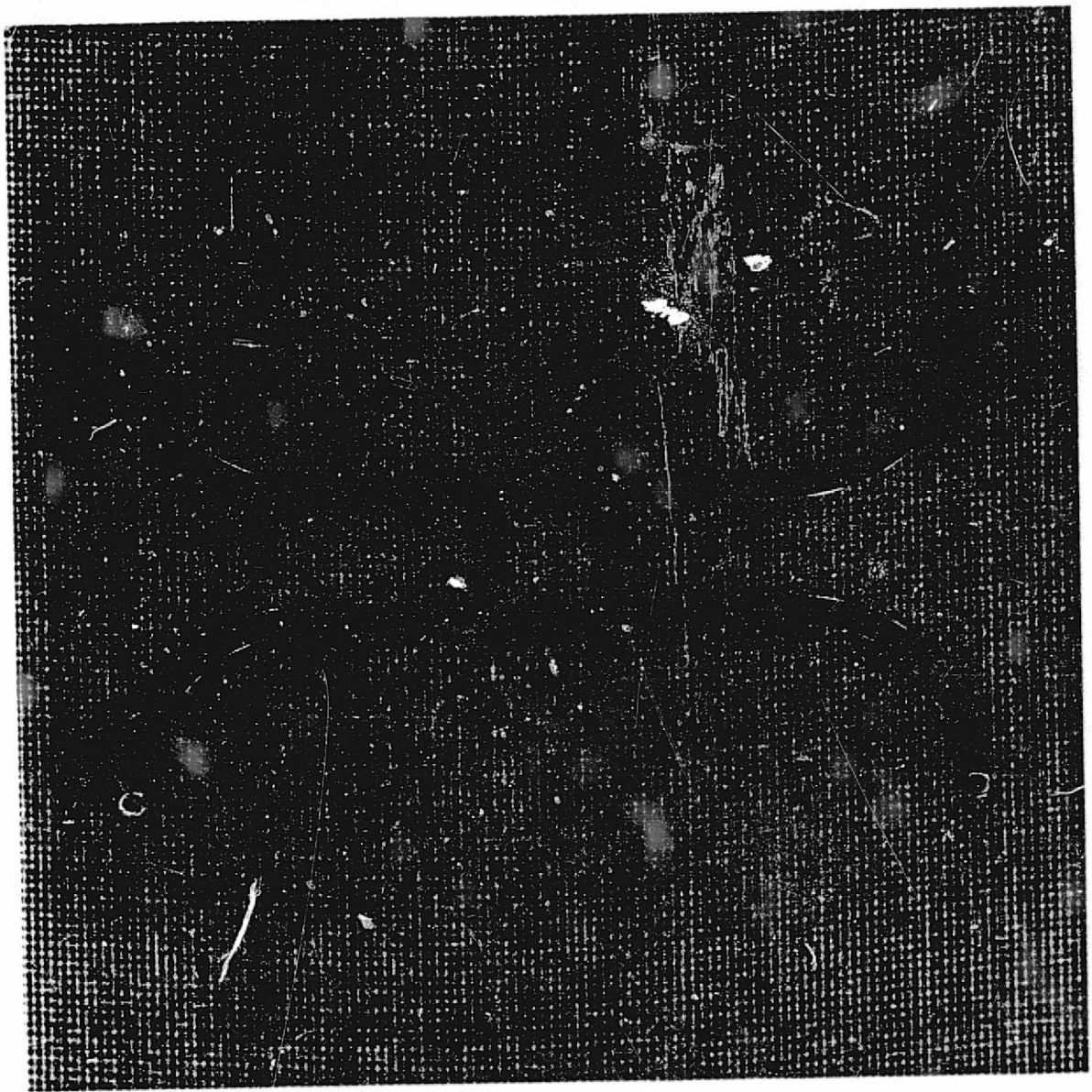

Figure 2-31. The center copper conductor of a stripline 3 dB 90° branchline hybrid coupler.

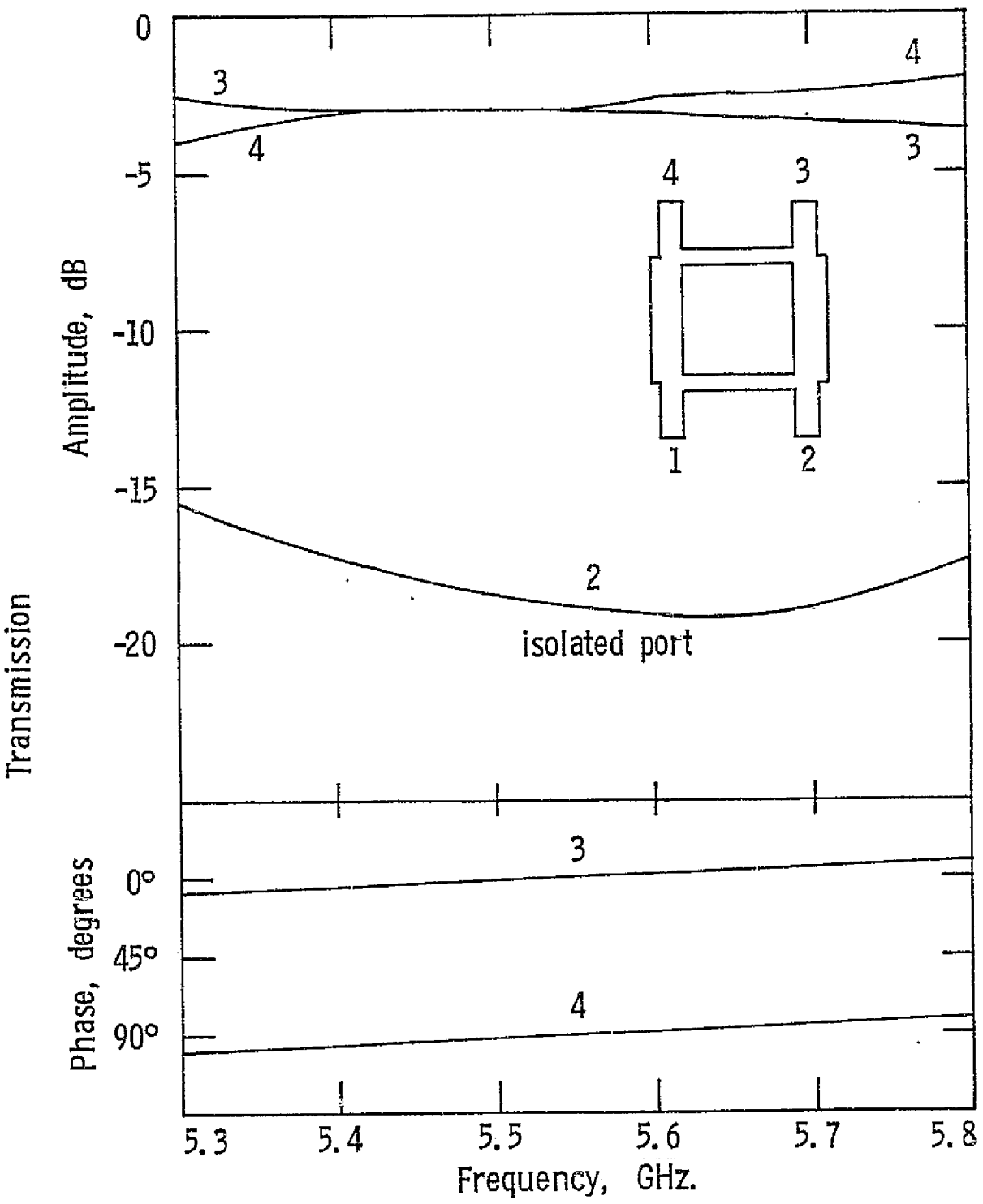

Figure 2-32. Transmission parameters of the branchline hybrid.

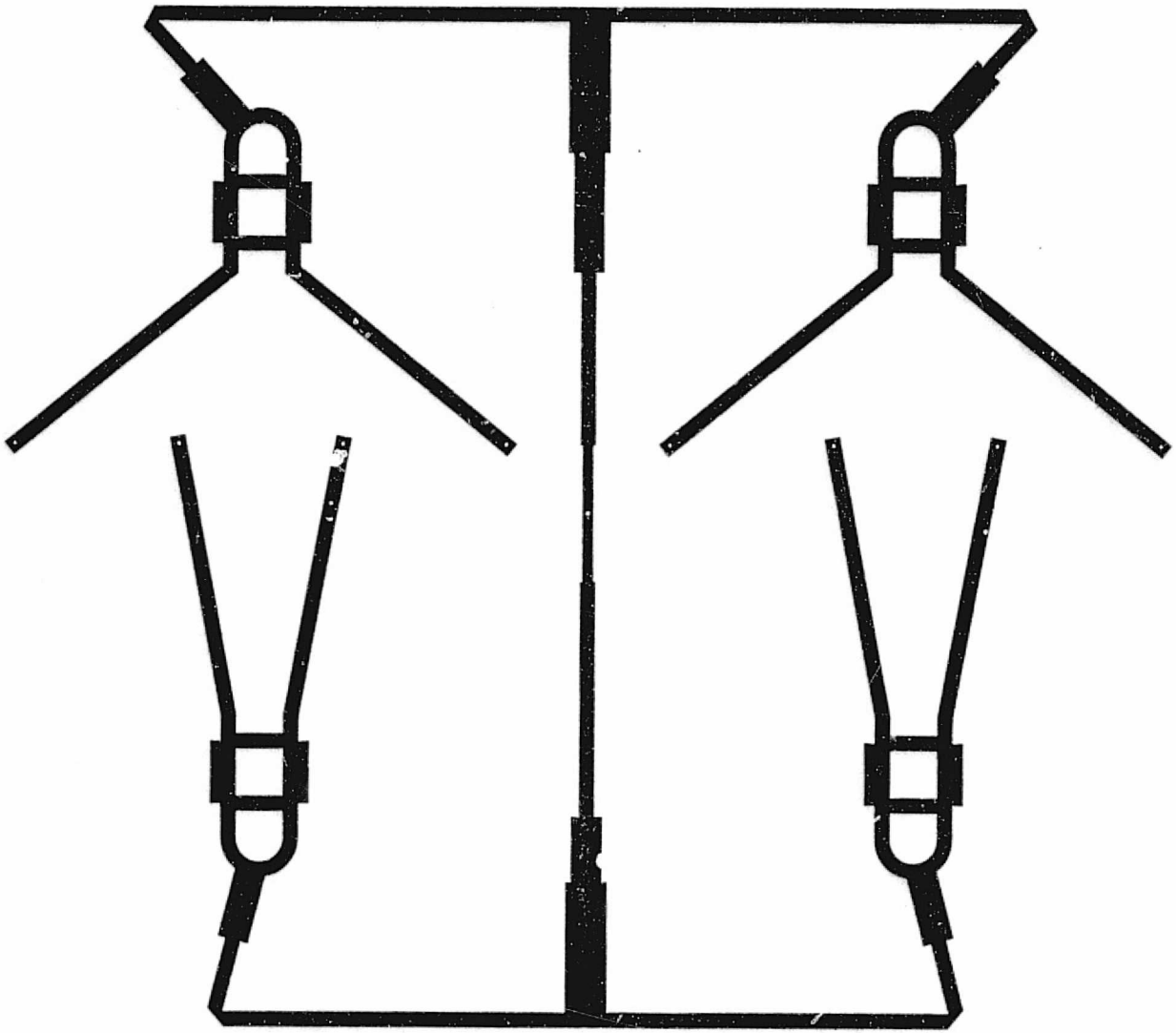

Figure 2-33. The center copper conductor of the stripline Butler matrix

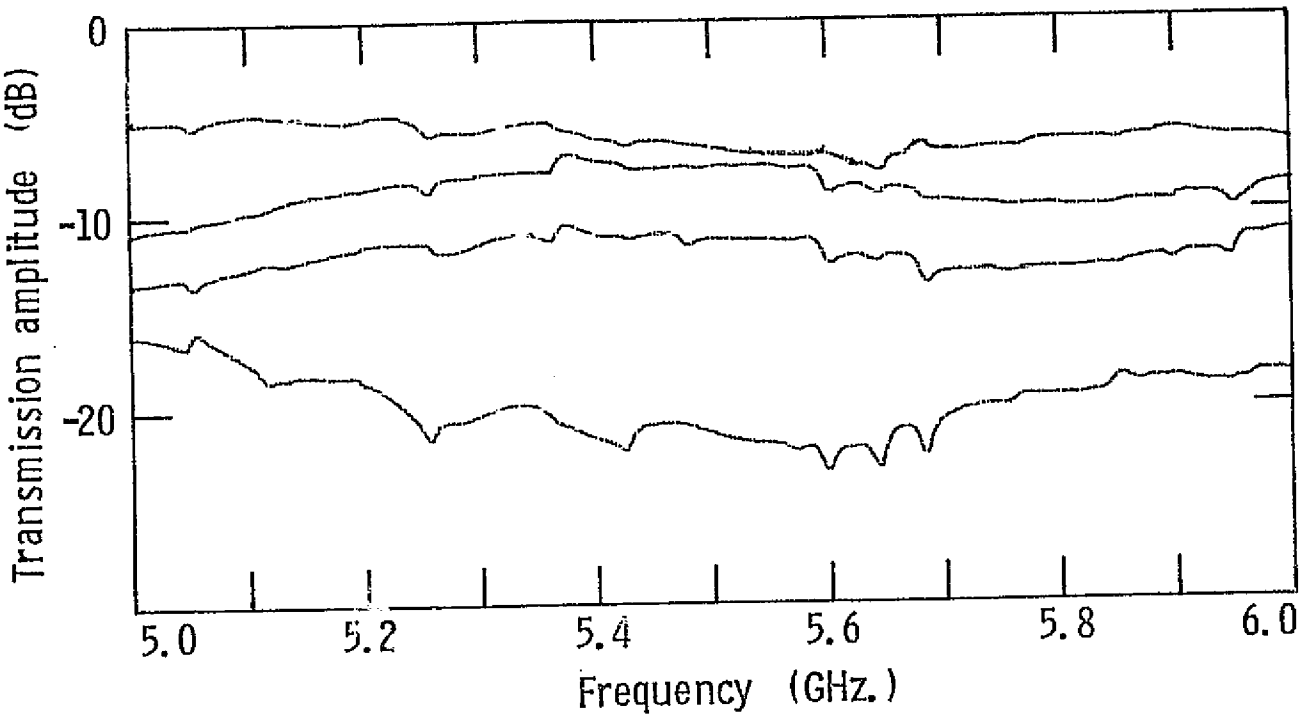

Figure 2-34. Measured transmission amplitude of the stripline Butler matrix.

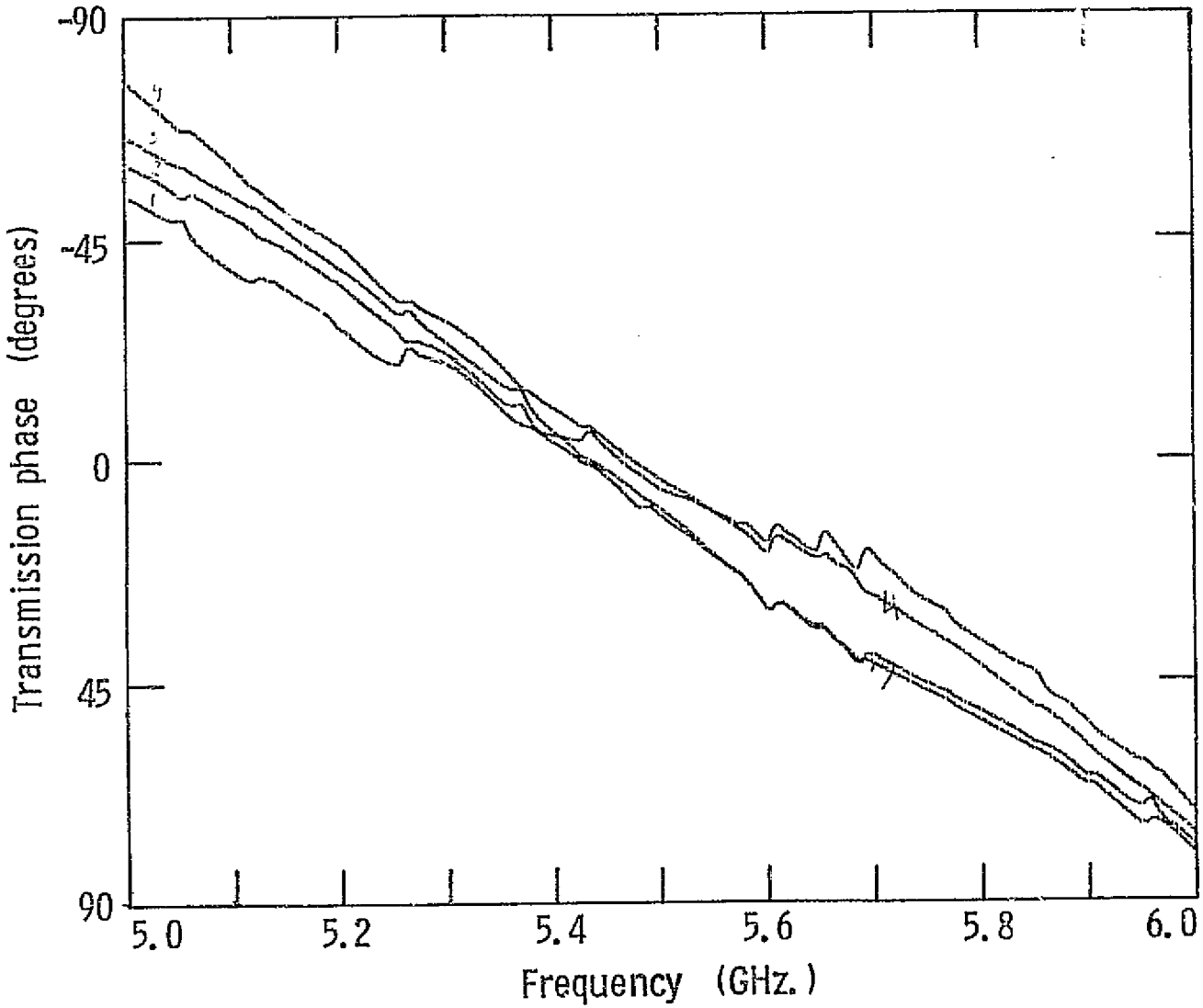

Figure 2-35. Measured transmission phase of the stripline Butler matrix.

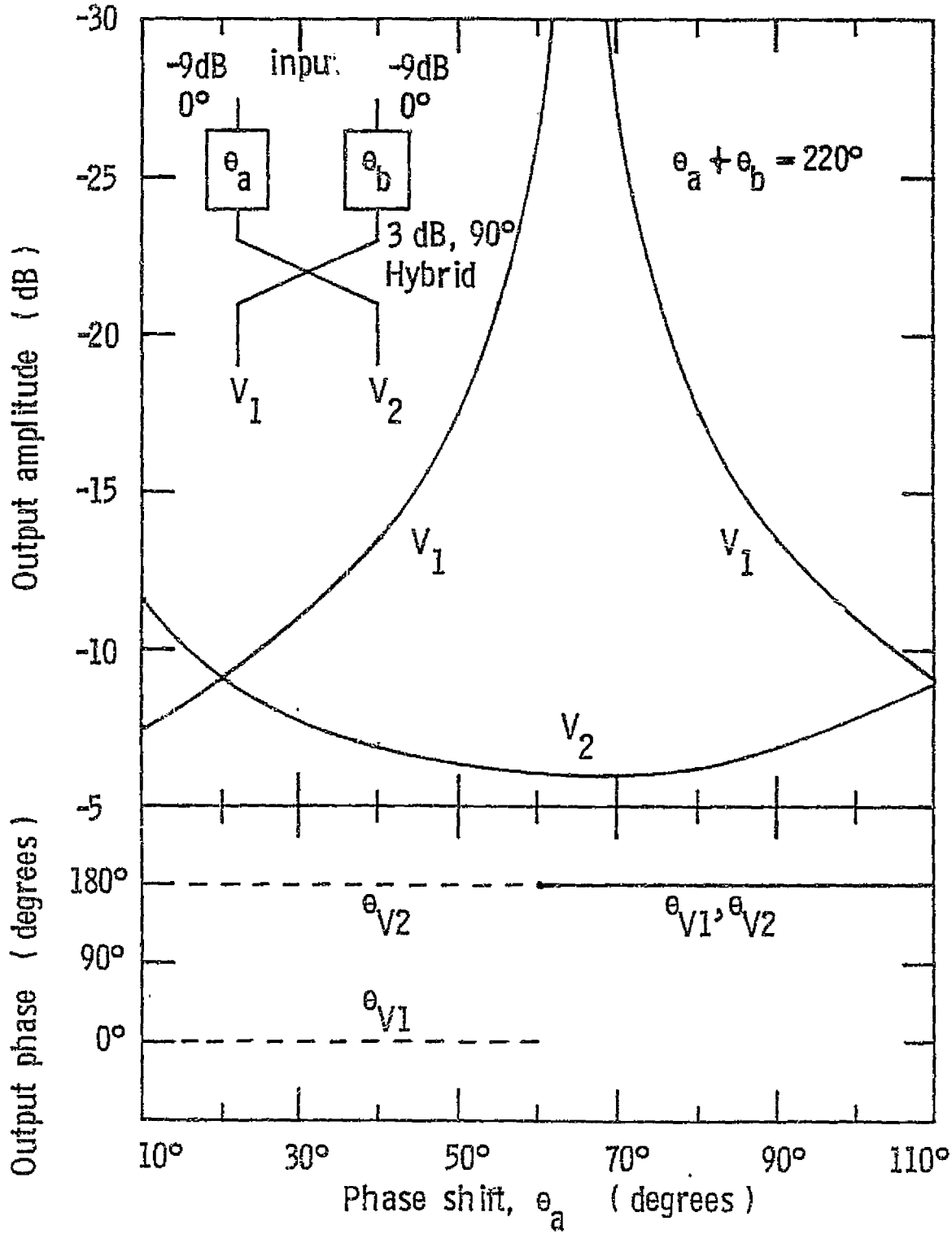

Figure 2-36. Calculated outputs of the hybrid and phase shifter network.

circuit discontinuities and the mis-matched power dividers result in sidelobes which are higher than -23dB.

Four-port power dividers will improve the electrical performance at the expense of greater assembly complexity and cost. The four-port network requires that external resistors or resistive film be added to the stripline package.

Stripline packaging.- The stripline package consists of two copper clad laminates, figure 2-37. The entire assembly is secured with a film fusion bonding process. Therefore, rivets are not necessary to hold the assembly together except as needed for mode suppression and shielding. Mode suppression is required for broadwall launching connections with less than 1/8 wavelength spacing between the rivets. The stripline is self shielding, so many of the rivets installed in the early networks were eliminated, figure 2-38.

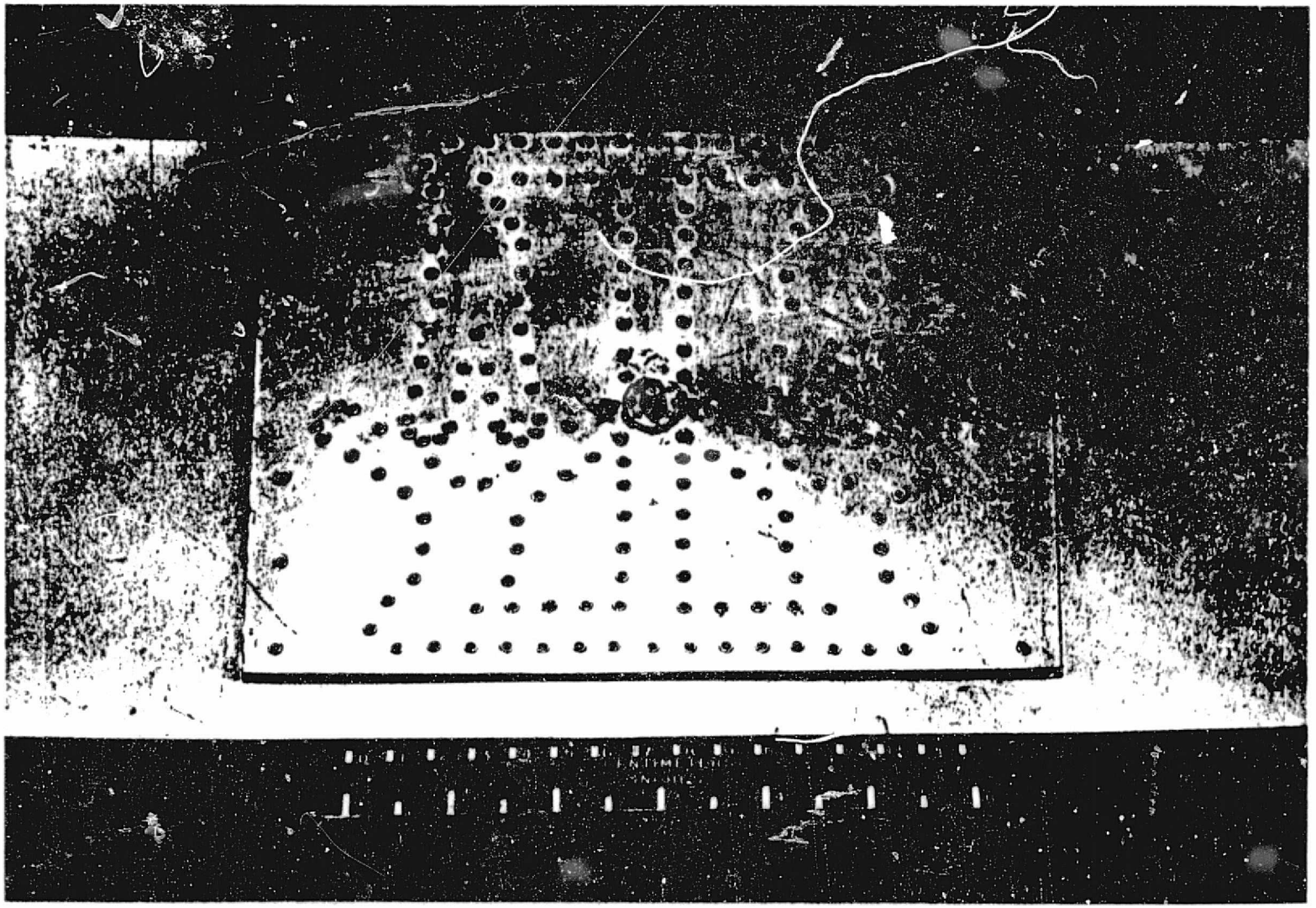

Figure 2-37. The stripline network bonded to the back of the microstrip array.

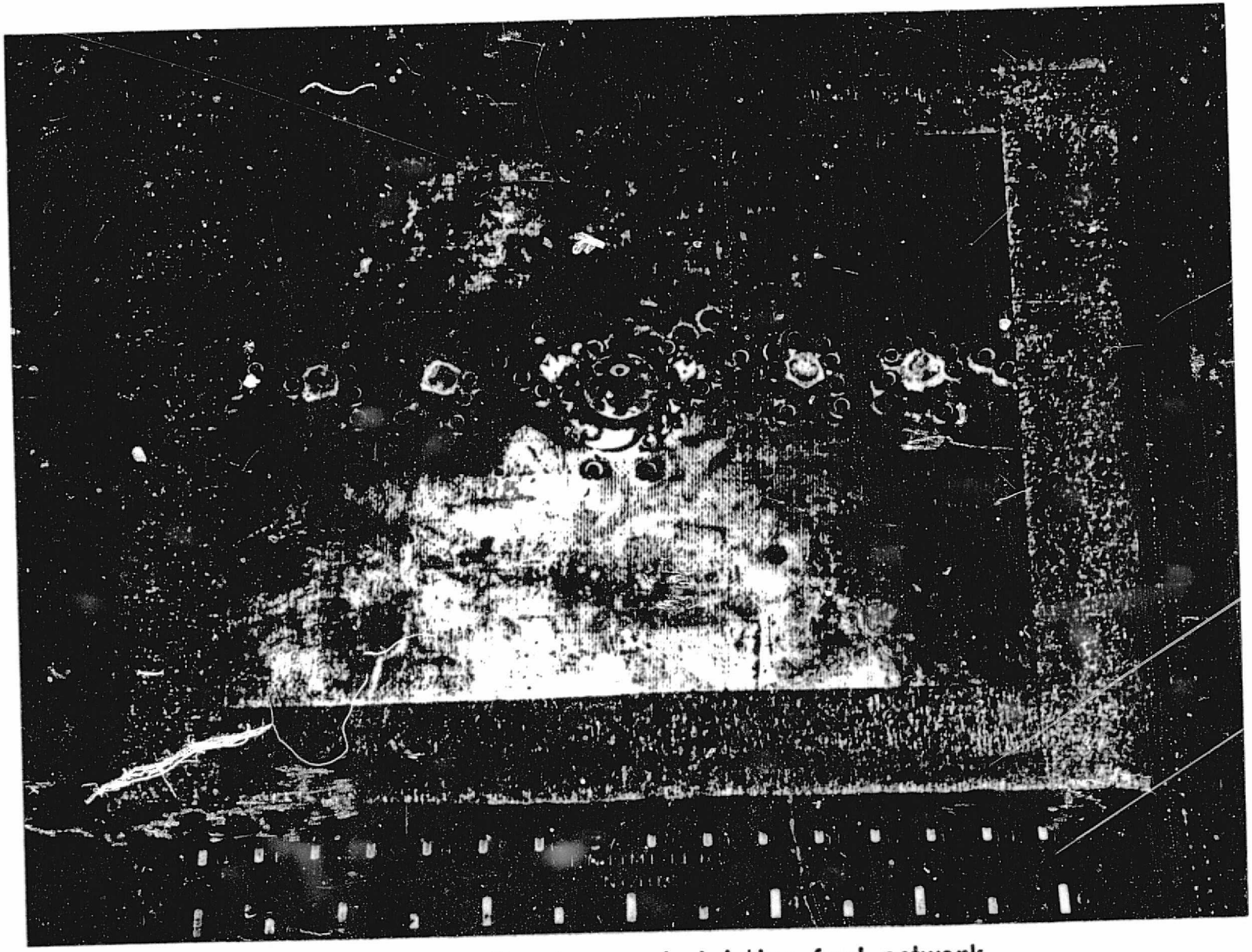

Figure 2-38. The improved stripline feed network.

CHAPTER 3 FABRICATION

Many avionics antenna applications require low profile and conformal antenna arrays. These applications require a high density package with a compact interconnection system.

Microstrip arrays with multilayer printed circuit technology offer an adequate solution for low profile antenna systems. Multilayer laminates provide a method for handling complex interconnection problems. This multilayer package includes the antenna, ground plane, and a shielded transmission line network.

The multilayer printed circuit package consists of a number of multiple layers of thin flexible copper clad laminates. The thin layers are stacked together in an orderly registration. The layers of conductors and the insulator are adjacent to each other. Interconnections are usually obtained by the plated-through-hole process, tubelet, or wire bus system.

Multilayer printed circuit packages retain many of the characteristics of regular printed circuit laminates. For example, large volume production capability, exact reproduction of circuitry from board to board, reduction of wiring time and elimination of miswiring. Its characteristics also include high density of circuitry and terminal points, increased freedom of conductor routing, shorter conductor paths, integral shielding and heat sink planes, and improved environment performance by locating all conductors within a homogeneous dielectric

material. These advantages and also the disadvantages of multilayer printed circuit packages are summarized below [33].

Multilayer Printed-Circuit Boards

Advantages	Disadvantage
1. Weight reduction	1. Poor repairability
2. Cost savings by standardization and simplified production	2. Circuit revision difficult
3. Reliability through:	3. Amplification of shock or vibration inputs
a. simple uniform assembly (reducing errors)	4. Difficult to simulate realistically during breadboard testing
b. connection minimization and control	5. Inspection of final product is difficult
c. controlled assembly process through mechanization	6. High cost in small quantities
4. Uniform electrical impedance and coupling	7. Extended design time
5. Assembly time reduced by simplification	8. Long lead time for fabrication
6. Capable of high inherent reliability (dependent upon process control and type of interconnection)	9. Thermal sensitivity (warp)
7. Can combine structural and electrical functions	

The Laminate

The multilayer printed circuit antenna package consists of radiating elements and feed lines etched from copper clad dielectric laminates. The laminates come in a wide variety of pure materials and mixtures. Laminates are usually in sheet form with copper laminated to one or both sides. A broad selection of thicknesses are available for the basic dielectric material as well as the conducting material. The most common dielectric thickness used for antennas is 0.16 cm (1/16 inch). Other thicknesses from 0.079 cm (1/32 inch) to 0.32 cm (1/8 inch) are also used. There is no universally accepted laminate which is best. Each material has advantages which make it desirable for some specific application and disadvantages which limit its usefulness in other applications.

Dual copper clad teflon fiberglass laminates are used in the project for the antenna substrate and the feed networks. The laminate is constructed from layers of glass cloth which have been impregnated with teflon. The anisotropy due to the woven nature of the glass is not significant for C-band antennas. However, manufacturing repeatability may be a problem with thin lines and coupled transmission lines at higher frequencies.

The dimensional stability of teflon fiberglass is excellent with respect to temperature, humidity, and processing. The teflon has excellent resistance to chemicals, and any standard fabrication process can be used. Also, solder and fluxes have no effect on the teflon fiberglass. However the teflon woven fiberglass laminate has a

tendency to wick water, etching, and plating solutions at the exposed edges. These edges should be protected.

The dual clad teflon fiberglass laminate technical data are summarized below:

Dielectric Constant, 10 GHz: 2.48 $\pm$.04

Dissipation Factor, 10 GHz: .002

Volume Resistivity, Megohm - cm: 10^6

Surface Resistivity, Megohm: 10^4

Arc Resistance - Sec.: 180

Flexual Strength - PSI

Lengthwise: 16,000

Crosswise: 12,000

Tensile Strength - PSI

Lengthwise: 20,000

Crosswise: 16,000

Water Absorption - Percent: .04 (.16 cm)

Copper Peel Strength - lbs/in; 2 oz copper: 12

Coefficient of Thermal Expansion: 1.85 X 10^5C

Fabrication Procedure

The design requirements for antennas require close fabrication tolerances of at least $\pm$.0076 cm (.003 inches). The goal of the fabrication procedures is to meet an overall dimensional tolerance of $\pm$.005 cm (.002 inches). This goal is being realized with a fair degree of consistency [8]. Figure 3-1 outlines the multilayer printed circuit laminate fabrication process.

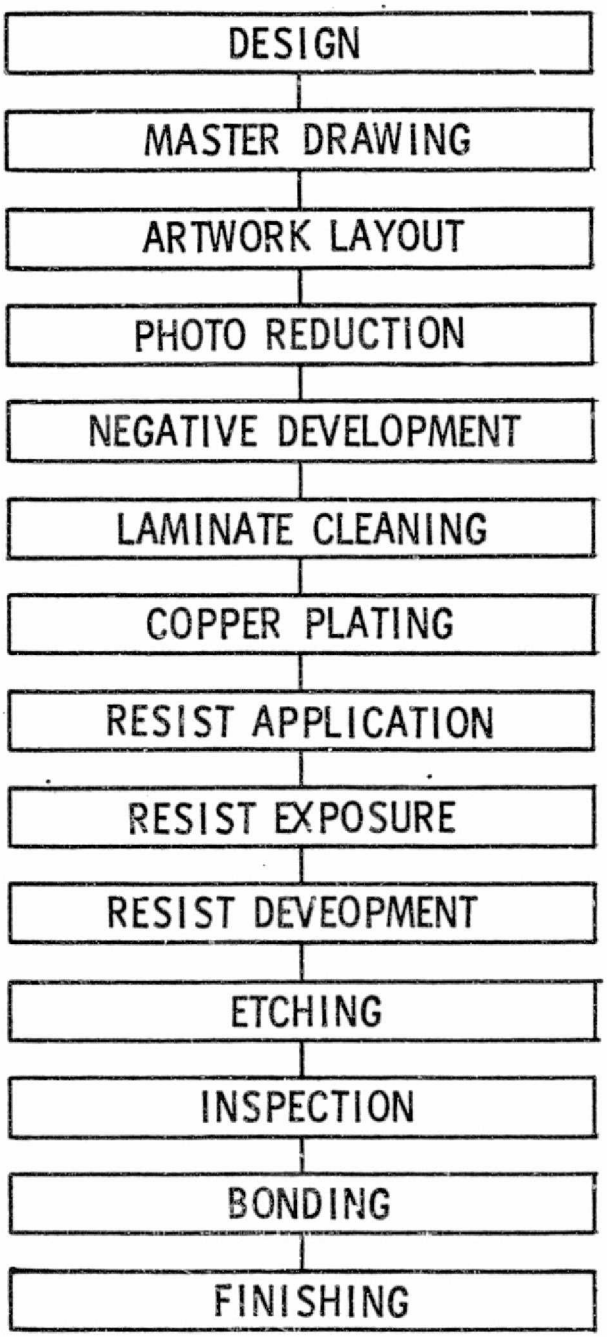

Figure 3-1. The multilayer printed circuit fabrication process.

Artwork layout procedure. - The first step in the fabrication process is the preparation of the artwork from the master drawing developed in the design process. No photo etching process can be better than the artwork from which the photo resist is exposed. Therefore, the artwork is prepared on an enlarged scale for ease of viewing and sharpness of detail on Stabilene film. This film has a .002 cm (.001 inch) thick opaque film layer on a .01 cm (.004 inch) transparent stable film base.

The opaque layer of the Stabilene film is cut to the proper geometry with the precision cutting blade of a manually operated coordinagraph, figure 3-2. The opaque layer then can be peeled away to produce a positive or negative representation of the antenna circuit. The coordinagraph does make cuts with an accuracy of $\pm$.002 cm (.001 inch). Therefore, accumulative geometric error is $\pm$.005 cm (.002 inch).

The completed artwork is next checked on a Cordax measuring instrument using optical scanning to insure that it conforms to the design dimensions with a tolerance $\pm$.005 cm (.002 inch).

Photo reduction. - The cut artwork is then photo reduced with a high precision camera to produce a photographic negative, figure 3-3. This camera is capable of holding reduced dimensions to $\pm$0.0005 cm ($\pm$.0002 inch). Green lights on the camera illuminate the artwork to avoid chromatic aberrations, to insure best lens conditions, and to simplify focusing.

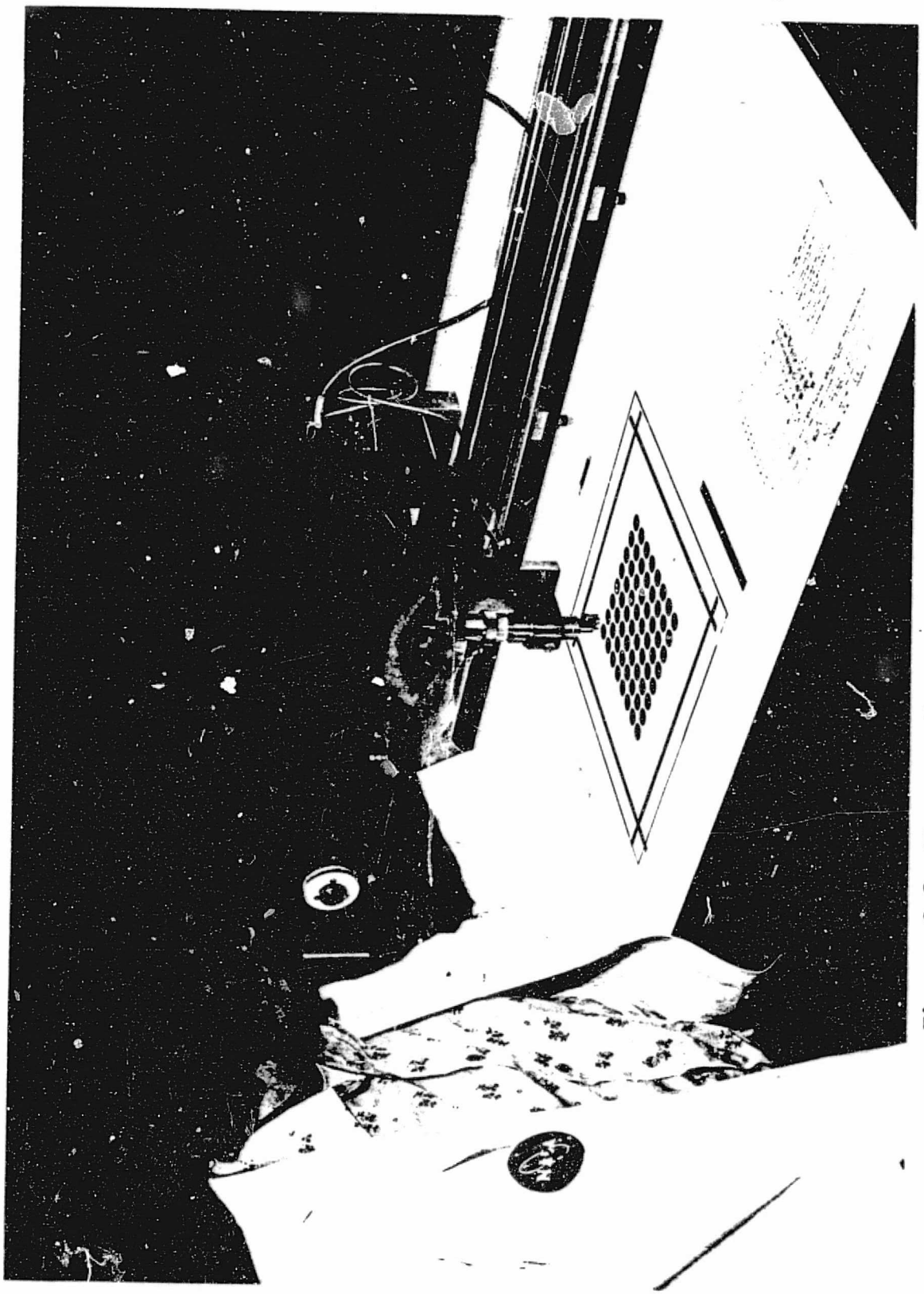

Figure 3-2. The coordinagraph for cutting film artwork.

Figure 3-3. A precision camera photo reduces the artwork.

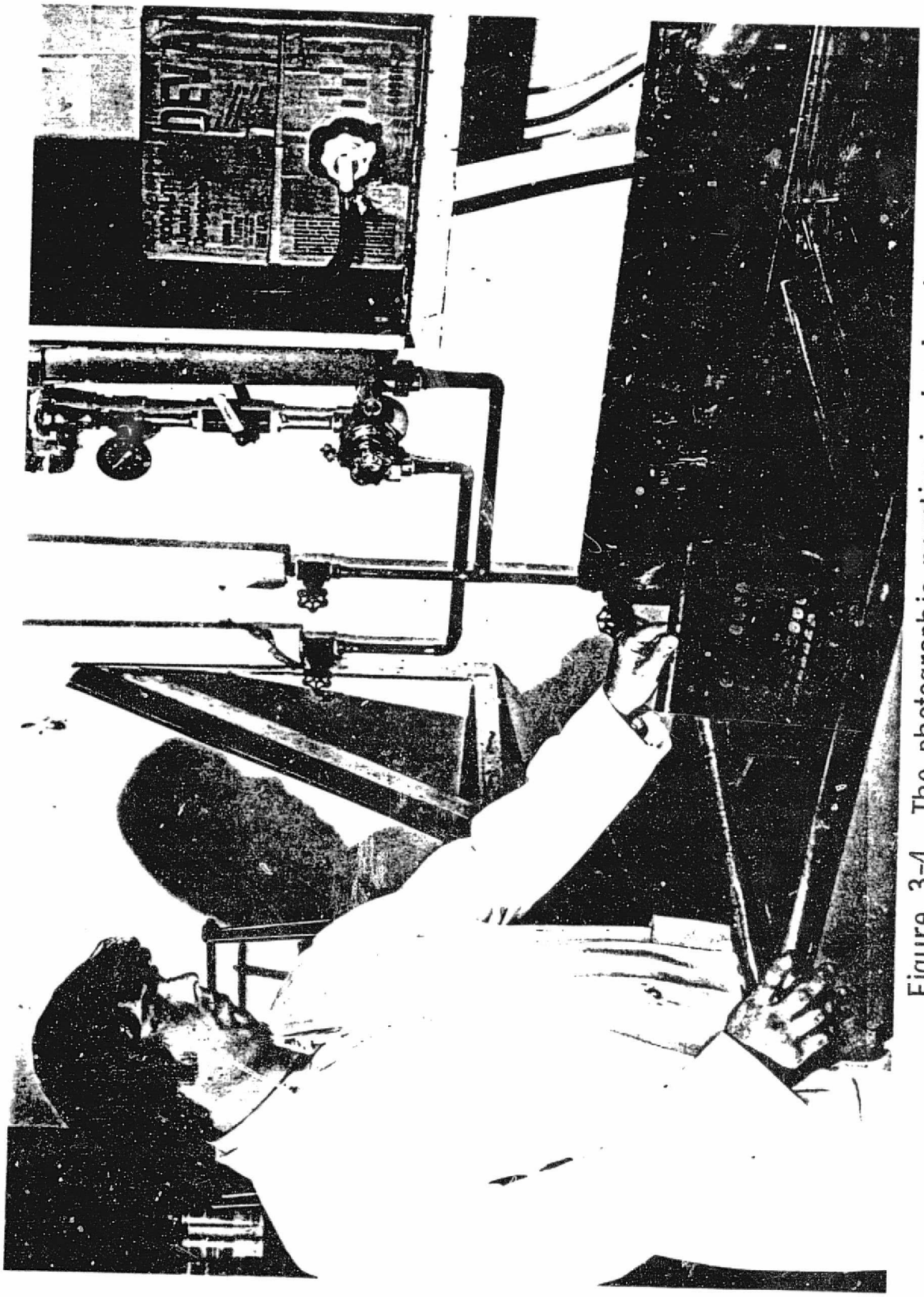

Figure 3-4. The photographic negative is developed.

The camera exposes a fine grained and very high contrast film which is developed to produce a high resolution negative, figure 3-4. This negative is later used to expose the photo resist.

Laminate cleaning. - The surface of the copper clad laminate must be extremely smooth and free of dirt, oils, oxides, and other contaminates. This will insure proper adhesion of the photo resist and the necessary resolution in the photo development step. The scrubber-deburring machine performs this cleaning function in a fast and efficient manner, producing a laminate that has been rinsed and dried, figure 3-6. The laminate is now ready for the photo resist application or copper plating, if required.

Copper plating. - Edge plating and plated-through-holes provide high reliability for side-to-side electrical connections during temperature cycling, mechanical shock, and vibration. A plating fabrication process should obtain these objectives [33]:

1. Complete coverage
2. Even thickness of plate in hole and on surface
3. In hole to surface metal ratio 1:1 to 1:2
4. Fine grain structure
5. No modules or inclusions
6. No excessive build-up at entrance to hole or at outer rim of terminal area
7. No fractures
8. 0.0025 cm (0.001 inch) minimum copper in hole

C-2

The first step in the plating process is to drill the required holes, figure 3-5. Carefully sharpened nonporous carbide drills made for epoxy glass circuit boardsare used. The laminate is next cleaned in the scrubber-deburring machine. Then the teflon holes and sides are chemically etched to roughen the teflon surface. Next, all surfaces are plated with electroless copper which adheres to the teflon, figure 3-7. The electroless copper over the teflon bridges the plated-through-hole with conducting copper cladding on both sides of the board. The conducting copper layer allows more copper to be deposited on the surface by electroplating.

Metallographic cross sectioning is a powerful evaluation method. Selected plated-through-holes are inspected by this method, figure 3-8. This evaluation reveals:

1. Drill-hole quality
2. Laminate continuity
3. Plating thickness, structure, voids, cracks, uniformity, adhesion of copper and resist through the hole
4. Effects of evaluation such as elevated temperature, high relative humidity, and current-carrying tests

The metallographic cross section is prepared by first mounting a plated-through-hole specimen in plastic. After mounting, the laminate is ground down to the area of interest. After grinding, the specimen is polished and etched.

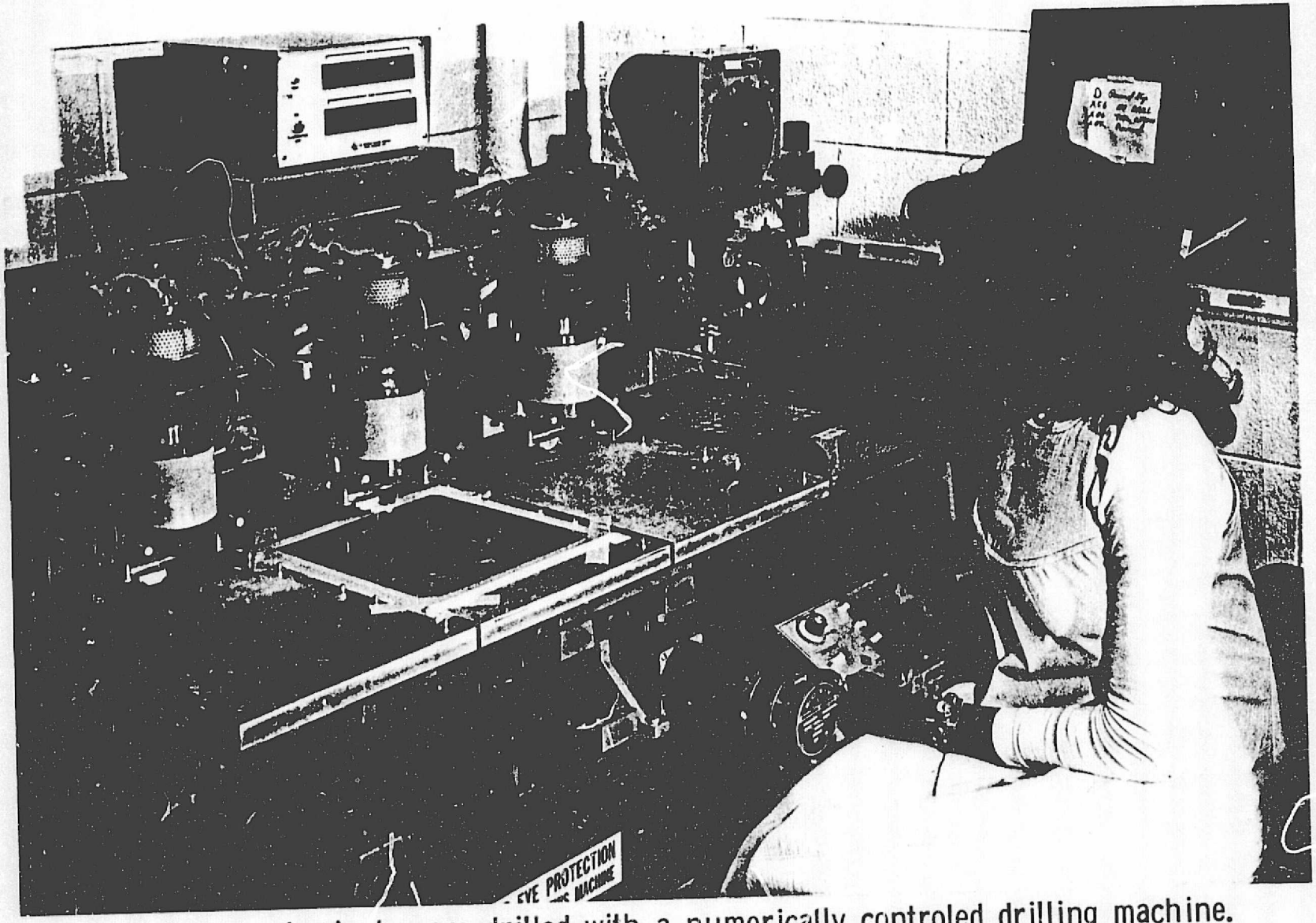

Figure 3-5. The laminates are drilled with a numerically controled drilling machine.

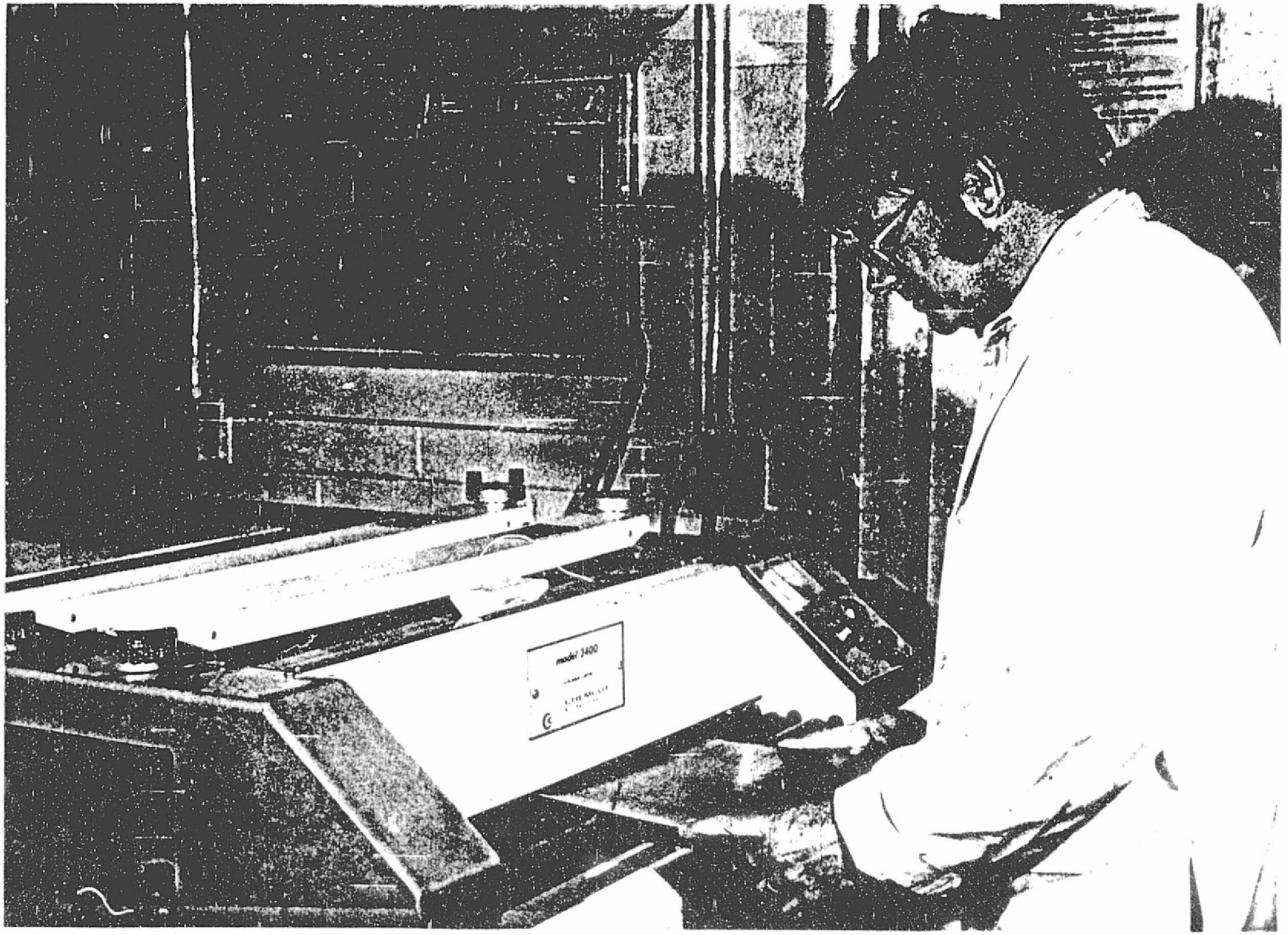

Figure 3-6. The laminates are cleaned with the scrubber-deburring machine.

Figure 3-7. The copper plating tanks.

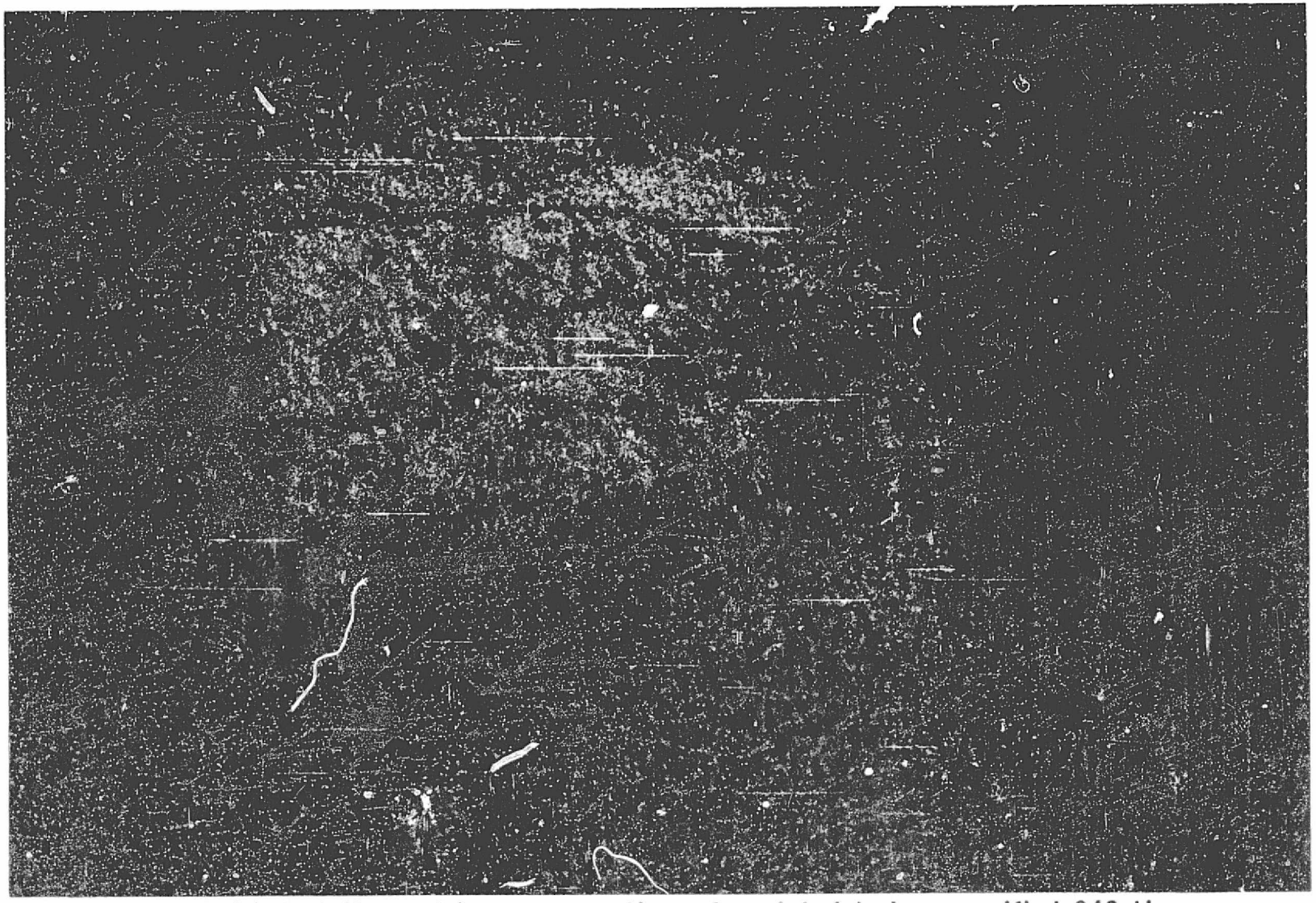

Figure 3-8. Metallographic cross section of a plated hole magnified 940 times.

With this preparation procedure, a metallurgical microscope capable of a 400 magnification ratio is adequate to determine thickness ±30 microinches.

Photo resist application. - Photosensitive resists are capable of fine line definition and well suited for prototype and small production runs of 10 to 15 units.

A dry film photo polymer resist is used for its ability to be applied in continuous lengths and to produce good etching results in either acid or alkaline etch solutions. The resist is applied simultaneously to both sides of the cleaned copper-clad laminate by use of a laminator operating at 115°C ±4° (240°F ±5°). The photopolymer resist is sandwiched between two thin polyethylene cover sheets. The cover sheet nearest the copper-clad laminate is automatically peeled away during resist lamination to allow the resist to adhere to the copper surface. The outer cover sheet is left in place to protect the resist during handling and exposing.

After photo resist application, the laminate is allowed to normalize at room temperature for 15 minutes. Application of the photo resist, and all subsequent steps through development, must be performed in a gold light environment to prevent unwanted exposure by ambient ultraviolet radiation.

Photo resist exposure. - To achieve the necessary fine line resolution in photo resist exposure, the photographic negative is held in contact with the polyethylene cover sheet of the applied photo resist. The required contact is accomplished with a vacuum frame copy

board, figure 3-9. Exposure to the proper wavelength light brings about a polymerization of the exposed photo resist, making it insoluble in the developer solutions. The optimum exposure time varies with the type and thickness of the photo resist and the distance from the light source. The backside of the antenna retains its copper foil, and it is exposed completely without benefit of a mask.

Photo resist development. - The protective polyethylene film is peeled from the resist, and the antenna is developed in a spray developer, figure 3-10, which moves the soluble photo resist material. Developing time is a function of solution temperature, spray distribution and pressure, and the concentration of the dissolved resist in the developing solution.

The spray developer is operated at 26°C (80°F), and the antenna laminate is oscillated slowly to eliminate concentrated developer on any given area. Proper development is insured by visual observation. Since the photo resist is developed in an aqueous solution, the work can proceed directly to the etching process.

Etching. - The etching is performed by a conveyor etcher, figure 3-11, which can handle laminate widths up to 60.96 cm (24 inches) and lengths limited only by the availability of the material. The etching rate, and ultimately the pattern dimensions, depend on etchant temperature, ph level, and conveyor speed. Several test circuits are etched and measured to determine the exact conveyor speed to be used with the prevailing etchant condition. After etching, the remaining photo resist is removed with a standard stripping solution.

Figure 3-9. The photo resist exposure process.

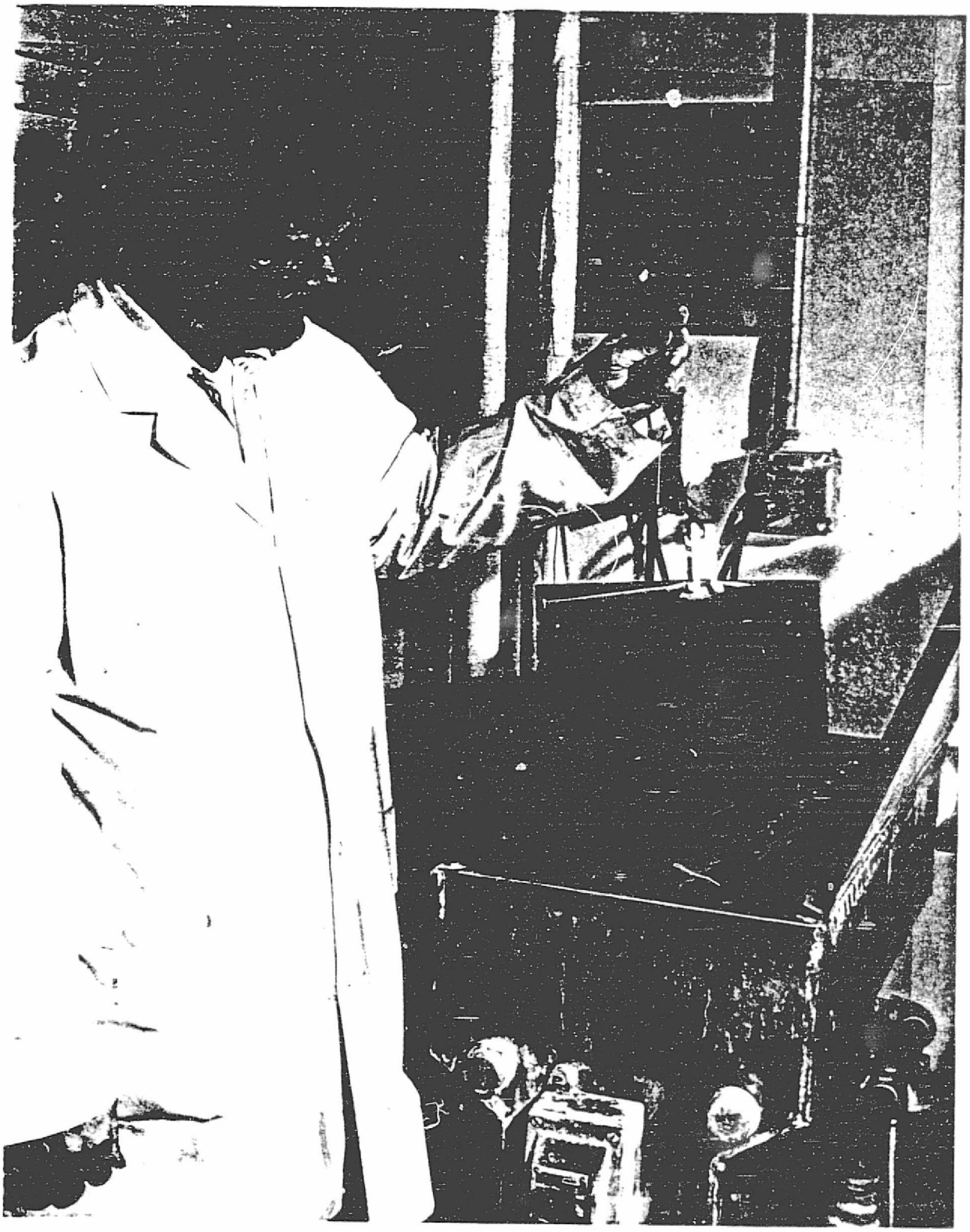

Figure 3-10. The development of the photo resist.

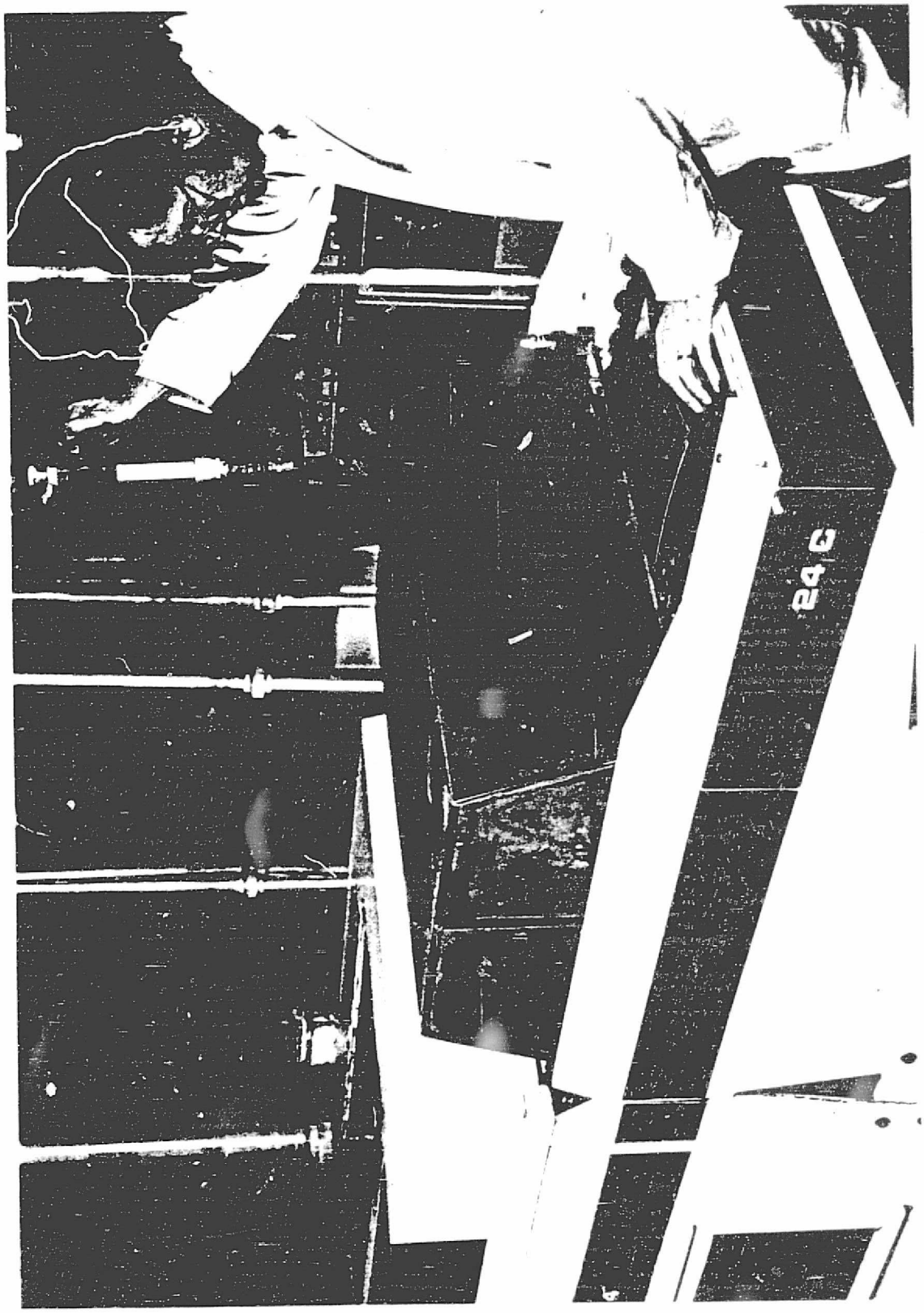

Figure 3-11. The conveyor etching process.

Inspection. - The etched laminate is checked on a Cordax measurement system to verify conformance to dimensional tolerances. All units found to be within dimensional tolerance are inspected for other etching imperfections such as pitting, rounded corners, excessive undercut, etc. The final acceptance or rejection of an individual board must be determined through radiation pattern and impedance testing.

Bonding. - Stripline assemblies and multilayer antenna packages are fusion-bonded with a 6700 fluorocarbon copolymer bonding film. The bonding film is placed between the laminates to be bonded. The temperature at the bondline is monitored with a thermocouple which is also inserted between the laminates. The assembly is then placed between two aluminum tooling plates. The plates, laminates, and bonding film are alined with each other by dowel pins. The assembly is now placed in a hot press preheated to 218°C (425°F), figure 3-12. Asbestos mill board press pads separate the aluminum plates from the press platen to provide more uniform and slower heating.

Then 100 to 200 pounds per square inch pressure is applied to the assembly. The laminates are held in the press until the bondline temperature reaches 204°C (400°F). Then the pressure is held for an additional 15 minutes. The final temperature at the bondline will approach 218°C (425°F), figure 3-13.

The fusion-bonded assembly is cooled under pressure until the temperature is below the melting point of the bonding film. The laminates may now be removed from the press and inspected.

Properly bonded packages will yield a peel bond strength in excess of 3.59 kg/cm (20 lbs/inch). Typical properties of the 6700 fluorocarbon copolymer bonding film are:

Thickness 0.003 cm (.0015 in, matches 1 oz copper)

Specific Gravity 2.1

Water Absorbtion, 24-hour immersion: 0.005 percent

Tensile Strength: (7,00 PSI) 4.92×10^{6} kgs/sq. meter

Elongation: 90 percent

Thermal Conductivity: 5×10^{-4} cgs

Dielectric constant at X-band, 23°C: 2.35

Dissipation factor at X-band, 23°C: 2.5×10^{-3}

Minimum bonding temperature: 199°C (390°F)

Maximum: 246°C (475°F)

Finishing. - The edges are machined to provide a smooth finish. Desired holes and indentations or slots may be milled at this time. Components that were not incorporated during assembly may now be installed.

Heat sensitive components that could not be mounted in the assembly prior to fusion-bonding may be installed by use of the holes drilled before bonding. Such components may be mounted normally and surrounded by a potting compound covered with a foil patch.

Heat stable components may be assembled into the package before fusion-bonding. For example, surface launcher pins are mounted and soldered in place before bonding. Soldered pins may be heated during bonding to sufficient temperature to reflow the solder and an electrically sound solder bond will be maintained.

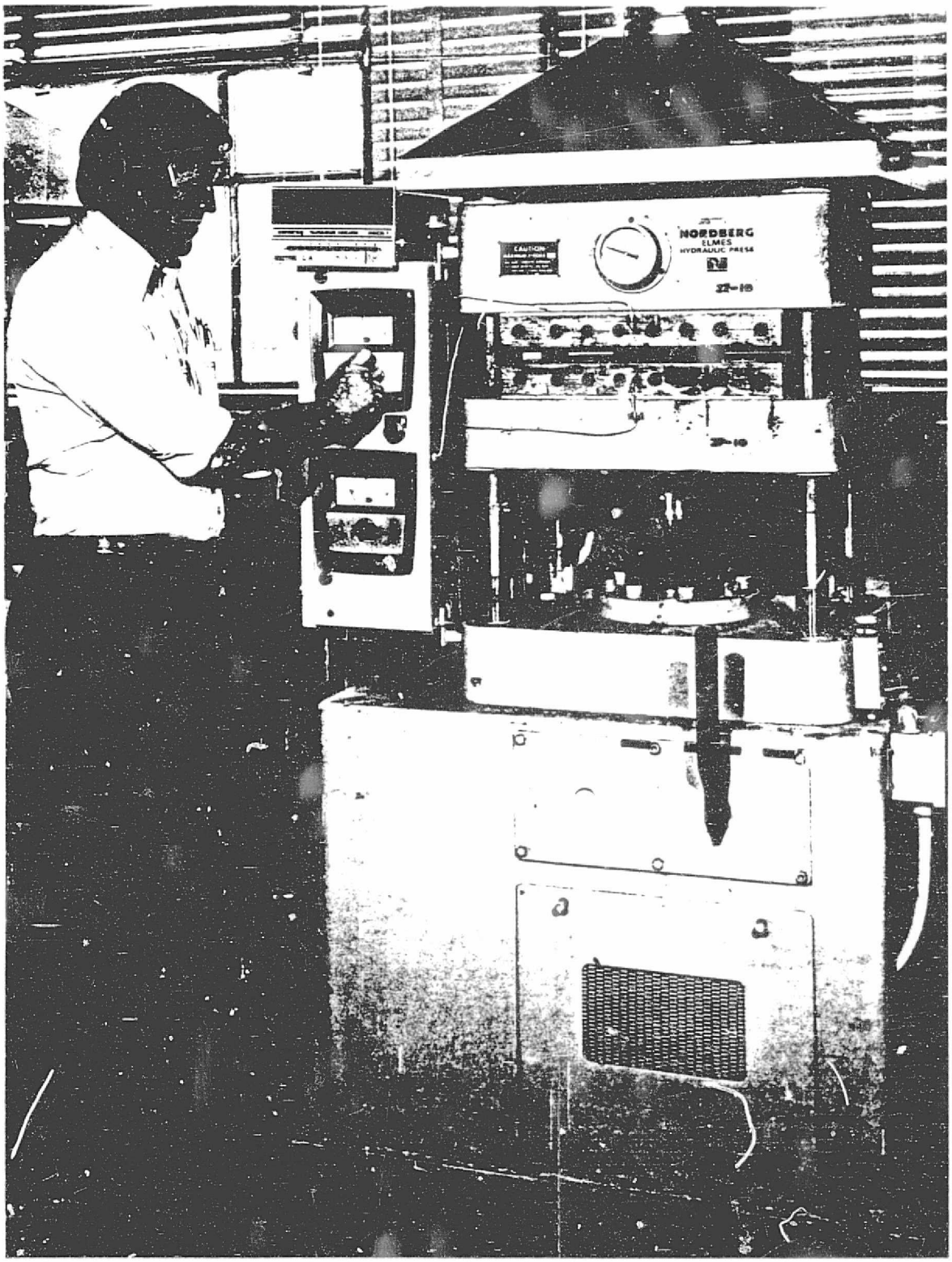

Figure 3-12. The bonding of stripline packages in a hot press.

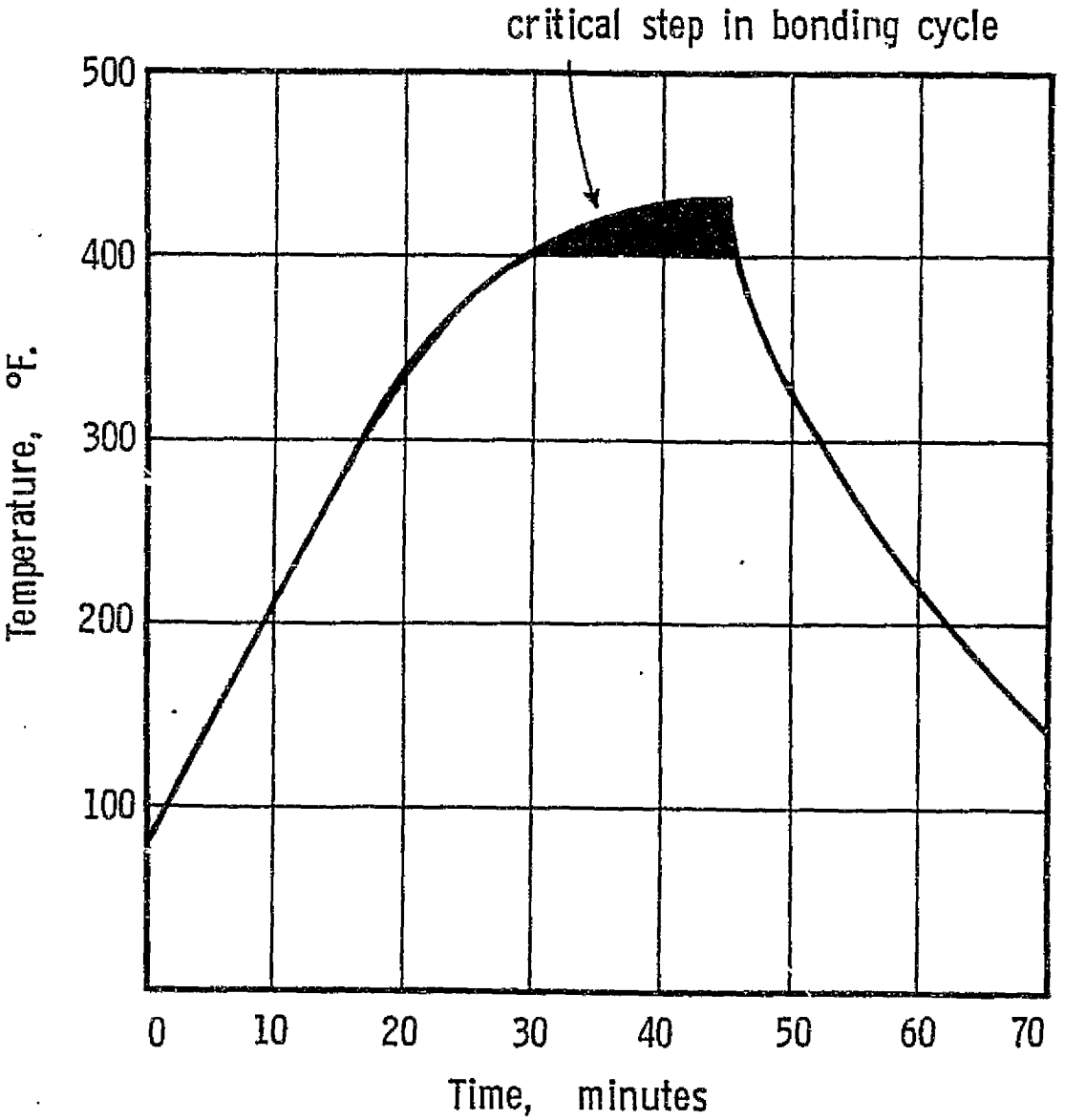

Figure 3-13. Laminate temperature measured by a thermocouple at the bondline during the bonding process.

CHAPTER 4 SYSTEM PERFORMANCE

This chapter compares the measured system performance of the microstrip disk and the low sidelobe linear and planar microstrip arrays. Three experimental C-band systems were considered:

1. The circular disk microstrip antenna
2. The 8-element linear microstrip array with a Butler matrix feed network
3. The 64-element planar array with a Butler matrix feed network.

The radiation characteristics and the impedance properties of each system were measured. The performance of each antenna is summarized in figure 4-1.

Radiation Performance

The three-dimensional far-field radiation pattern is one of the most important performance characteristics of the antennas tested. Therefore, the complete description of the field requires intensity measurements over the entire sphere of polar coordinate aspect angles, 4π steradians. The antenna is located in the YZ plane with the main beam radiating in the negative X direction, figure 4-2.

Each test antenna was measured in an indoor anechoic test range. Figure 4-3 shows the 64-element array mounted on a pedestal in the NASA Langley Research Center antenna test facility. The pedestal rotated the antenna around the Y and Z axes so the field was measured in all directions. The antenna rotation is controlled from the chamber console (figure 4-4), and then the data are recorded on magnetic tape.

		Microstrip Disk	8-Element Linear Array	64-Element Planar Array
I Radiation:				
3 dB beamwidth:	E-plane	110^{o}	20^{o}	19^{o}
	H-plane	85^{o}	83^{o}	20^{o}
First Sidelobe level:	E-plane	-	-20.5 dB	-22.5 dB
	H-plane	-	-	-20.0 dB
Frequency = 5.5 GHz				
Directivity		7.8 dB	13.5 dB	20.2 dB
Maximum gain		6.9 +5 dB	12.8 +.5 dB	18.6 +.5 dB
Efficiency		81 +10%	85 +10%	69 +8%
Frequency		5.7 GHz	5.5 GHz	5.5 GHz
3 dB gain bandwidth		7.6%	12.0%	12.2%
II Impedance				
Zo = 50 ohms				
Center frequency = 5.5 GHz				
2:1 VSWR bandwidth		2%	7%	1%
3:1 VSWR bandwidth		5%	8%	2%

Figure 4-1.- Summary of performance

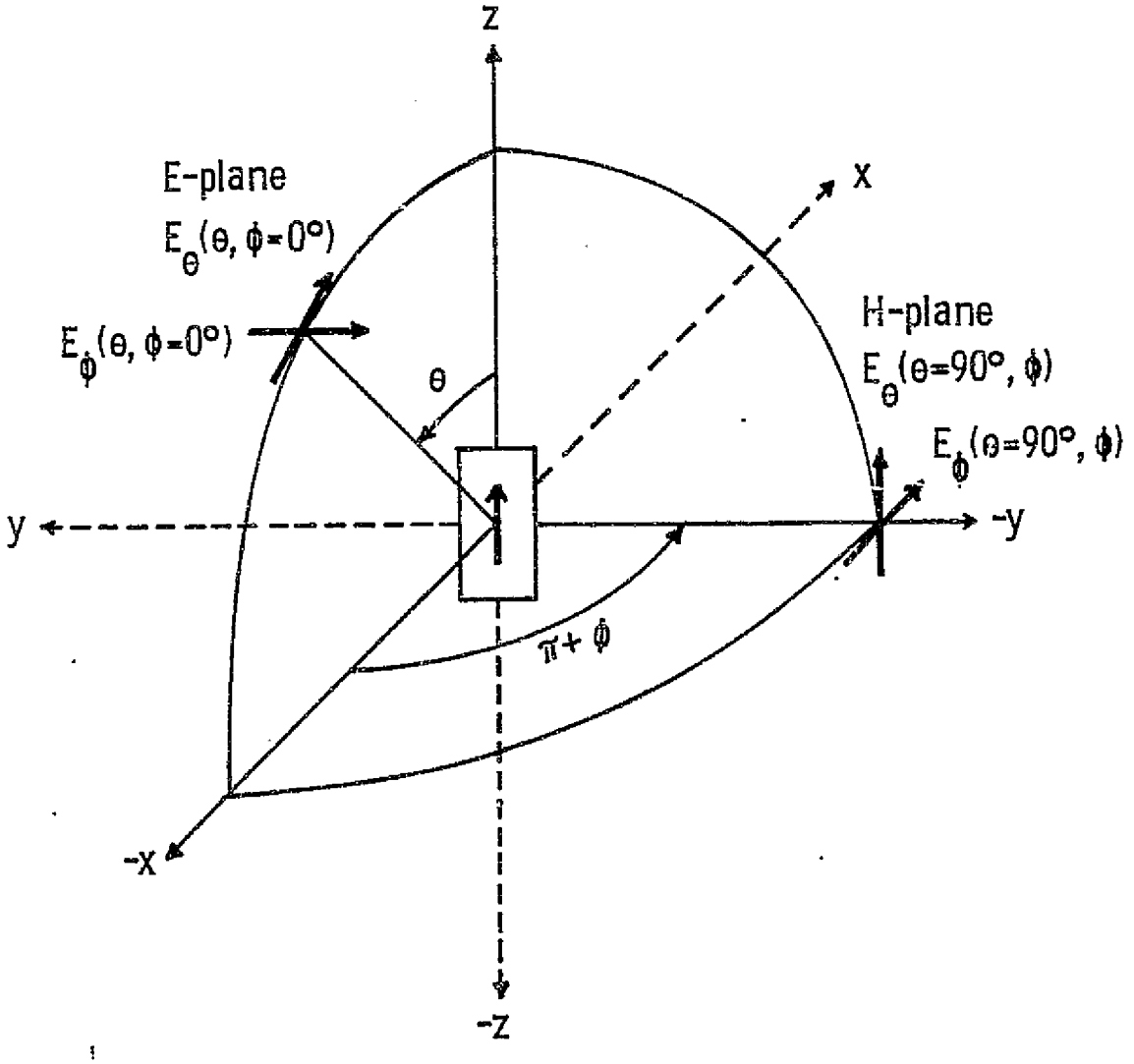

The coordinate system for the measurement of radiation patterns.

Figure 4-2.

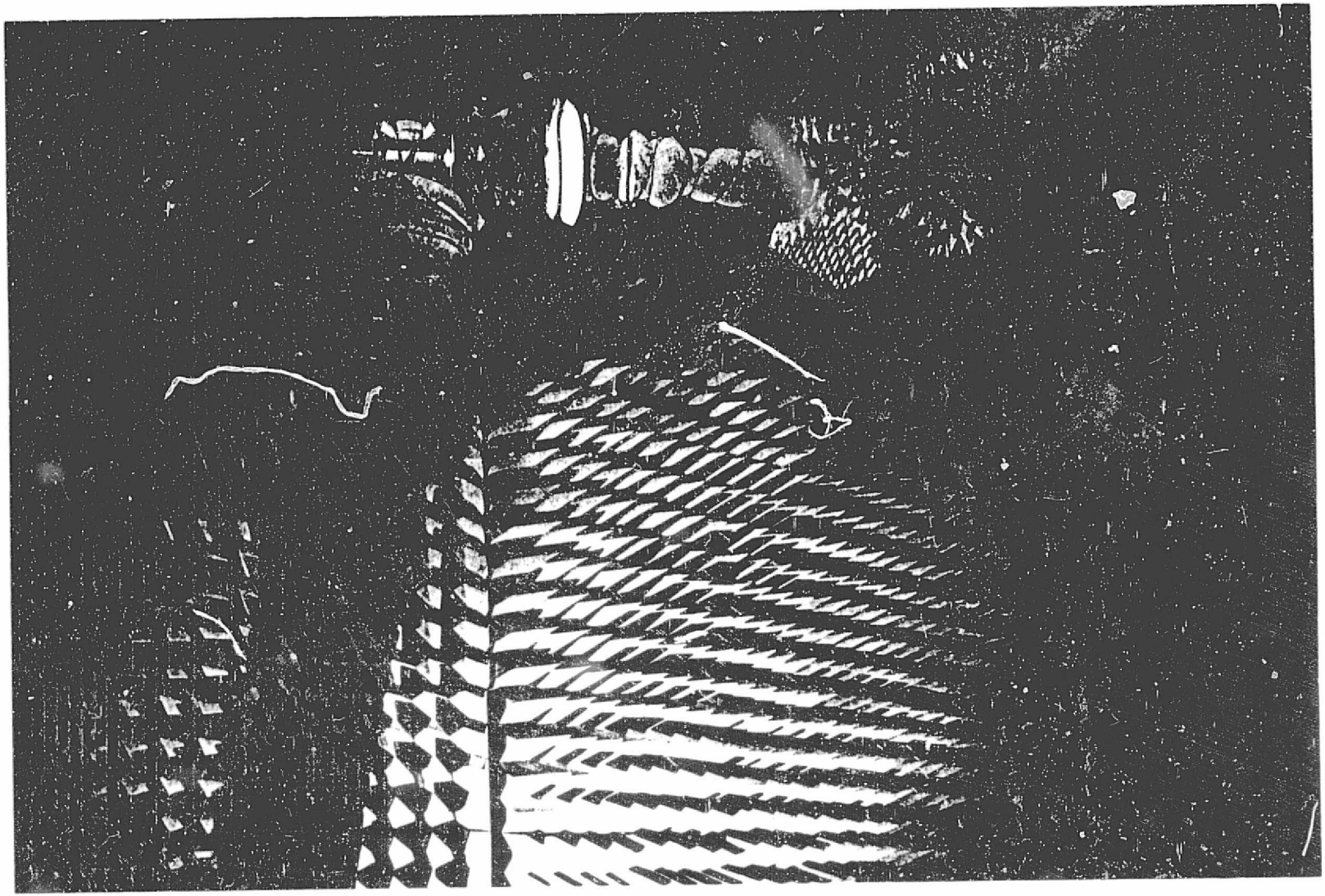

Figure 4-3. The 64 element array mounted in the anechoic test chamber.

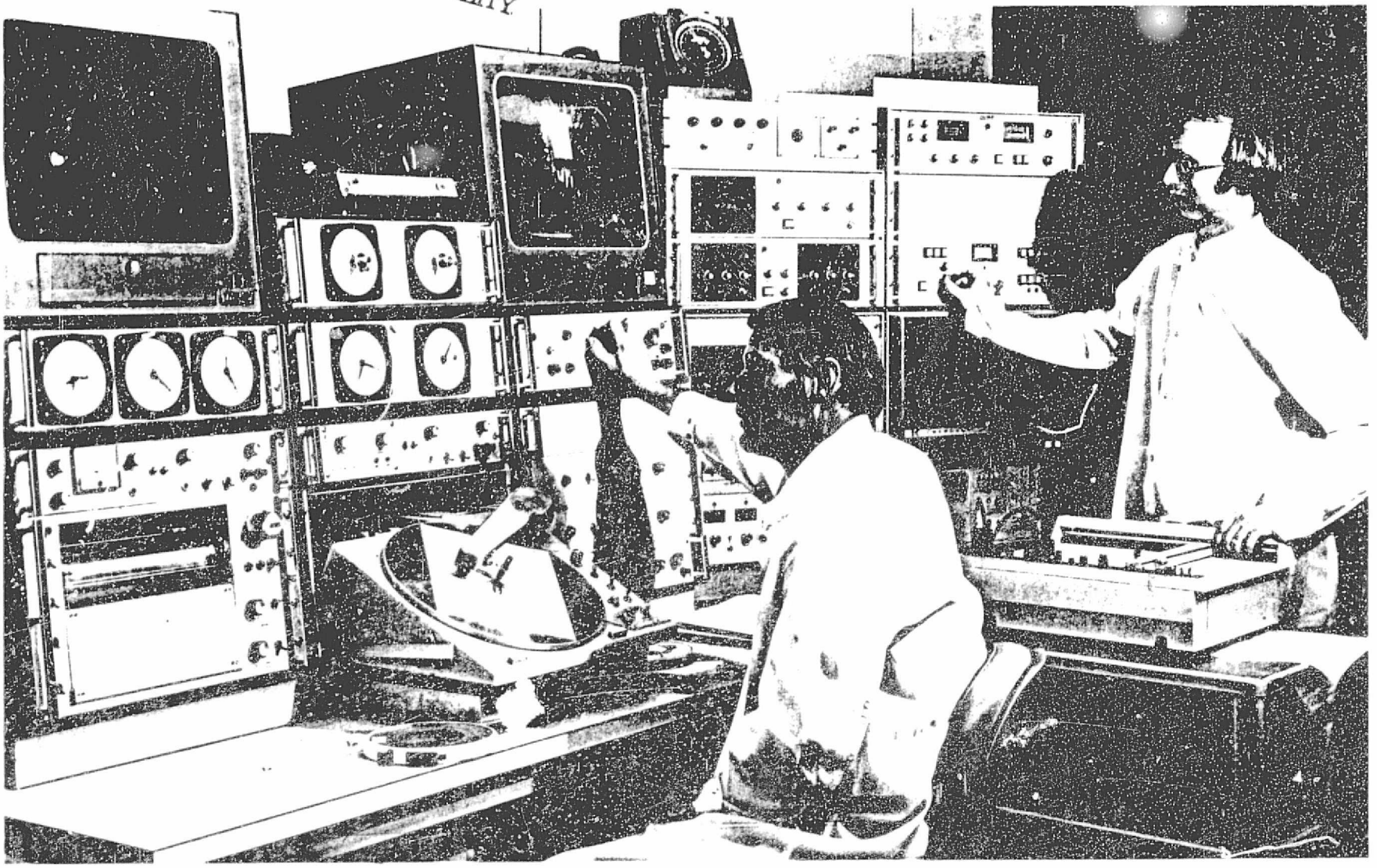

Figure 4-4. The anechoic chamber operating console.

A circularly polarized high gain horn should illuminate the test antenna with a plane wave. Plane wavefronts are obtained only at infinite distances so limits must be specified. A commonly specified criterion is the phase difference between the center and the edge of the antenna under test shall be no greater than 10^{0} [19]. The distance R between the transmitting antenna and the antenna under test is 23 meters. The phase error δ between the center and the end of the array is then

$$\delta^{0} = \frac{d^{2}}{8R} \frac{360^{0}}{\lambda} = 0.9^{0},$$

where d = length of the array, 0.158 meters,

λ = wavelength, 0.0545 meters

R = distance between antennas, 23 meters

The minimum distance R between the transmitting and receiving antenna under test for a 10^{0} phase difference is

$$R \geq 4.5 \frac{d^{2}}{\lambda} = 2.07 \text{ meters}$$

The antenna patterns are recorded in 2^{0} increments in both theta and phi. Theta is increased in 2^{0} increments from 0 to 180^{0} as phi increases continuously from 0 to 360^{0}. A complete recording consists of 91 scans with a total of 16,380 data points. Since the transmitting antenna is circularly polarized this represents the total spherical radiation. The radiation pattern data are integrated over 4π steradians to determine the antenna's directivity.

The directivity is calculated at the peak of the main beam. To find the peak the computer scans the recorded data. The maximum directivity increases with frequency as shown in figure 4-20 for each test antenna.

The radiation patterns are plotted relative to the maximum directivity value at a given frequency. The recorded radiation pattern is then displayed as a volumetric false color plot in which the directivity values that fall within specified ranges are assigned a color. The computer generated false color plots are displayed on a television screen and then photographed to provide a single volumetric pattern.

The volumetric patterns are presented in three forms. The first presentation, figures 4-5, 4-6, 4-7, are false color plots which display the directivity values relative to an isotropic radiator that fall within seven ranges: $\geq$0 dBi, $\geq$-3 dBi, $\geq$-6 dBi, $\geq$10 dBi, $\geq$-15 dBi, $\geq$-20 dBi, and $\leq$-20 dBi. The second presentation, figures 4-8, 4-9, 4-10, displays the directivity levels in shades of gray instead of color. Figures 4-11, 4-12, and 4-13 are volumetric plots which display the directivity values relative to the peak of the main beam instead of relative to isotropic directivity. The normalized directivity levels relative to the beam peak are 0 to -3 dB, -3 to -6 dB, -6 to -10 dB, -10 to -15 dB, -15 to -20 dB, -20 to -25 dB, and <-25 dB. the lightest shade of grey represents the half power beamwidth.

Comprehensive pattern surveys are often necessary; however, for many applications it is possible to obtain sufficient information with

only a few radiation patterns. Four patterns which bisect the major lobe of radiation in two perpendicular planes are required when the antenna is in the Y-Z plane and the electric field is along the Z axis, figure 4-2.

The first pattern, the E-plane pattern, is designated $E_\theta(\theta, \phi = 0^o)$. The theta component of the electric field is measured in the X-Z plane as a function of theta. The second principal pattern, the H-plane pattern, is designated

$$E_\theta \ (\theta = 90^o, \phi)$$

The theta component of the electric field is measured as a function of phi in the X-Y plane.

The dominant radiation from linearly polarized microstrip antennas is in the E-plane and H-plane patterns; but, some of the minor lobes may be cross-polarized. To observe such cross-polarization in the X-Z and X-Y plane requires the measurement of the $E_\phi \ (\theta, \phi = 0^o)$ and $E_\phi \ (\theta = 90^o, \phi)$ patterns.

Measured E and H-plane patterns with the cross-polarized components are plotted in figures 4-14, 4-15, and 4-16 for the single microstrip disk, the 8-element linear array, and the 64-element rectangular array.

The radiation patterns of each array vary with frequency. The E-plane patterns of the 8-element linear array are displayed as a function of frequency from 5.0 GHz to 6.0 GHz in figure 4-17. In addition, the E-plane and H-plane patterns of the 64-element planar array are displayed for 12 frequencies from 5.0 to 6.1 GHz in figure 4-18.

The first sidelobe level versus frequency from the above patterns is shown in figure 4-19 from 5.0 to 6.0 GHz. The sidelobe level varies from -20 to -23.5 dB in the frequency range of 5.3 to 5.8 GHz. The level varies principally due to errors in the amplitude and phase of the excitation from the stripline feednetwork. These problems are discussed in chapter 2.

The gain of each antenna system was measured with a swept frequency receiver relative to the gain of a standard horn. The gain and directivity are compared in figure 4-20 from 5.0 to 6.0 GHz. The efficiency of the system η can be determined from the ratio of the gain and directivity at the peak of the main lobe (θ, ϕ):

$$\eta = G(\theta, \phi) / D(\theta, \phi)$$

The maximum efficiencies for each antenna are summarized in figure 4-1.

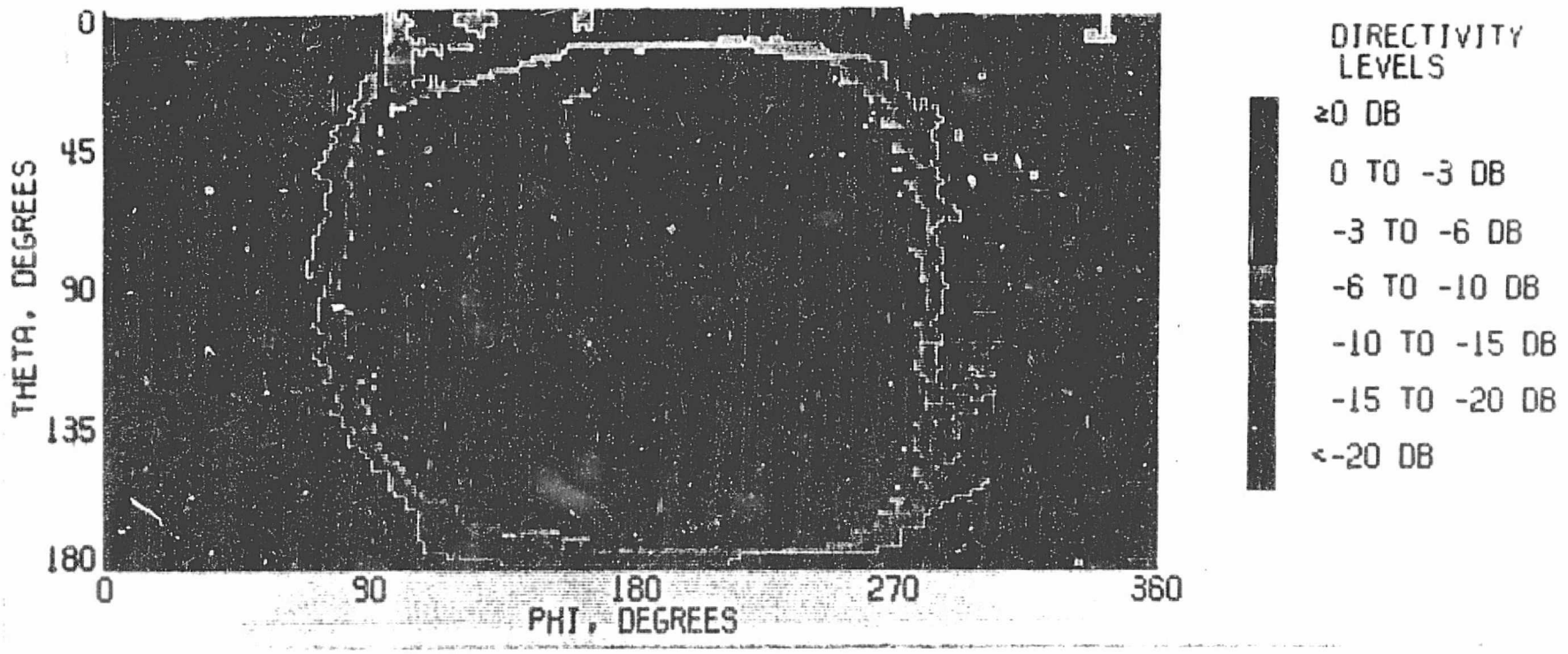

Figure 4-5. Measured color volumetric pattern of a microstrip disk relative to isotropic directivity.

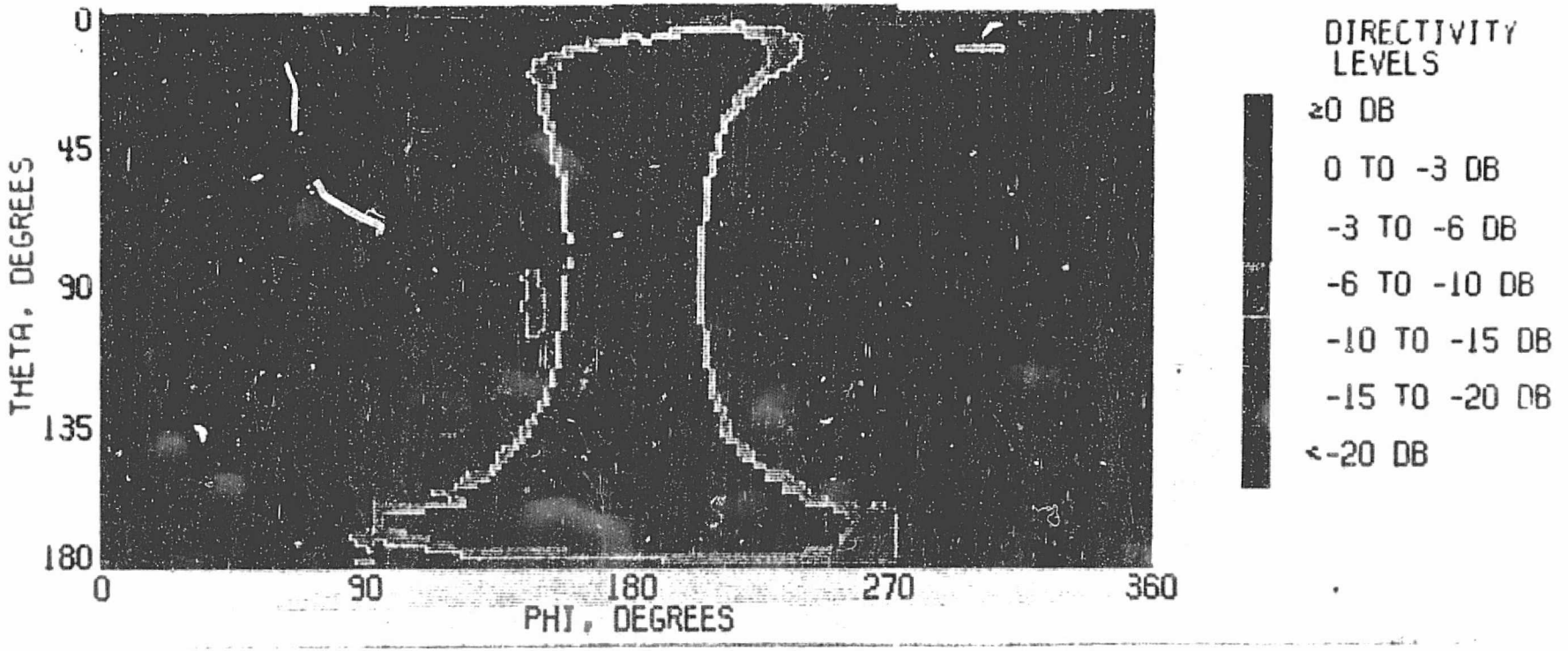

Figure 4-6. Measured color volumetric pattern of an 8 element linear array relative to isotropic directivity.

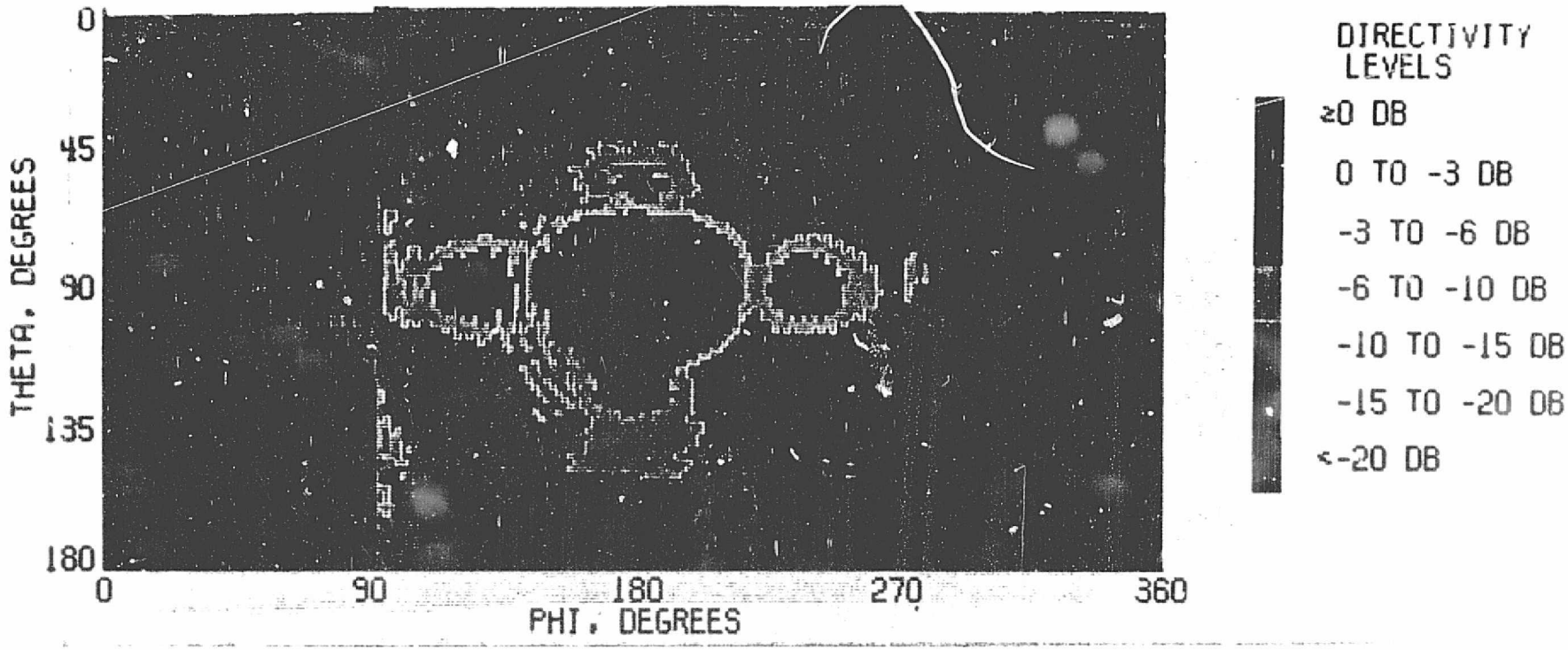

Figure 4-7. Measured color volumetric pattern of a 64 element planar array relative to isotropic directivity.

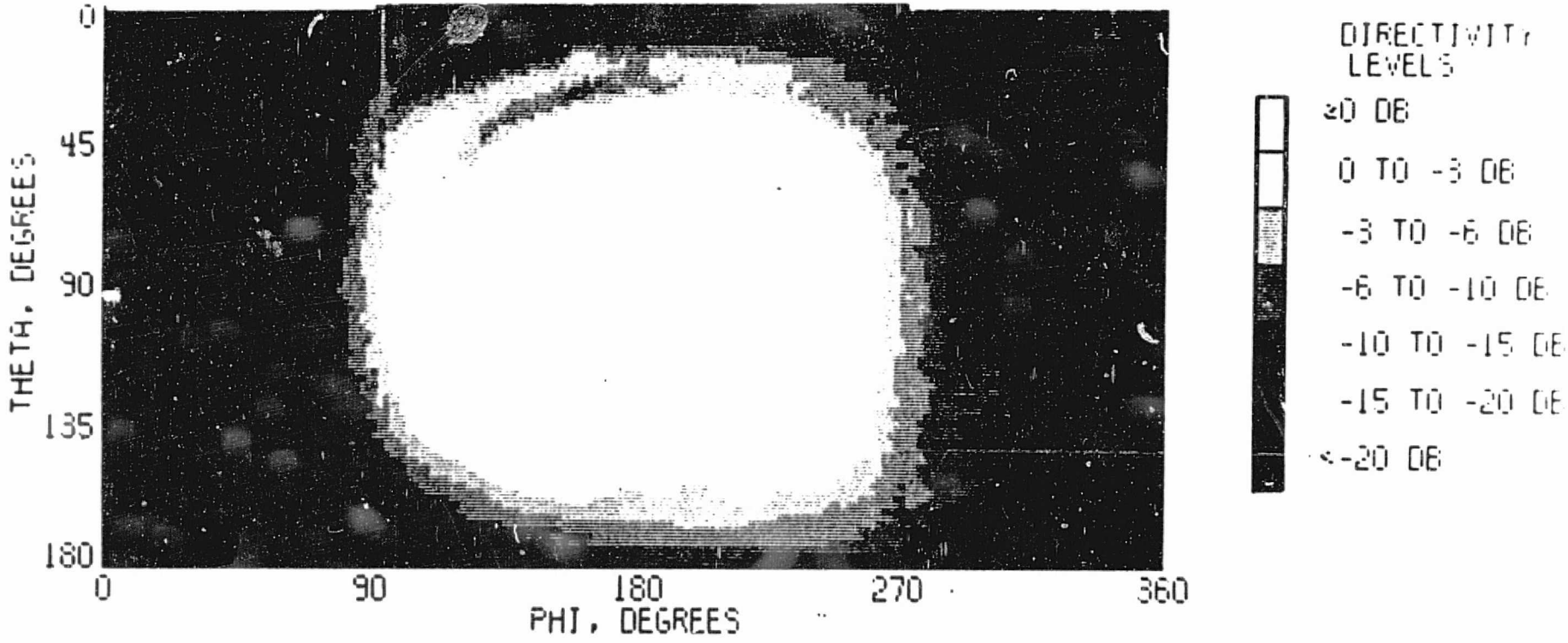

Figure 4-8. Measured volumetric pattern of a microstrip disk relative to isotropic directivity.

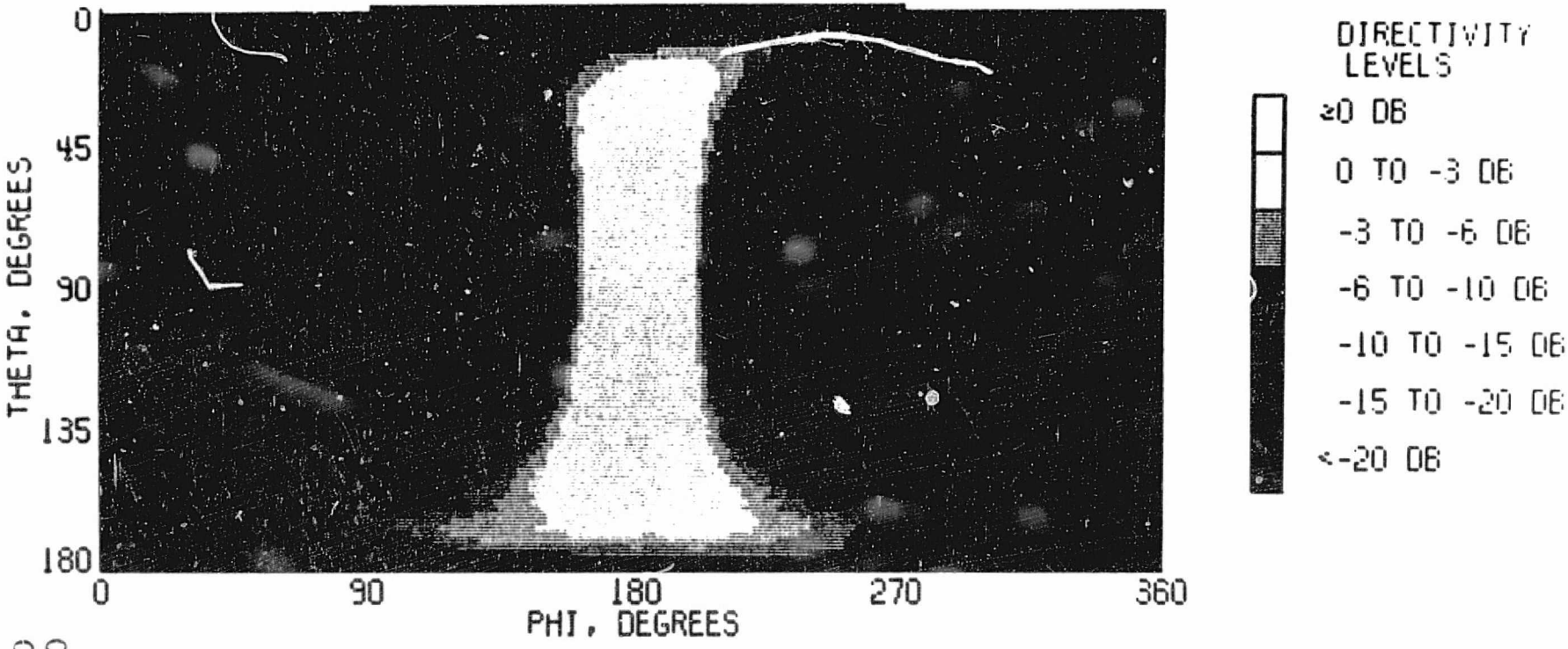

Figure 4-9. Measured volumetric pattern of an 8 element linear array relative to isotropic directivity.

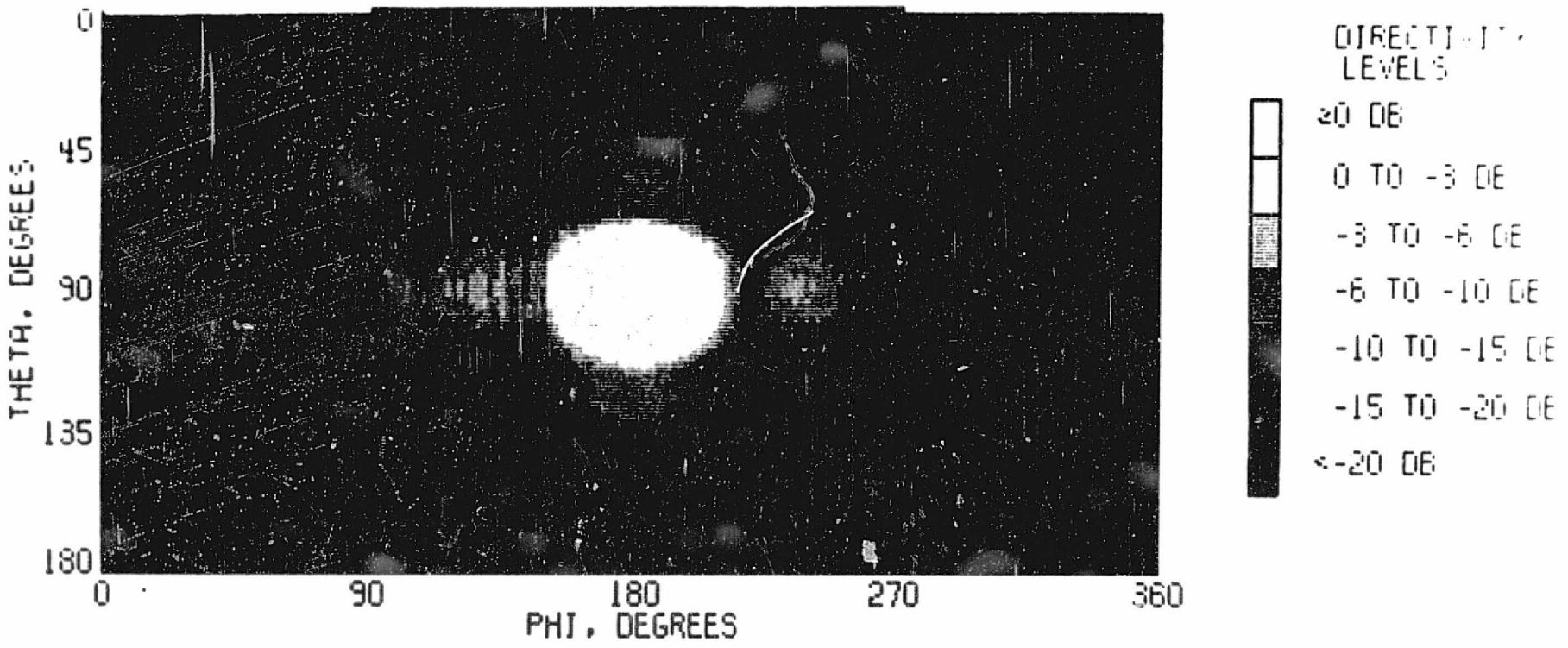

Figure 4-10. Measured volumetric pattern of a 64 element planar array relative to isotropic directivity.

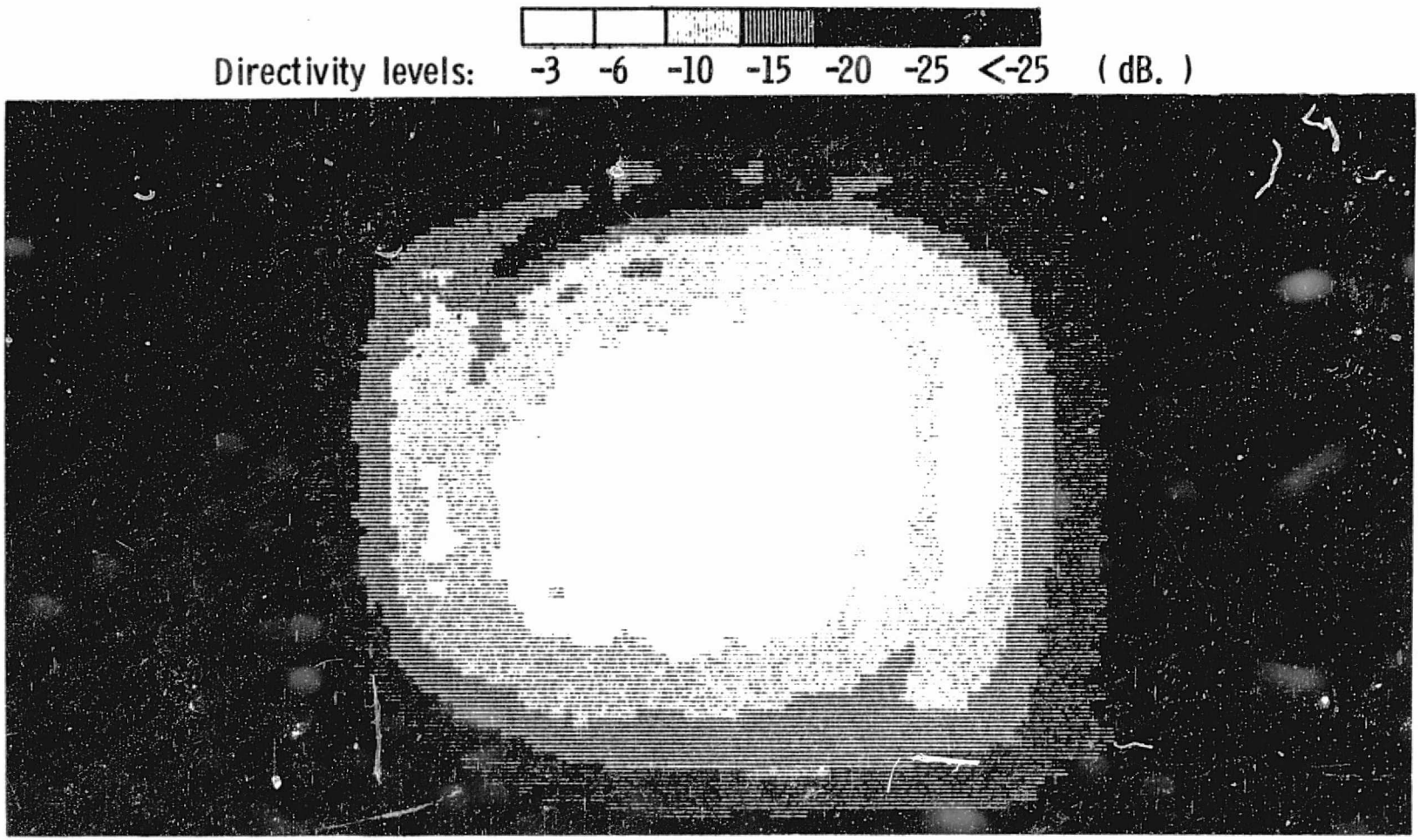

Figure 4-11. Measured volumetric pattern of a microstrip disk normalized to the beam peak.

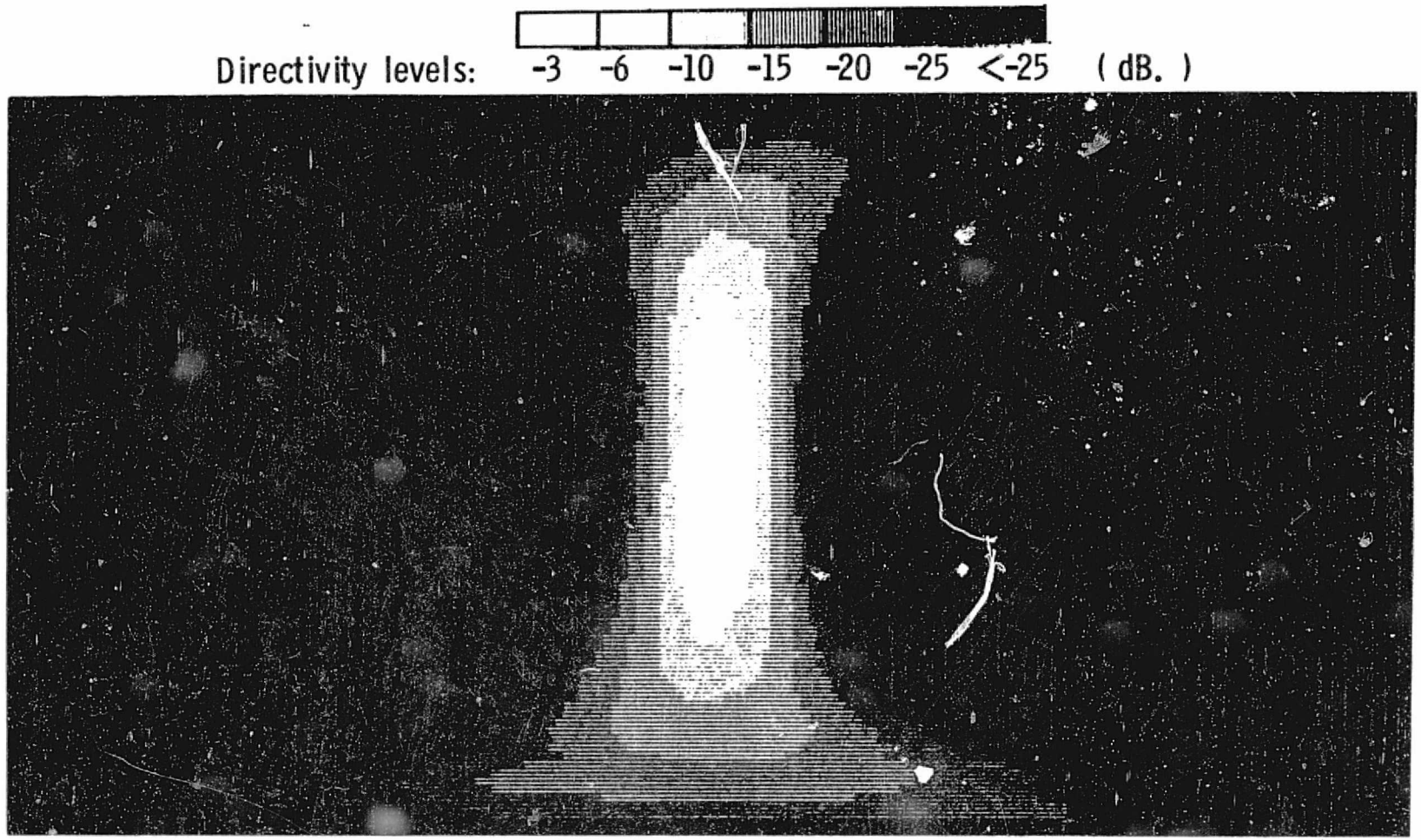

Figure 4-12. Measured volumetric pattern of an 8 element linear array normalized to the beam peak.

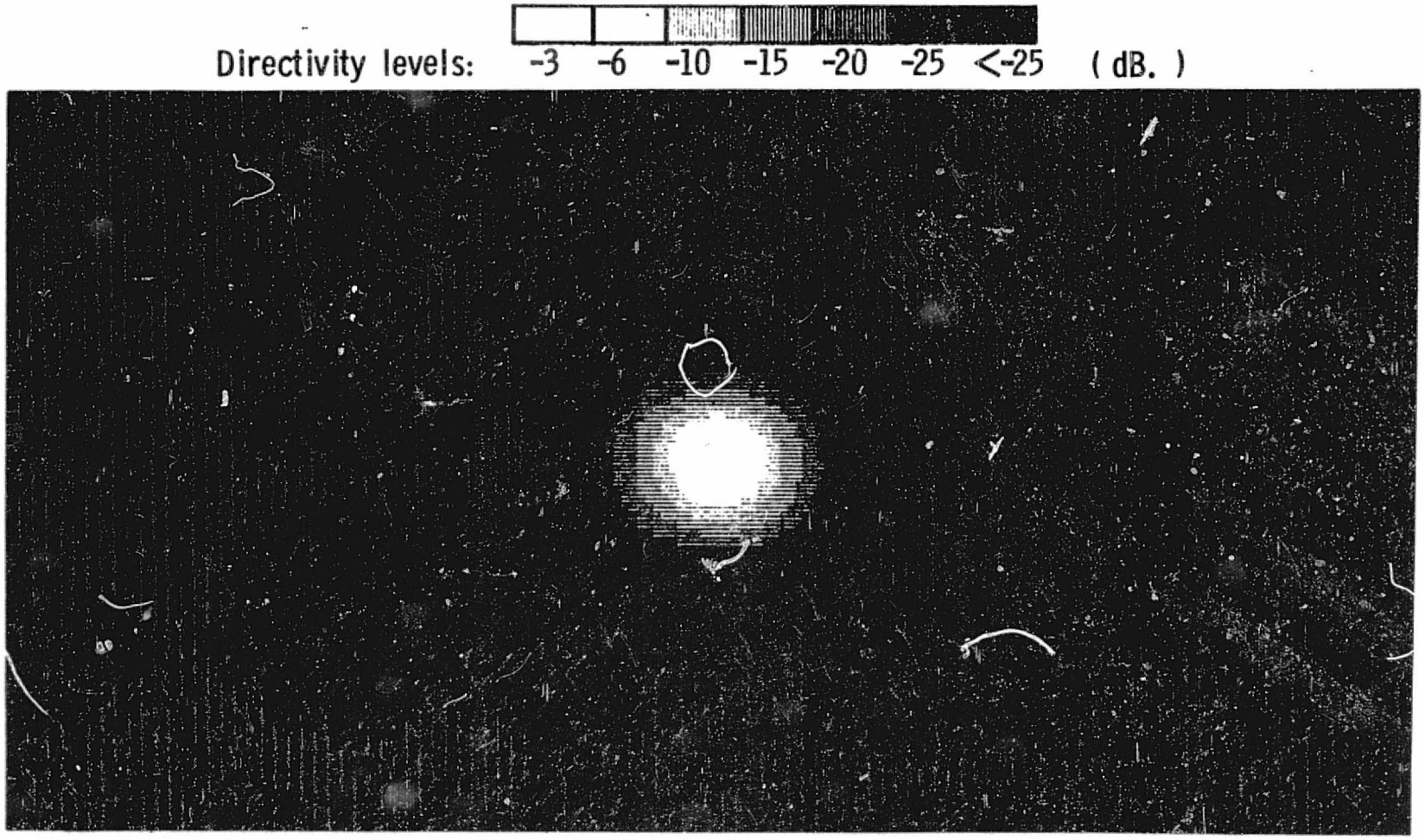

Figure 4-13. Measured volumetric pattern of a 64 element planar array normalized to the beam peak.

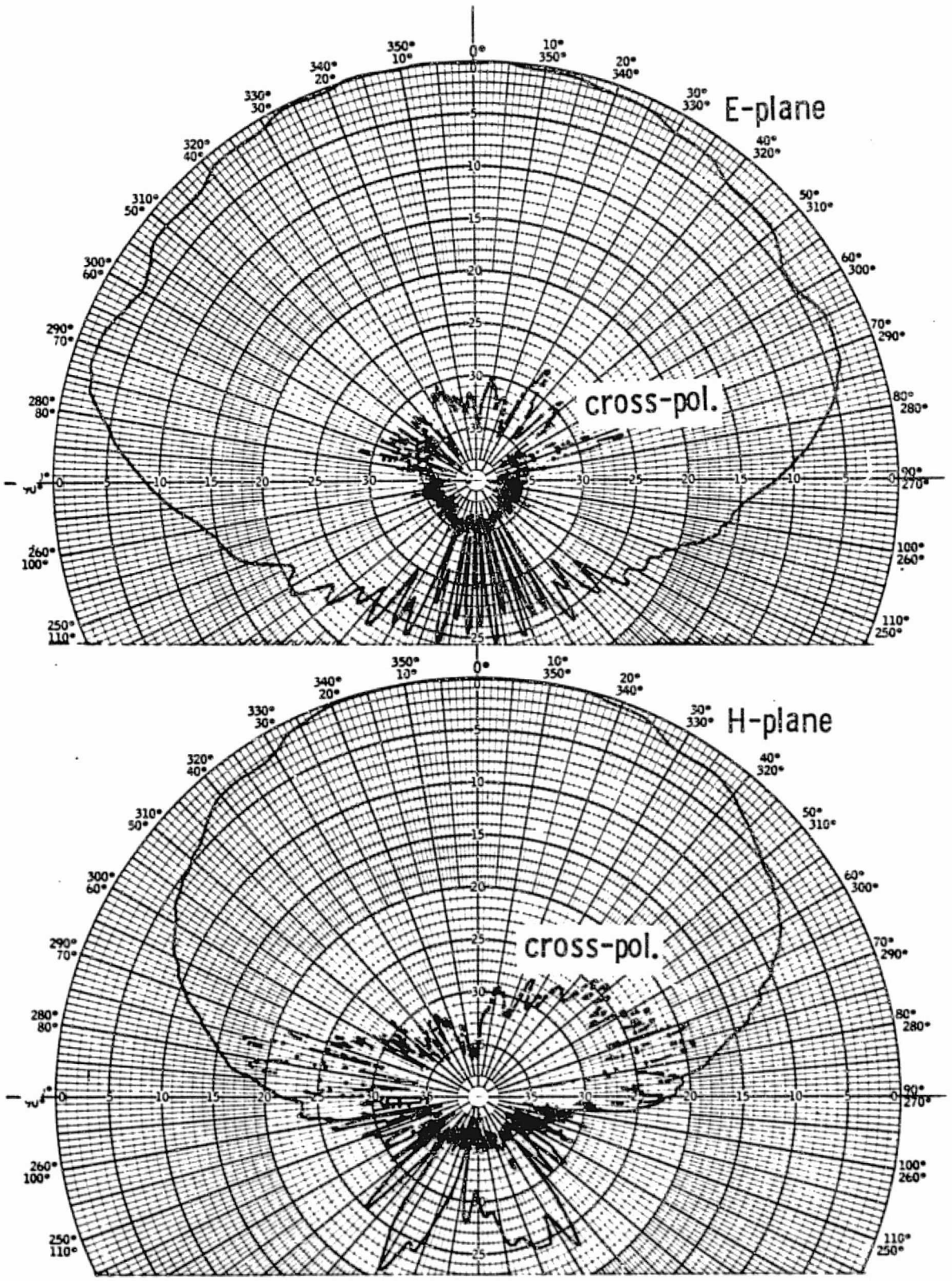

Figure 4-14. E-plane, H-plane, and cross-polarized microstrip disk patterns on a 0.6 meter ground plane at 5.5 GHz.

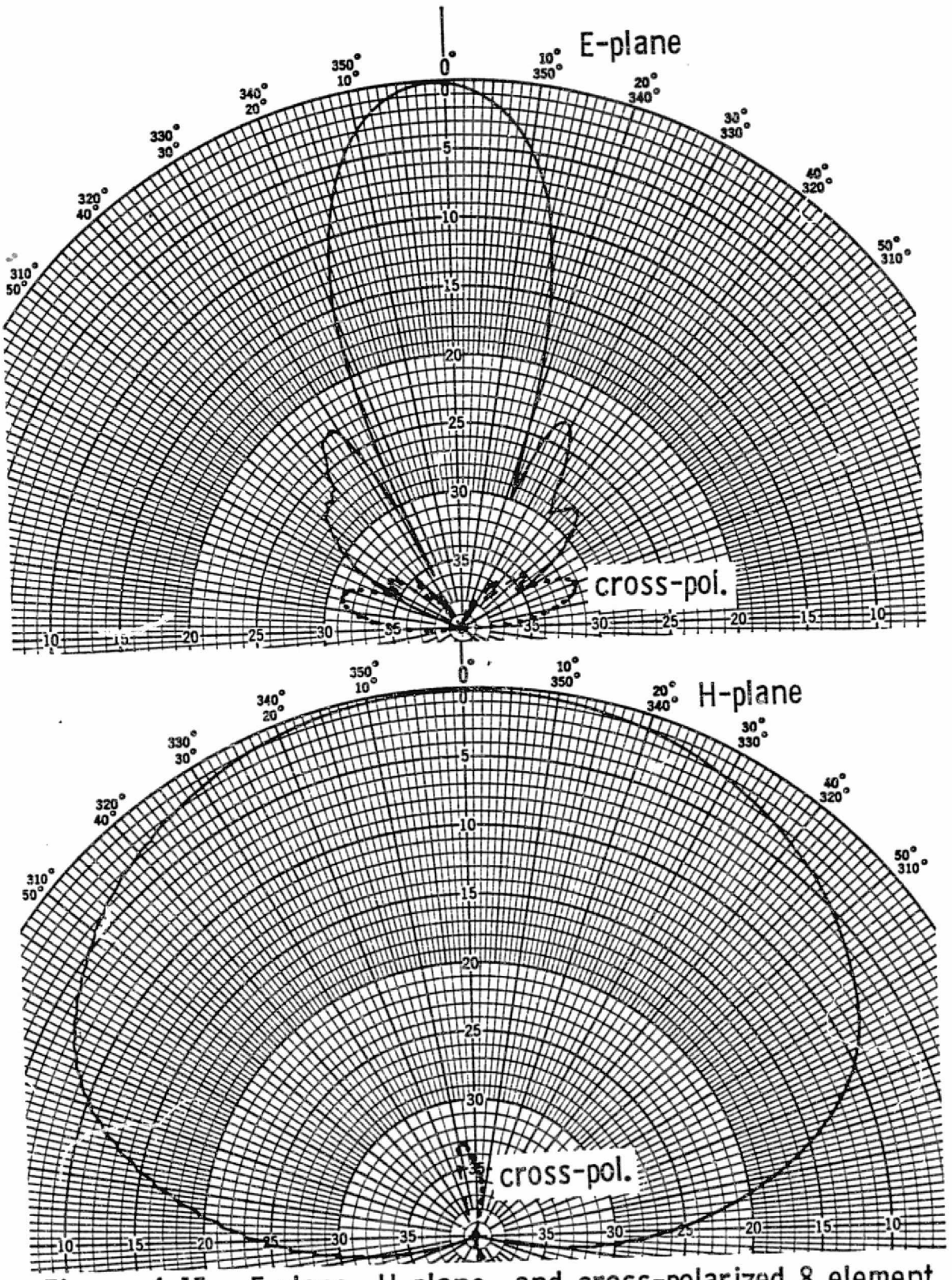

Figure 4-15. E-plane, H-plane, and cross-polarized 8 element linear array patterns on a 0.6 meter ground plane at 5.45 GHz.

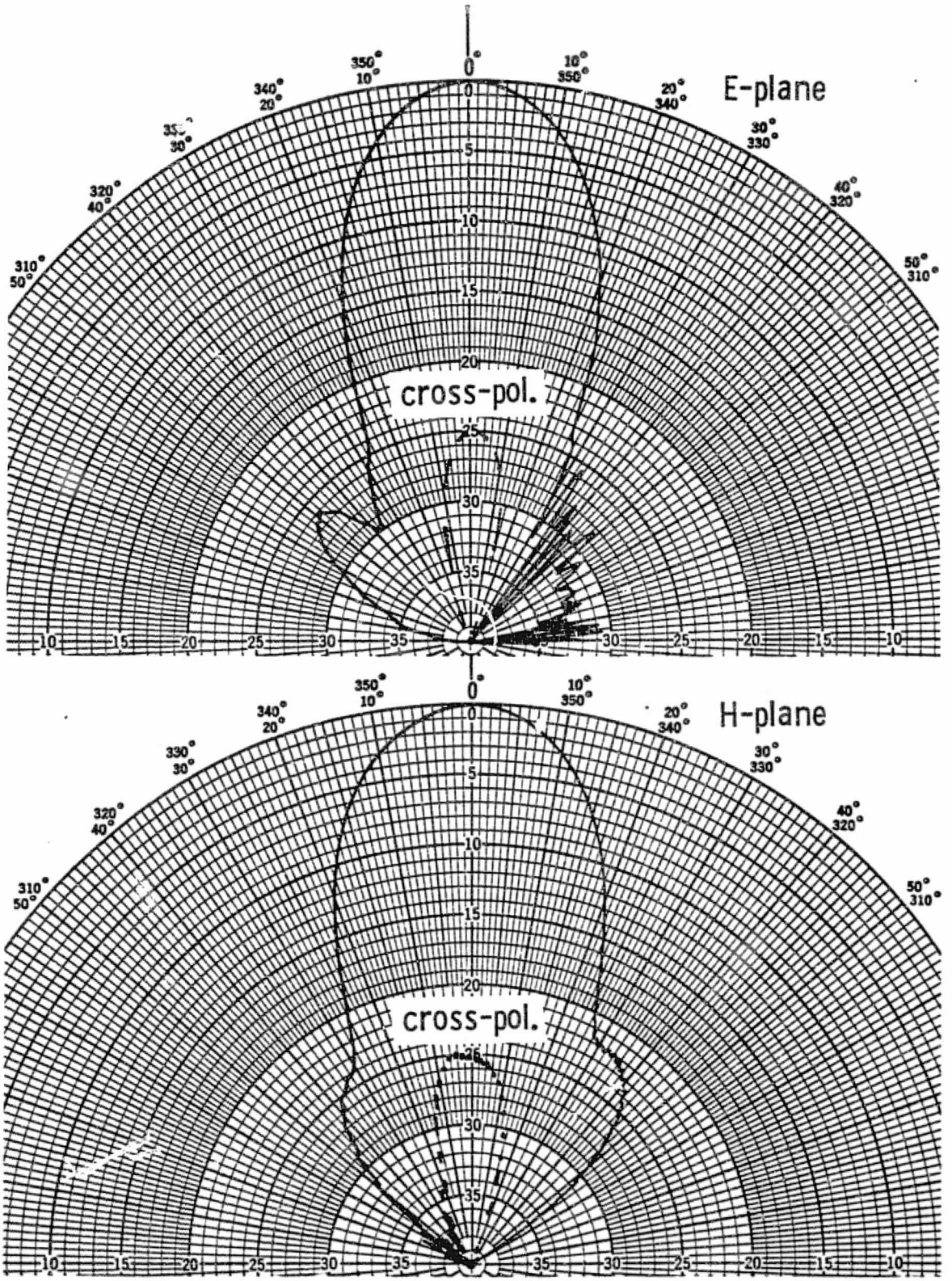

Figure 4-16. E-plane, H-plane, and cross-polarized 64 element planar array patterns on a 0.3 meter ground plane at 5.35 GHz.

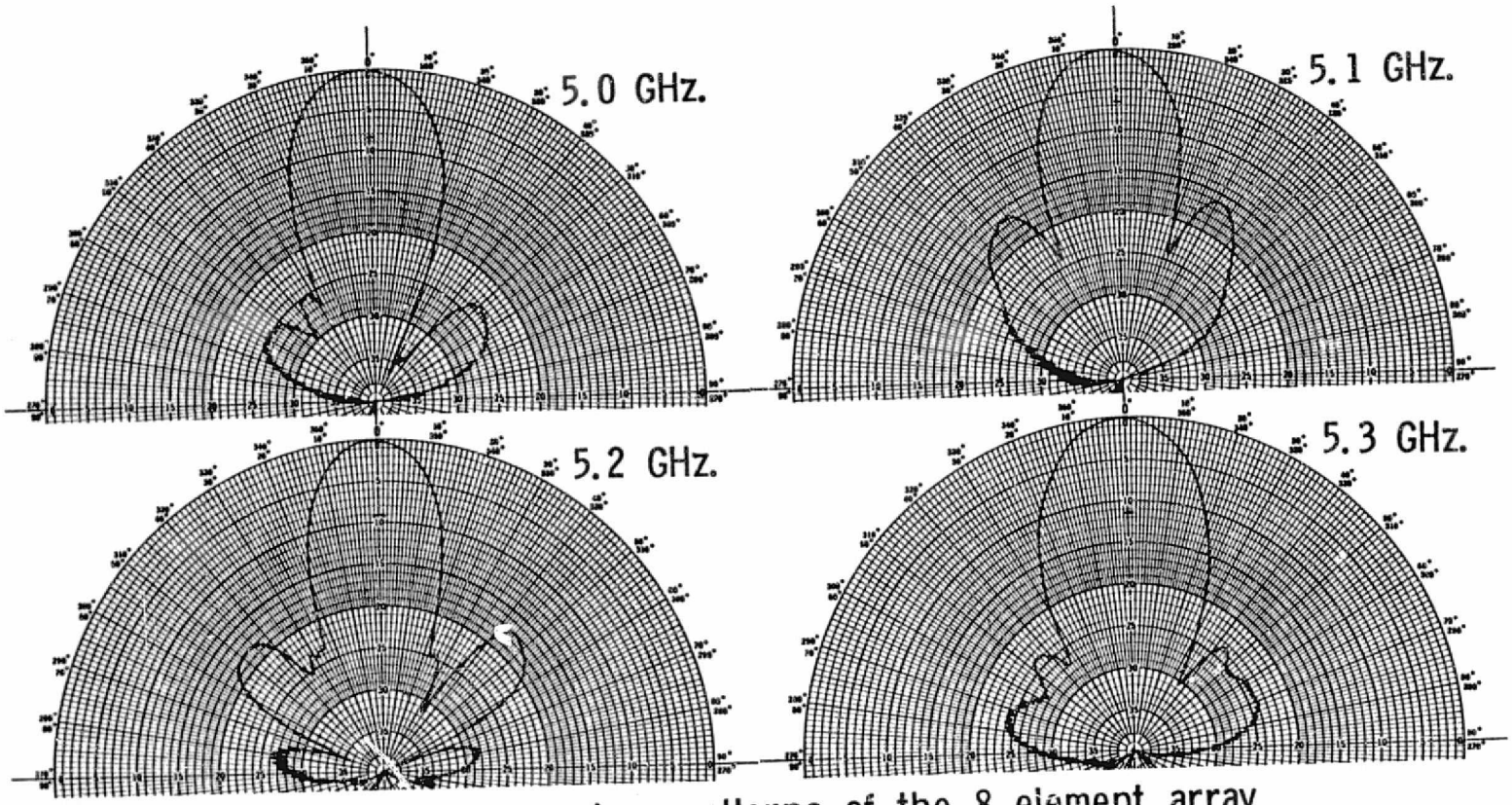

Figure 4-17a. E-plane patterns of the 8 element array with frequency as a parameter.

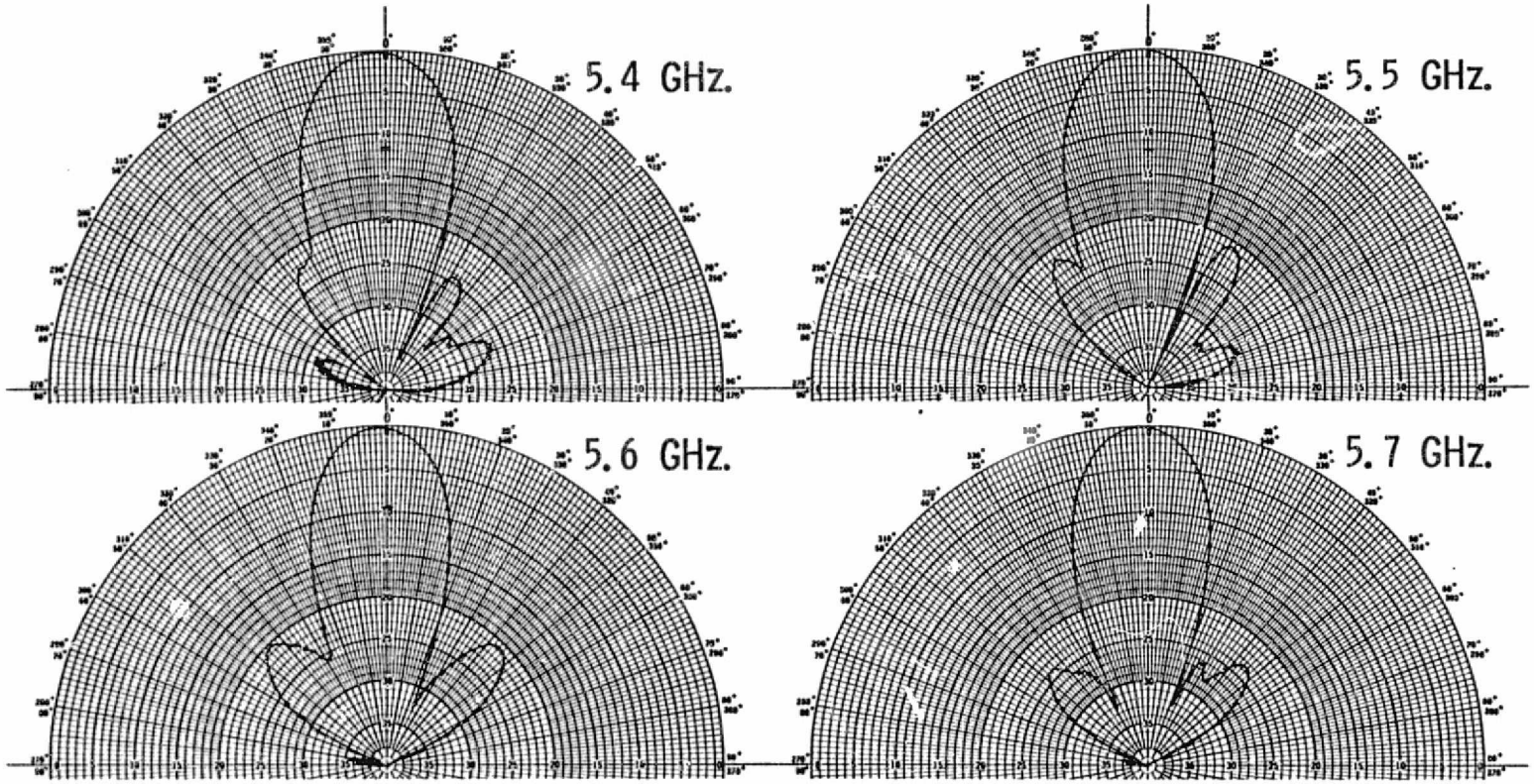

Figure 4-17b. E-plane patterns of the 8 element array with frequency as a parameter.

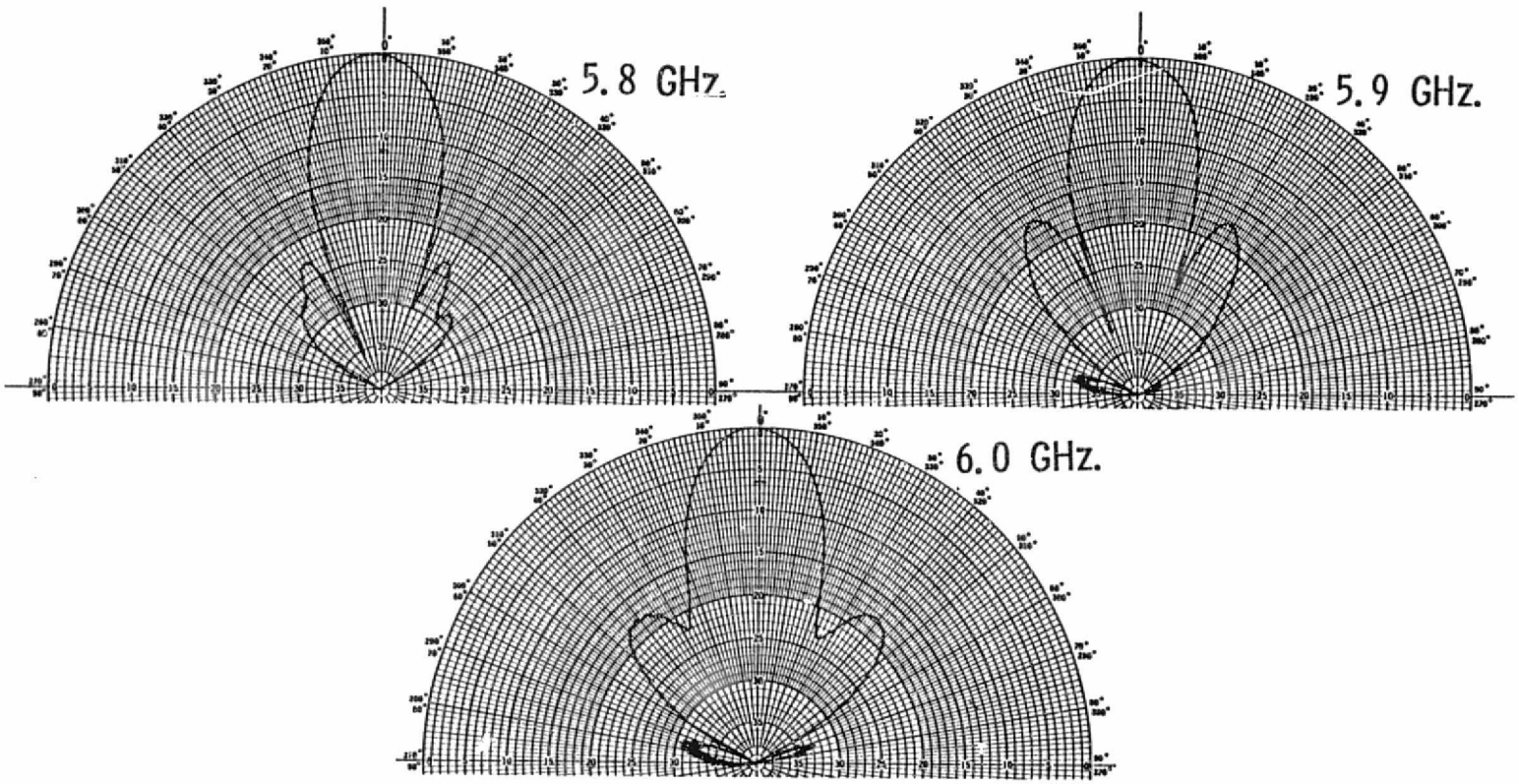

Figure 4-17c. E-plane patterns of the 8 element array with frequency as a parameter.

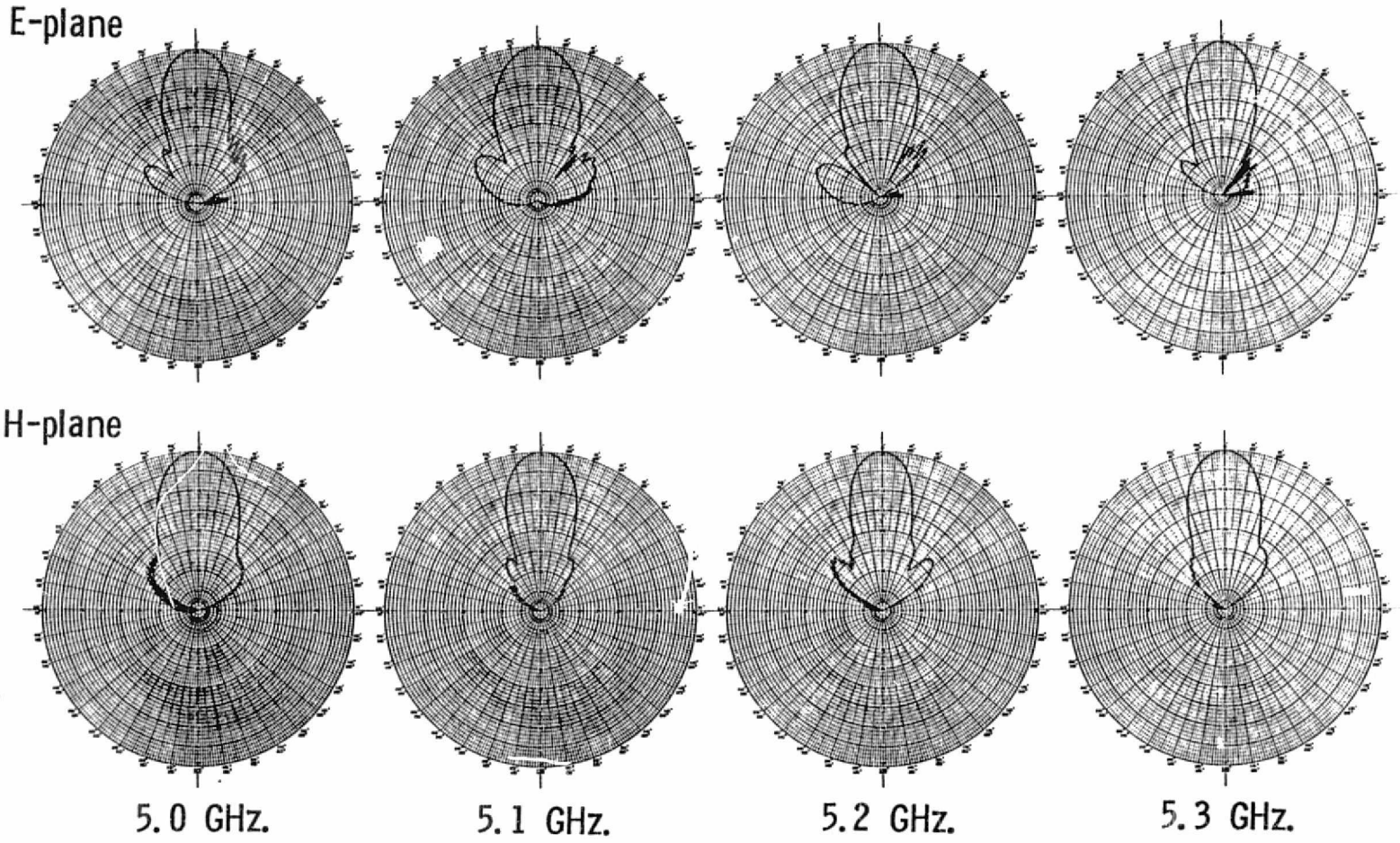

Figure 4-18a. E-plane and H-plane patterns of the 64 element planar array

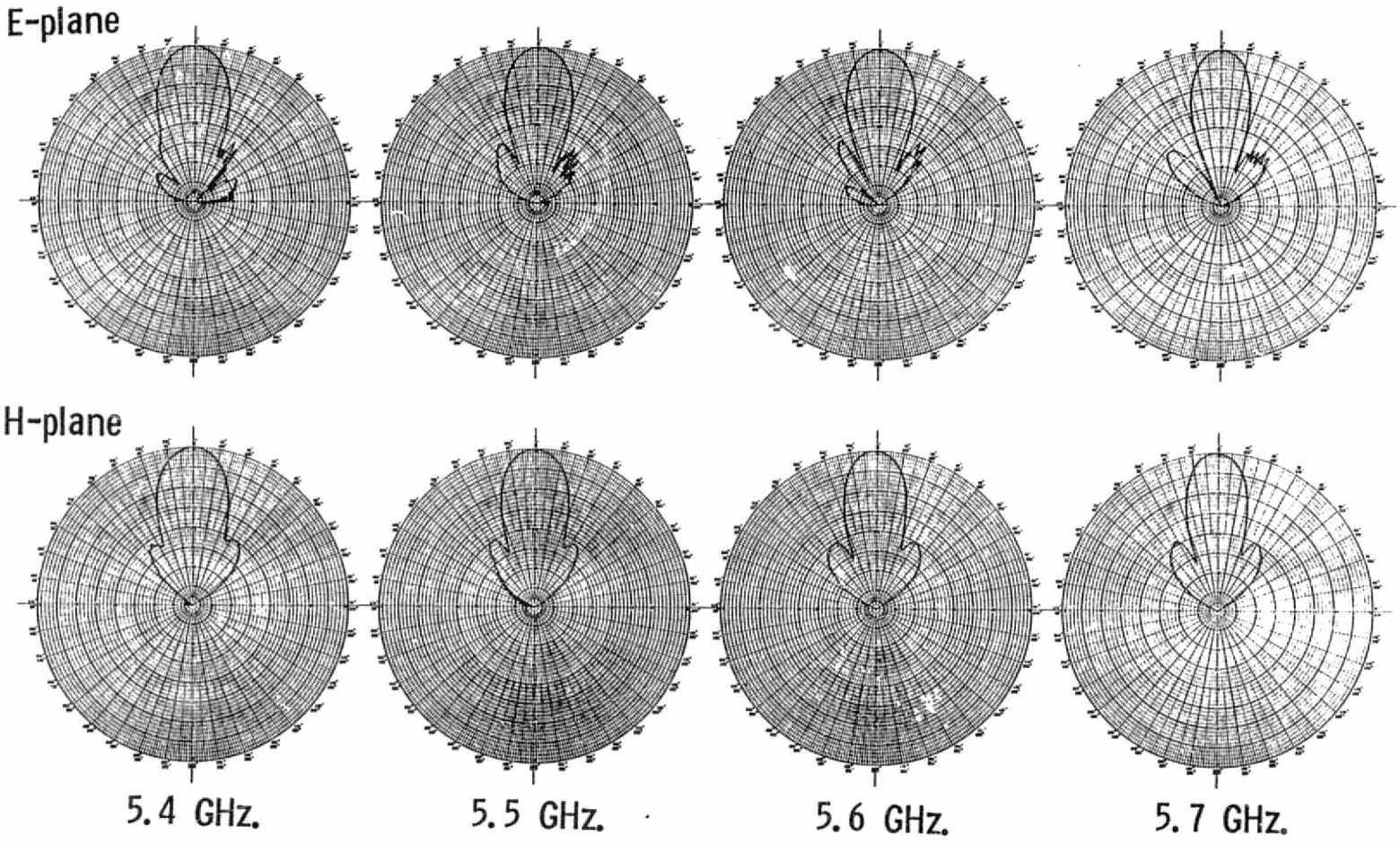

Figure 4-18b. E-plane and H-plane patterns of the 64 element planar array

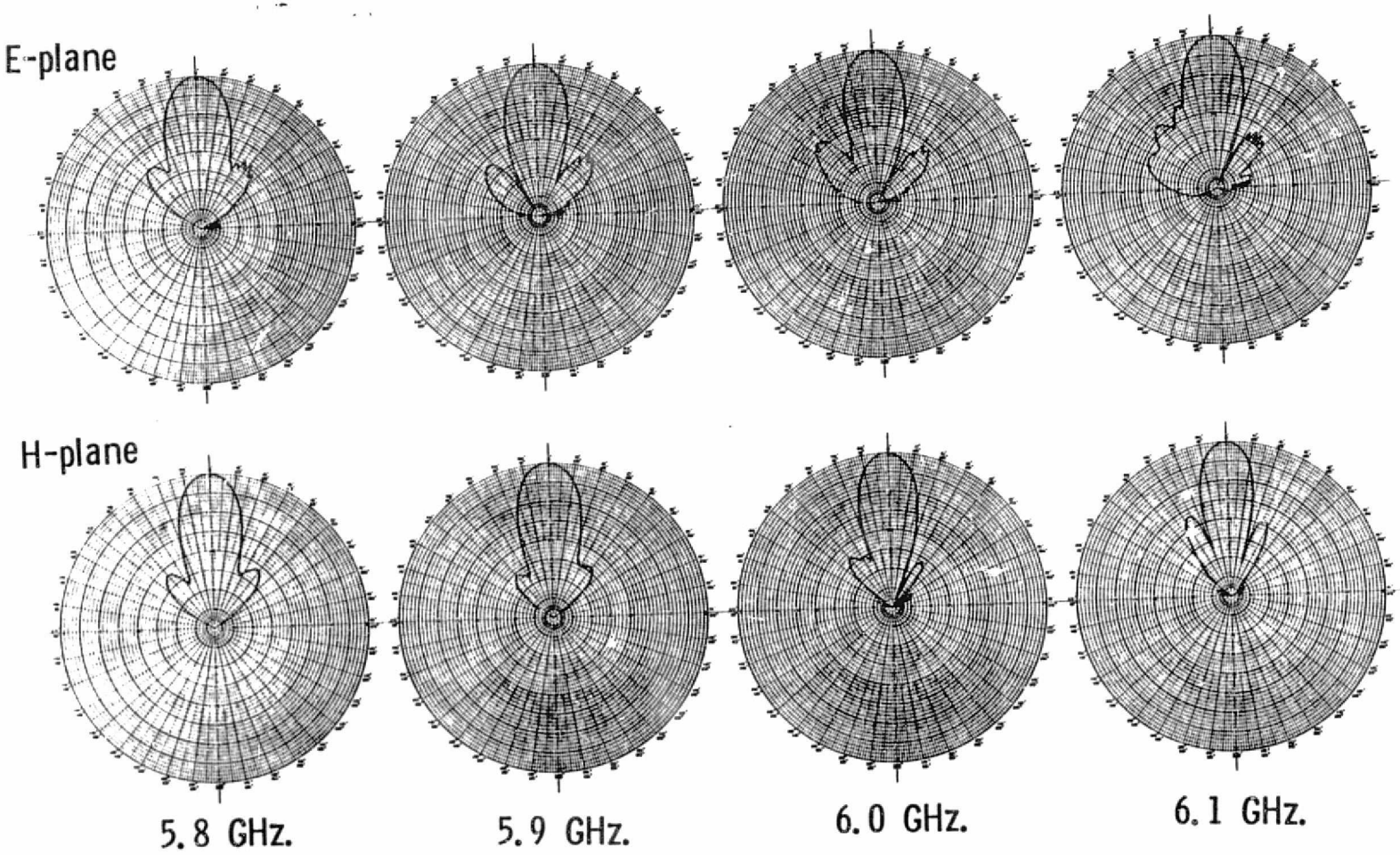

Figure 4-18c. E-plane and H-plane patterns of the 64 element planar array

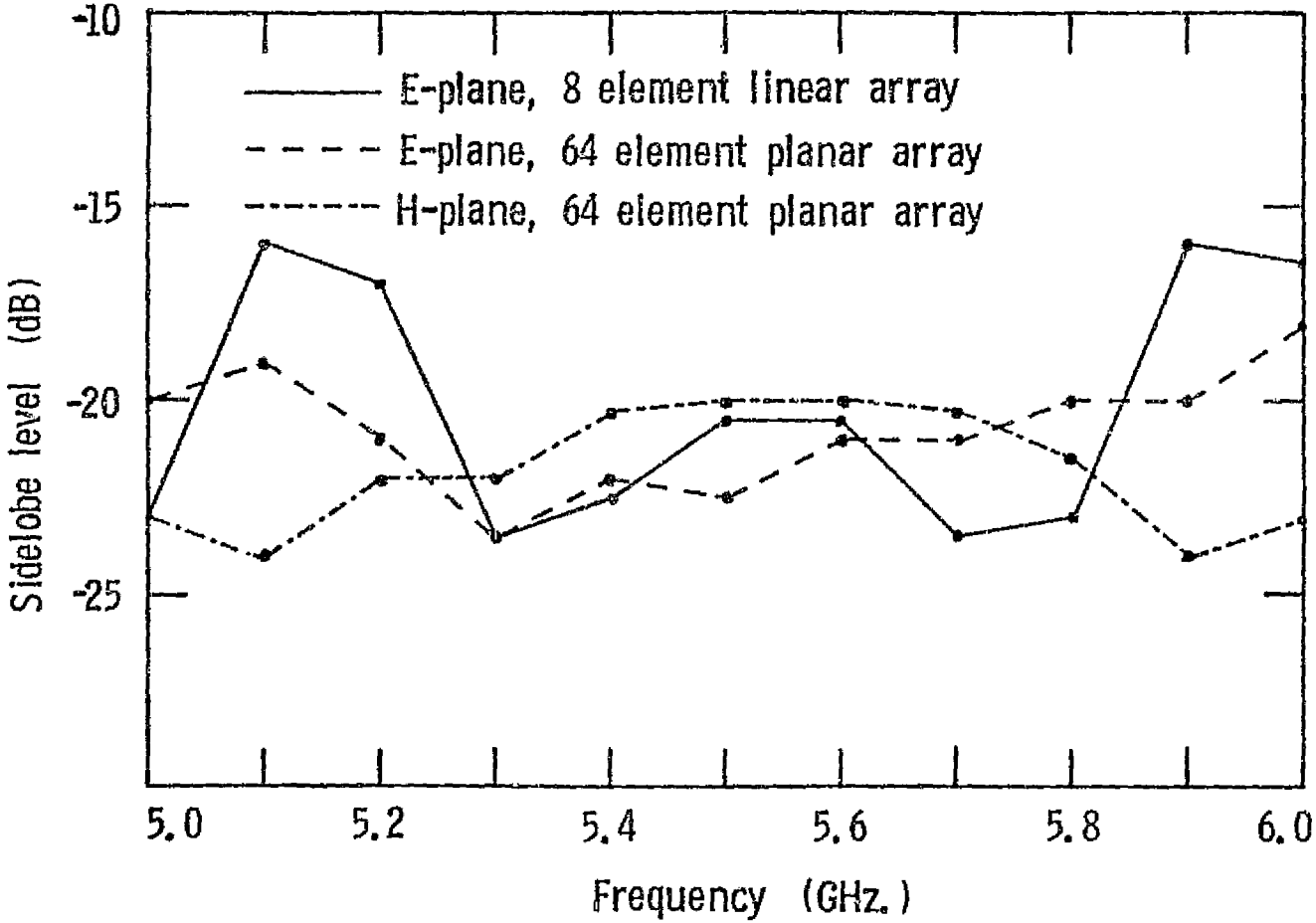

Figure 4-19. Sidelobe level versus frequency.

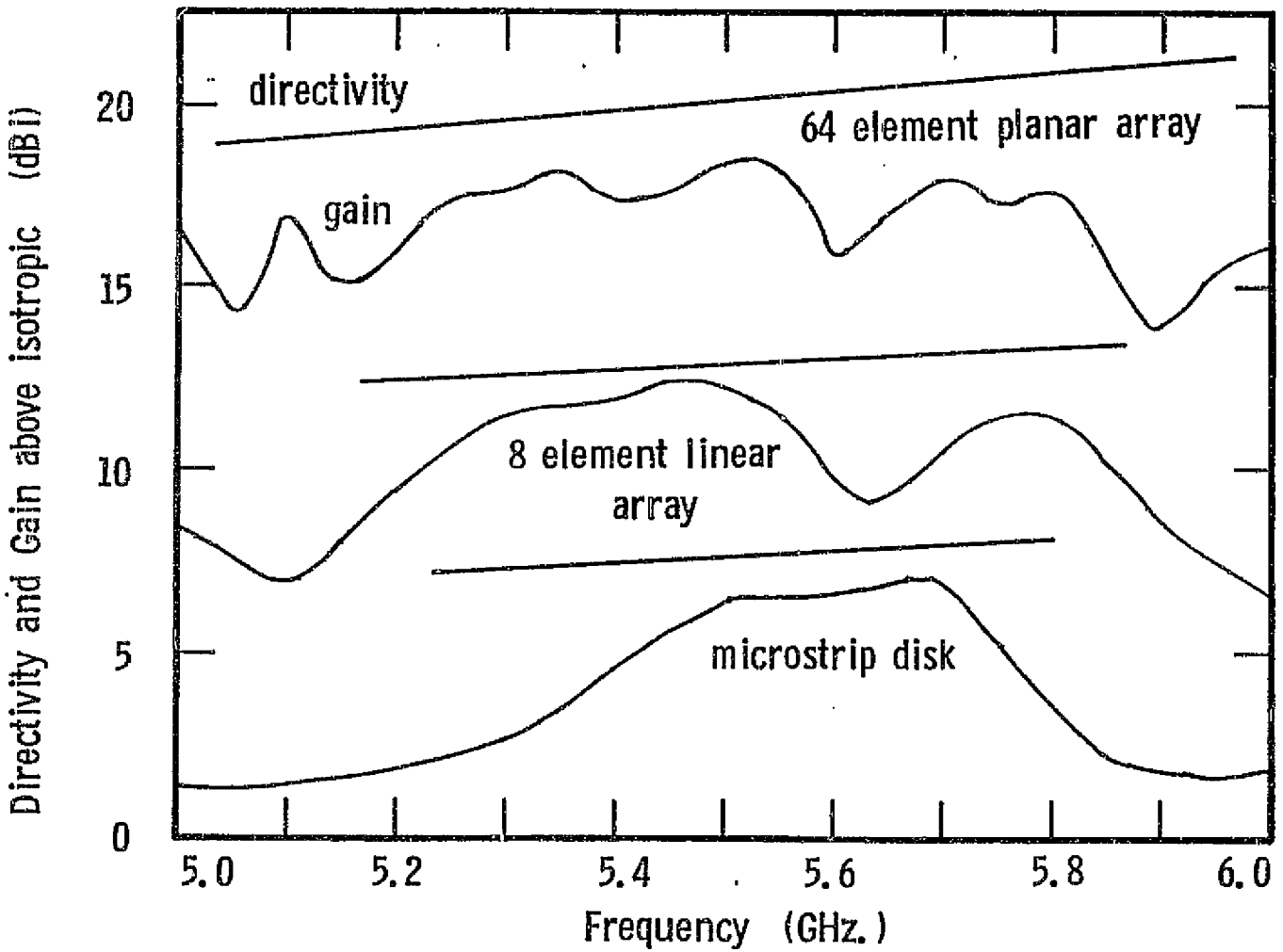

Figure 4-20. Gain and directivity versus frequency for the microstrip disk, the 8 element linear array, and the 64 element planar array.

Impedance Performance

The impedance of an antenna and the feed network limit the efficiency and the bandwidth of the system.

The measurement of impedance is made at the single input port of each antenna system with a swept frequency network analyzer, figure 4-20. The analyzer characterizes the antenna in terms of the complex small-signal scattering parameters as a function of frequency. The scattering parameters determine the magnitude and phase of the reflection coefficient which is displayed on a Smith chart, figures 4-22, 4-23, 4-24. The scattering parameters and the Smith chart are normalized to a 50-ohm characteristic impedance.

Another important impedance property is the voltage standing wave ratio (VSWR). VSWR can be expressed in terms of the reflection coefficient ρ:

$$VSWR = (1 + \rho)/(1 - \rho)$$

The 2:1 and 3:1 VSWR bandwidth for each system is included in the summary, figure 4-1.

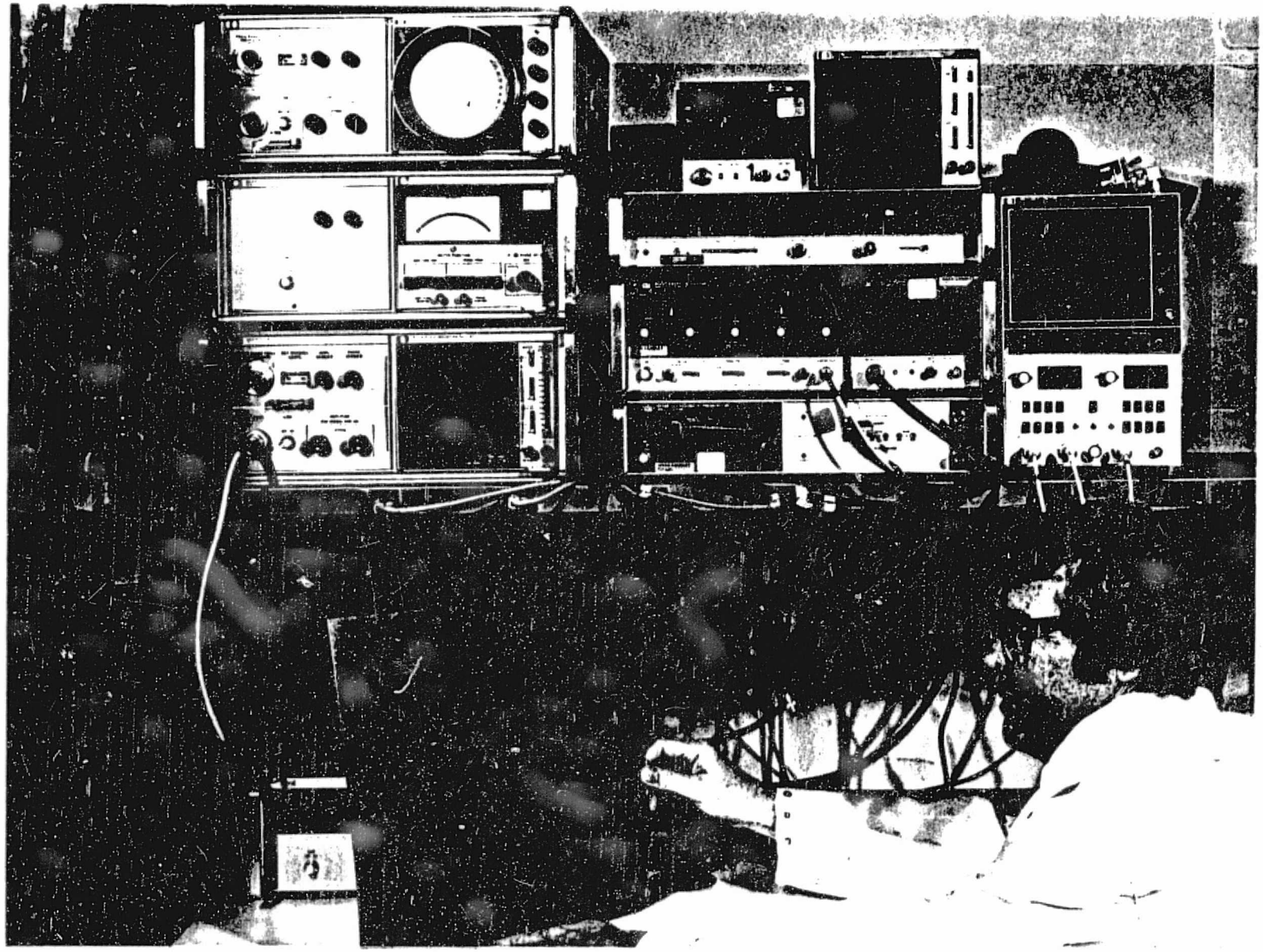

Figure 4-21. The network analyzer measurement system.

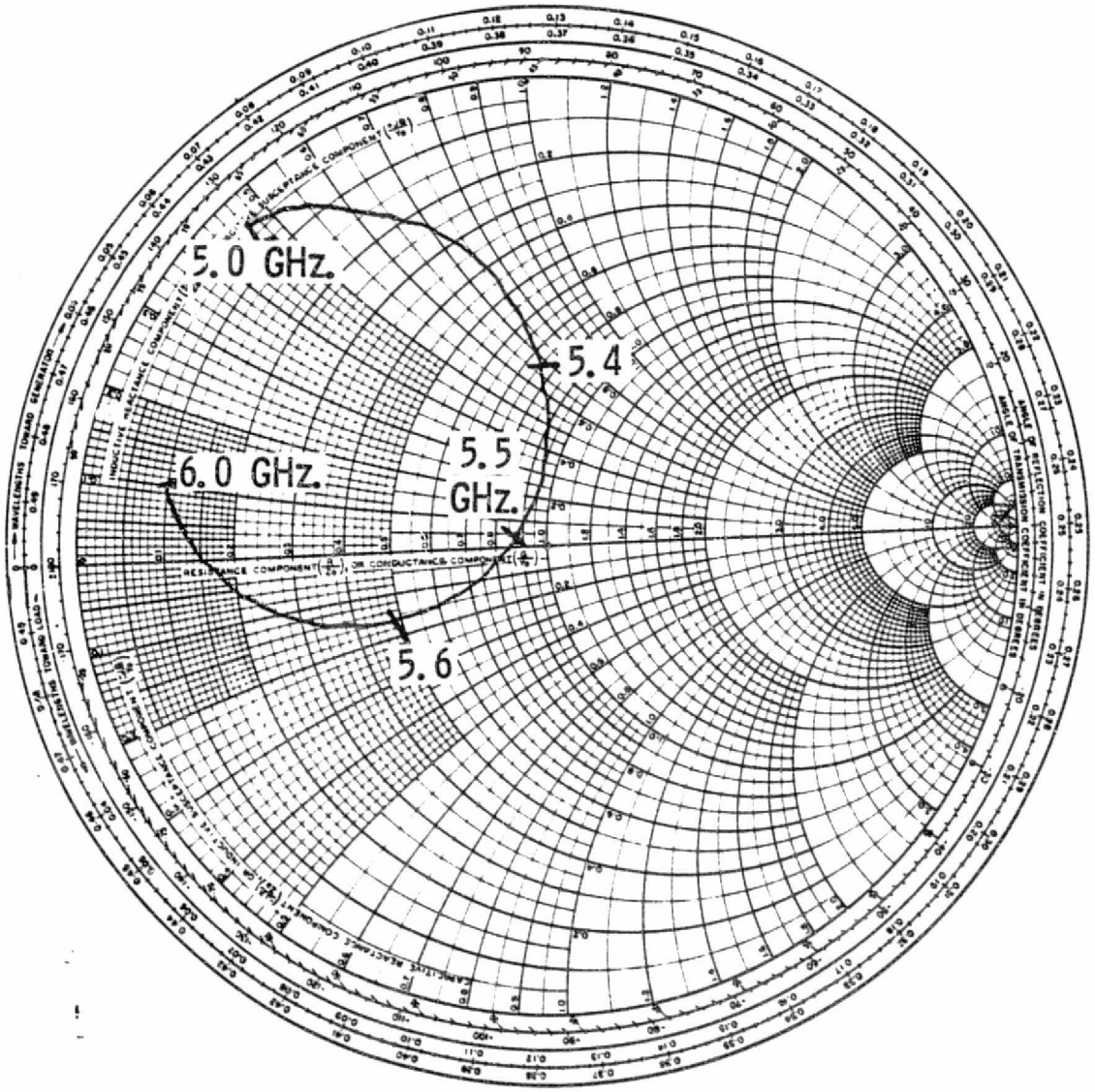

Figure 4-22. The impedance of a microstrip disk.

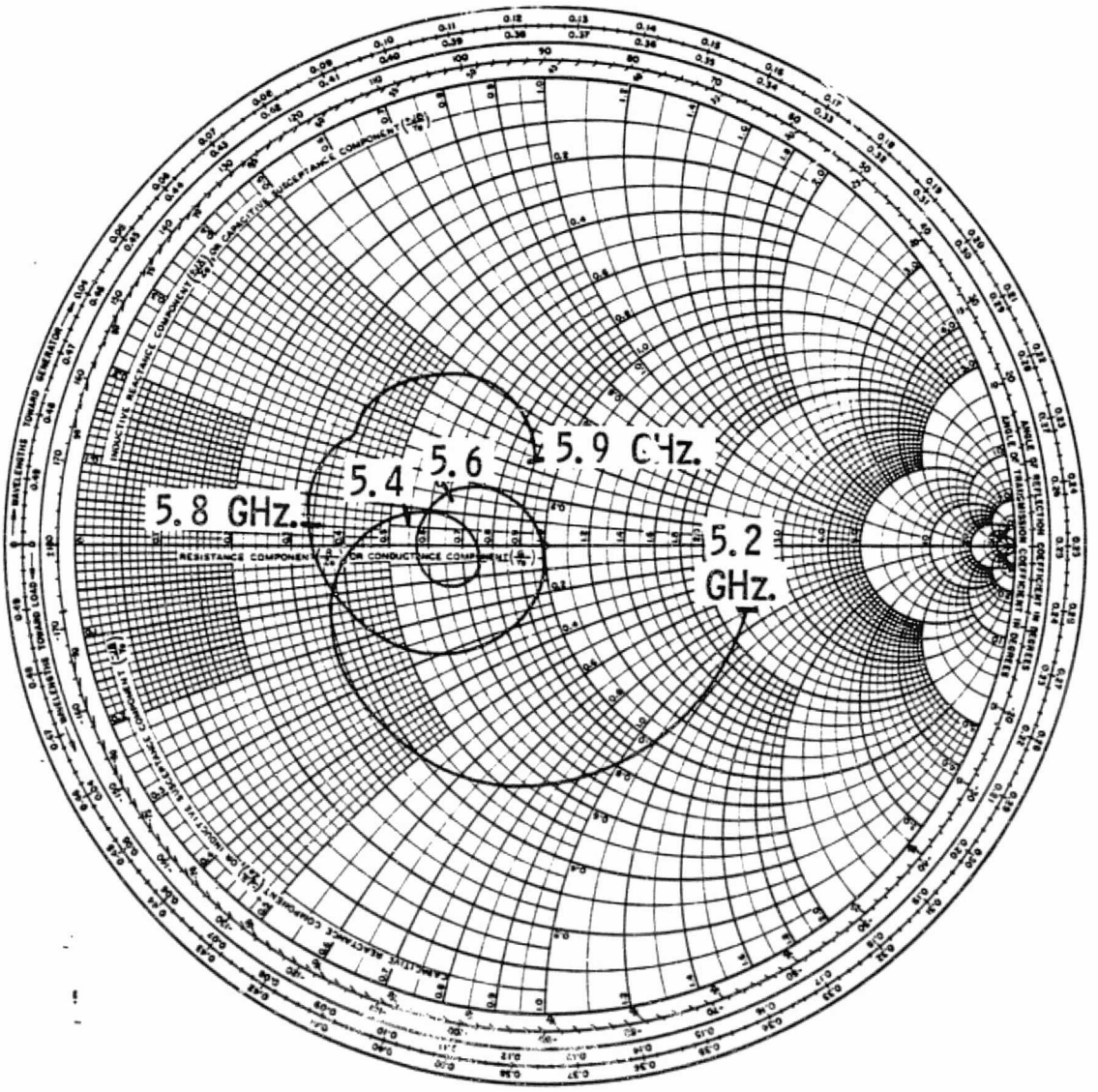

Figure 4-23. The impedance of an 8 element linear array.

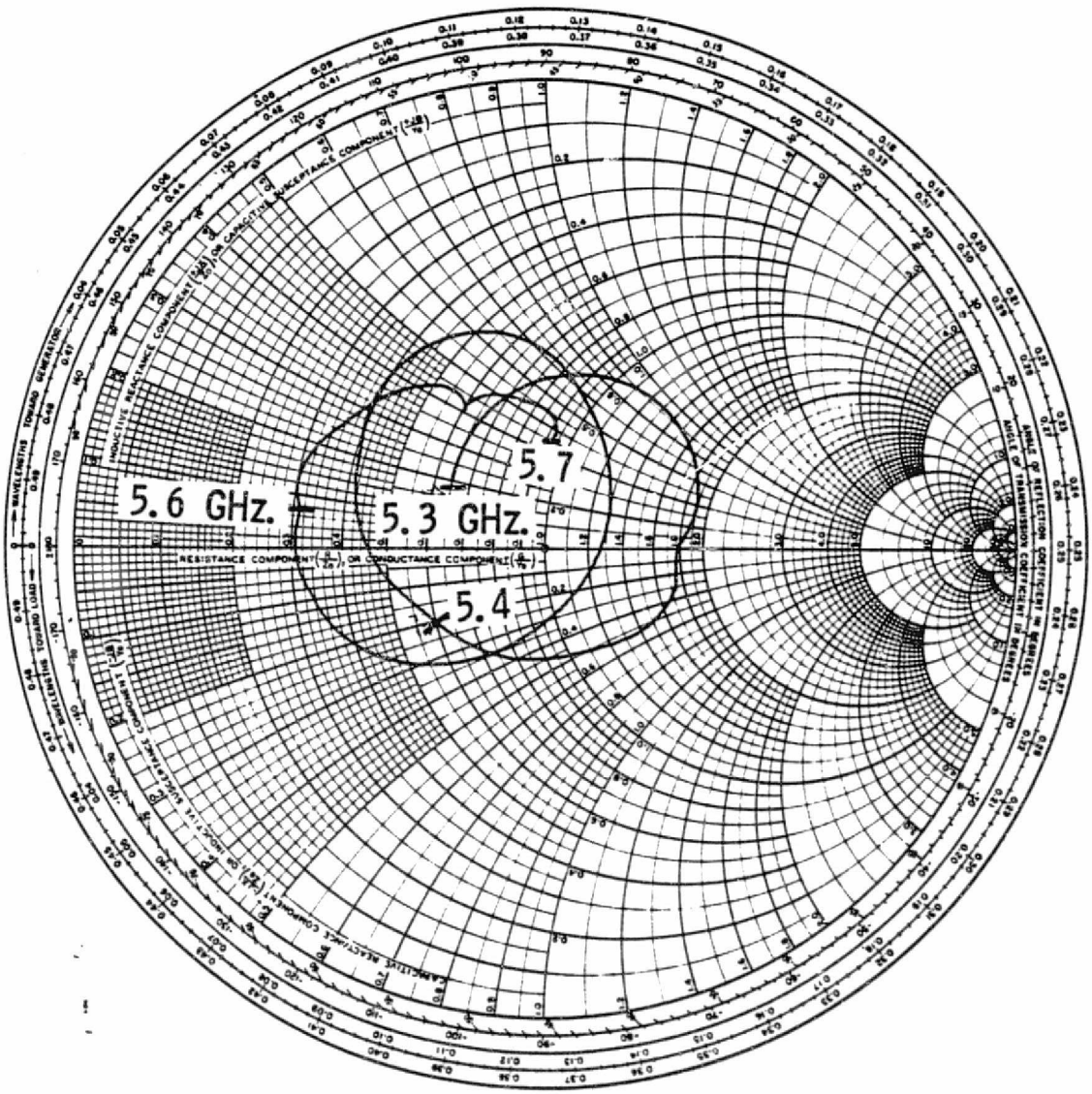

Figure 4-24. The impedance of the 64 element planar array.

CHAPTER 5 CONCLUSIONS AND RECOMMENDATIONS

Conclusions

This project demonstrated the feasibility of designing and fabricating microstrip disk arrays with simple low cost techniques. Design data was presented for microstrip elements and arrays including the effects of the protective covers, the mutual interaction between elements, and stripline feed network design. Low cost multilayer laminate fabrication techniques were also investigated.

Utilizing this design data two C-band low sidelobe arrays were fabricated and tested: an eight element linear and a 64 element planar array. These arrays incorporated stripline Butler matrix feed networks to produce a low sidelobe broadside beam.

The microstrip elements were easily matched with a 3:1 VSWR bandwidth up to 8 percent for the eight element array. Good agreement was obtained between the measured and calculated radiation patterns including the half power beamwidth and the sidelobes. The sidelobes were designed for a -23 dB level. The measured sidelobes for both arrays were less than -20 dB for an 11 percent bandwidth.

Recommendations

The success of this project indicates that a scanning phased array will be practical. A possible cirucit to implement a scanning system is the Butler factorial digital phase switching matrix, figure 5-1. The network produces seven scanned beams. They result from seven progressive phase distributions with a cosine amplitude distribution.

The far field patterns for this network were calculated. An H-plane scanning array produces the patterns in figure 5-2. And the E-plane scanning array produces the patterns of figure 5-3.

There will be many compromises in the design of the scanning array. For example, one compromise is when the large scan angle grating lobes begin to appear for a .5 wavelength spacing as in figure 5-3. For the same angle a .42 wavelength element spacing will decrease the effect of the grating lobe; however, the half power beamwidth of the main lobe will increase. A good compromise will consider the trade-off between limited scanning, element spacing, and beamwidth.

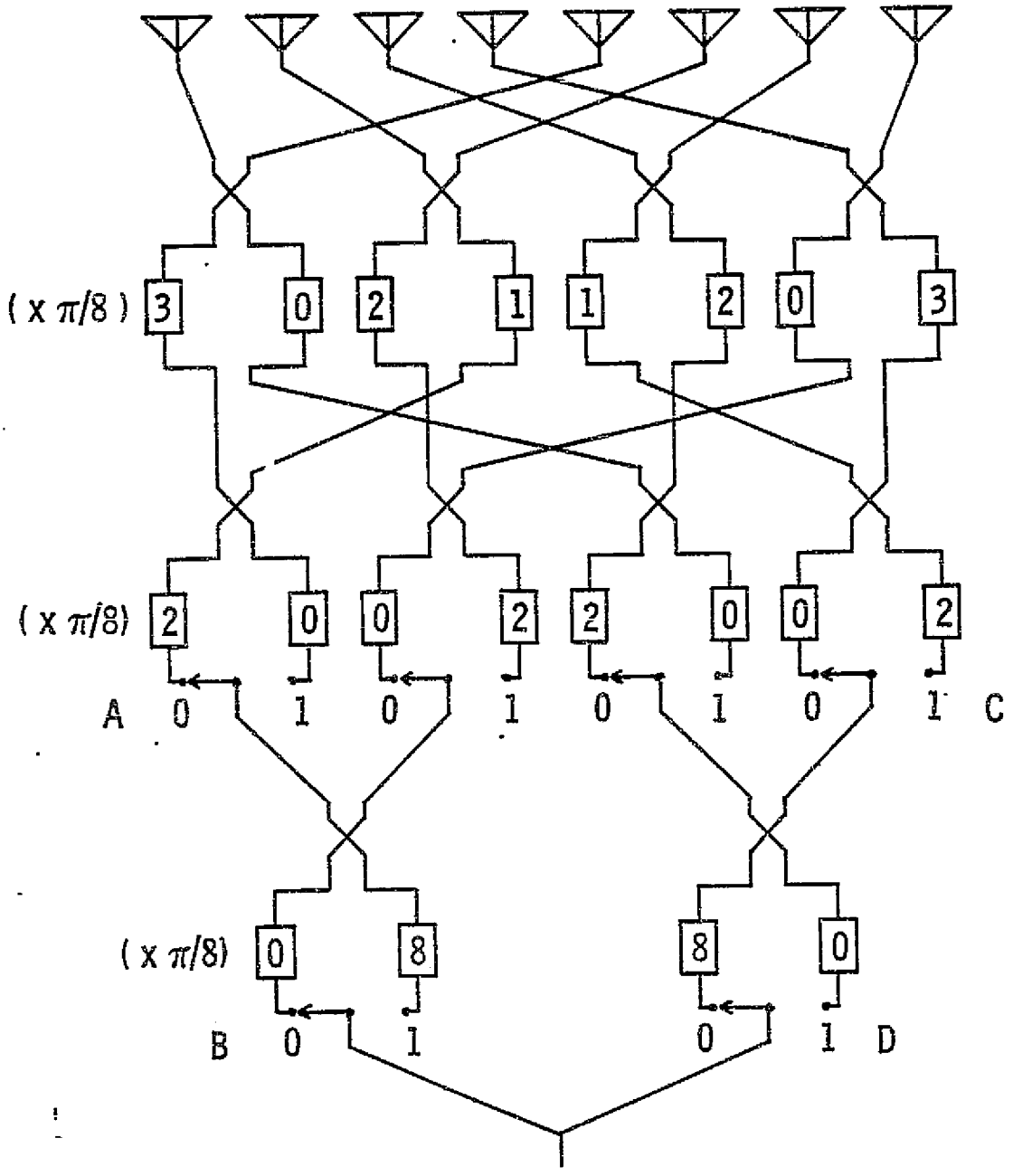

Figure 5-1. The digital switching Butler matrix for cosine tapers.

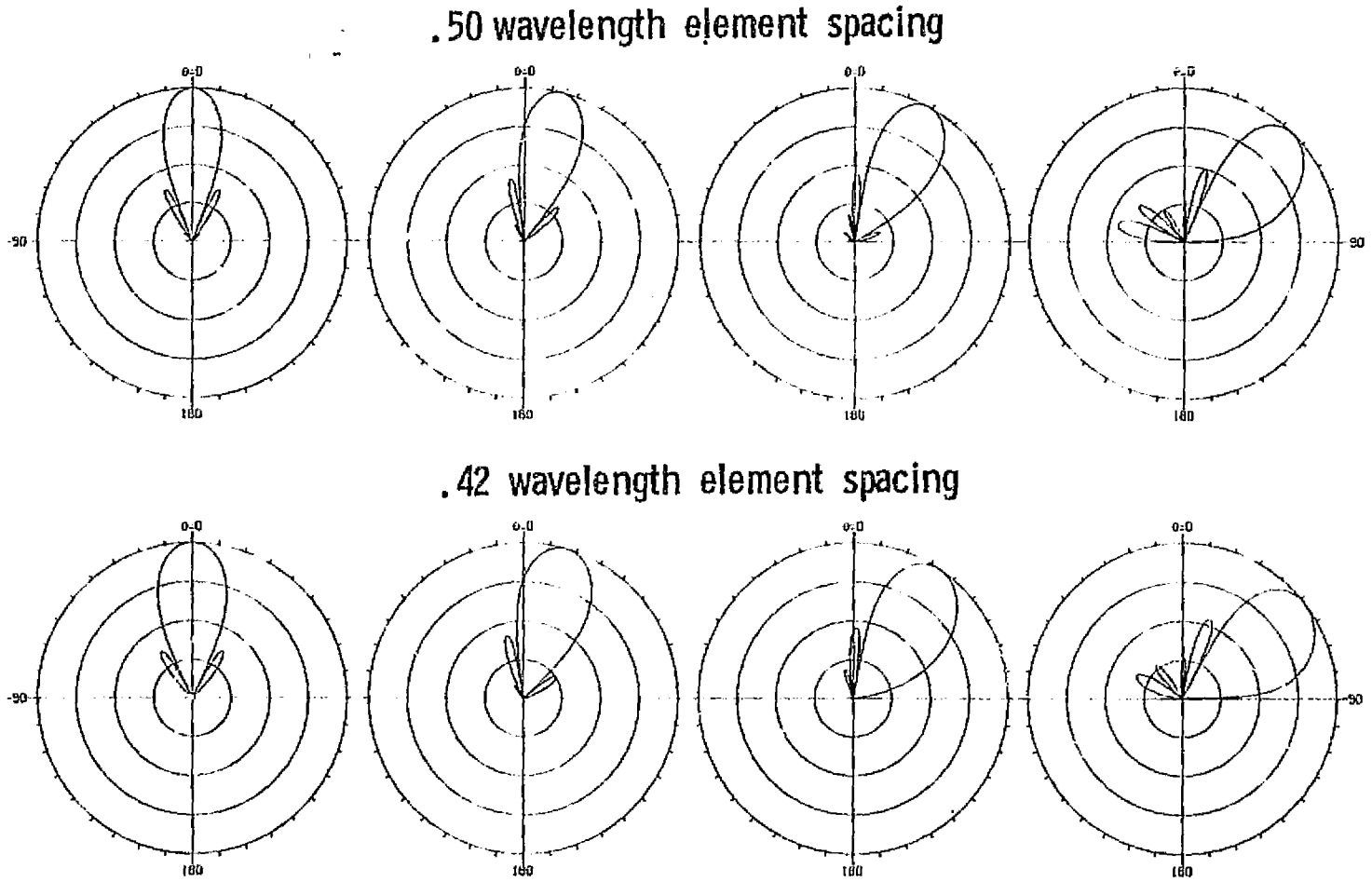

Figure 5-2. Calculated H-plane scanning radiation patterns for a 64 element array.

.50 wavelength element spacing

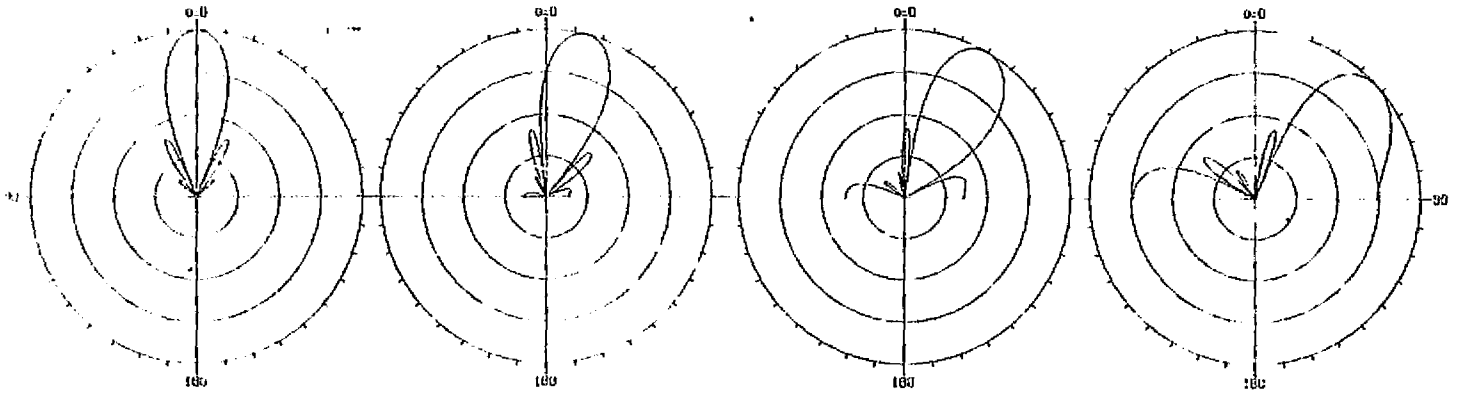

.42 wavelength element spacing

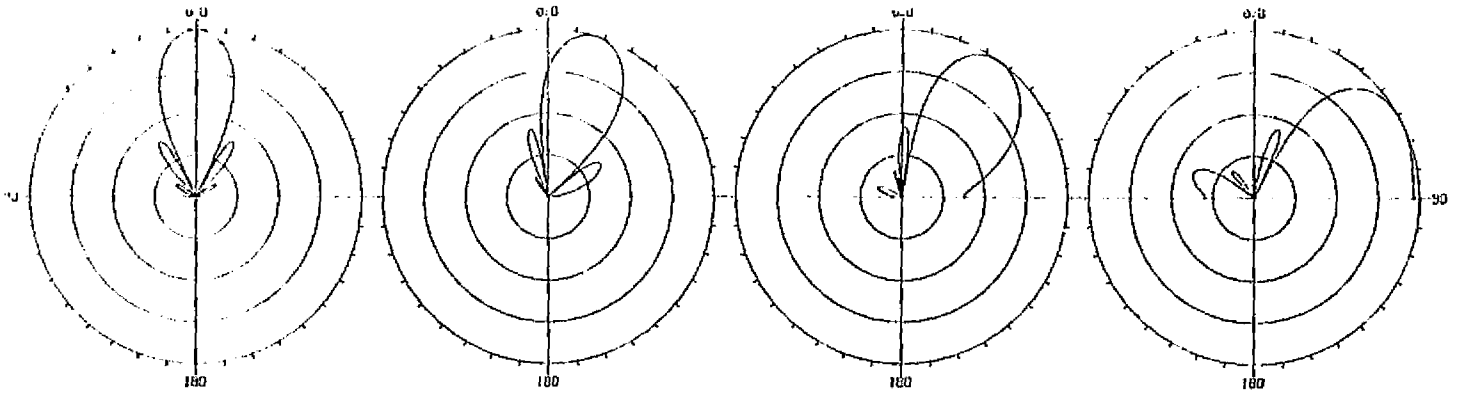

Figure 5-3. Calculated E-plane scanning radiation patterns for a 64 element array.

REFERENCES

1. Munson, R. E.: "Microstrip Antenna Structures and Arrays," U.S. Patent #3,921,177, November 18, 1975.

2. Munson, R. E.: "Microstrip Phased Array Antennas," Twenty-Second Annual USAF Antenna Symposium, October 1972.

3. Munson, R. E., and Murphy, L. R.: "Conformal Microstrip Array for a Parabolic Dish," Twenty-Third Annual USAF Antenna Symposium, October 1973.

4. Howell, John Q.: "Microstrip Antennas," IEEE Transactions on Antennas and Propagation, January 1974.

5. Munson, R. E.: "Conformal Microstrip Antennas and Microstrip Phased Arrays," IEEE Transactions on Antennas and Propagation, Volume AP-22, Number 1, pp. 74-78, January 1974.

6. Sanford, G. G.: "Conformal Microstrip Phased Array for Aircraft Tests with ATS-6," National Electronics Conference, Volume XXIX, October 16, 1974.

7. Weinschel, H. D.: "A Cylindrical Array of Circularly Polarized Microstrip Antennas," IEEE Society on Antennas and Propagation International Symposium, pp. 177-180, June 1975.

8. Campbell, T. G., Appleton, M. W., and Lusby, T. K.: "The Design and Fabrication of Microstrip Omnidirectional Array Antennas for Aerospace Applications," NASA Technical Memorandum, NASA TMX-73979, November 1976.

9. Butler, J. L.: "Digital, Matrix, and Intermediate-Frequency Scanning," edited by Hansen, R. C., Microwave Scanning Antennas, Volume III, Academic Press, 1966.

10. Wheeler, H. A.: IEEE Proceedings, Volume 56, pp. 1940-1951, 1968.

11. Amitay, N., Galendo, V., Wu, C. P.: Theory and Analysis of Phased Array Antennas.

12. Diamond, B. L.: "Small Arrays - Their Analysis and Their Use for the Design of Array Elements," Phased-Array Antenna Symposium, 1970.

13. Kuhlman, E. A.: "Microstrip Antenna Study for Pioneer Saturn/Uranus Atmosphere Entry Probe," NASA CR-137513, May 1974.

14. Watkins, J.: "Circular Resonant Structures in Microstrip," Electronic Letters, Volume 5, pp. 524-525, October 16, 1969.

15. Howell, John Q.: "Microstrip Antennas," IEEE Group on Antennas and Propagation International Symposium, December 1972.

16. Wolff, I., Knoppik, N.: "Rectangular and Circular Microstrip Disk Capacitors and Resonators," IEEE Transactions on Microwave Theory and Techniques, Volume MTT-22, Number 10, October 1974.

17. Balanis, C. A.: "Pattern Distortion due to Edge Diffractions," IEEE Transactions on Antennas and Propagation, July 1970.

18. Oliner, A. A., Malech, R. G.: "Mutual Coupling in Infinite Scanning Arrays," edited by Hansen, R. C., Microwave Scanning Antennas, Volume II, page 215, Academic Press, 1966.

19. Kraus, J. D.: Antennas, McGraw-Hill, pp. 450, 1950.

20. Bailey, M. C., Samaddar, S. N., Swift, C. T.: "Electromagnetic Properties of a Circular Aperture in a Dielectric-Covered or Uncovered Ground Plane," NASA Technical Note, TN D-4752, October 1968.

21. Agrawal, P. K., Bailey, M. C.: "An Analysis Technique for Microstrip Antennas," Submitted to IEEE Transactions on Antennas and Propagations, January 1977.

22. Richmond, J. H.: "Radiation and Scattering by Thin-Wire Structures in the Complex Frequency Domain," NASA Contractor Report CR-2396, May 1974.

23. Collin, R. E., Zucker, F. J.: Antenna Theory, Part 1, McGraw-Hill Book Company, 1969.

24. Hollis, J. S., Lyon, T. J., Clayton, L.: Microwave Antenna Measurements, Scientific-Atlanta, Atlanta, Georgia, 1970.

25. Howell, J. Q.: Unpublished Notes, February 1973.

26. Collin, R. E.: Foundations for Microwave Engineering, McGraw-Hill, 1966.

27. Parks, F. G., Bailey, M. C.: "Mutual Coupling Between Microstrip Disk Antennas," IEEE International AP-S Symposium, October 1976.

28. Bailey, M. C., Bostian, C. W.: "Mutual Coupling in a Finite Planar Array of Circular Apertures," IEEE Transactions, Volume AP-22, pp. 178-184, March 1974.

29. Bailey, M. C.: "Analysis of Finite-Size Phased Arrays of Circular Waveguide Elements," NASA TR R-408, April 1974.

30. Parks, F. G., Bailey, M. C.: "A Low Sidelobe Microstrip Array," To be Presented at the 1977 International IEEE AP-S Symposium, June 1977.

31. Agrawal, P. K.: Private Communications.

32. Howe, H.: Stripline Circuit Design, Artech House, Dedham, Massachusetts, 1974.

33. Coombs, C. F., Jr.: Printed Circuits Handbook, McGraw-Hill, 1967.

34. NASA: Project Management, NASA LHB 7121.1, December 1975.

35. Wolff, E. A.: Antenna Analysis, John Wiley and Sons, 1966.